**ALMA MATER STUDIORUM**
**UNIVERSITA' DI BOLOGNA**

SCHOOL OF ENGINEERING

- Forlì campus -

SECOND CYCLE MASTER'S DEGREE in AEROSPACE ENGINEERING

Classe LM-20

GRADUATION THESIS in Aerospace Equipments and Systems

# Autonomous estimation of the gravity field for asteroids missions

CANDIDATE:
Aurélia Bourgeaux

SUPERVISORS:
Erwin Mooij
Bart Root
Marco Zannoni

Academic year 2019/2020

# Abstract

In the few past decades, there has been an increasing interest in asteroid missions, which can be explained by three main reasons. The first reason being the fact that their composition has remained the same since their formation in the protoplanetary disc, and therefore, they can provide information on the formation of the solar system. The second being the fact that they can be dangerous to Earth, as it has been the case in the distant past and can still be seen in the Yucatan craters. Last but not least, it is possible to exploit asteroid resources before the Earth's resources are exhausted.

Many successful asteroid missions have been carried out, leading to many technical advances, particularly in terms of navigation. However, they all faced many challenges, the latter being the Osiris-Rex probe sample collection. To ensure secure navigation around asteroids, they have shown that precise navigation has been and would be of significant importance. The spacecraft has to experience an extremely disturbed environment while approaching asteroids. Although these asteroids' gravity fields are small, they ca be very irregular and they can perturbed the spacecraft's dynamics. To ensure safe navigation, it is therefore very important to characterise these gravity fields.

Through estimating the asteroids' gravity field, this thesis will approach autonomous navigation. In the navigation software, the spherical harmonics model has been selected to be applied in the simulator. The spherical harmonic coefficients are calculated at each time step, along with the state vector. While this approach is convenient and can lead to sufficiently accurate results, it is important to take into account that this model is limited and can not be used for precise landing near the surface, since when approaching the sphere of Brillouin, the spherical harmonics models tend to diverge. Another gravity model must then be used for the last step of the mission.

A real world model was implemented to propagate the dynamics of the spacecraft in a simulated but"real" environment, taking into account solar induced perturbations and torques as well as the spherical harmonics gravity field of 433 Eros up to degree and order 22. To compare their results, an Extended Kalman filter (EKF) has been developed along with an Unscented Kalman filter (UKF). Although the difference in efficiency was not seen to be significant, the UKF, when calculating large number of parameters, was chosen over the EKF for the simplicity of implementation.

To evaluate its performance, the simulator was tested under different conditions, changing the range, inclination of the orbit, and evaluating the effect of different perturbations on the estimation. The simulator was applied to the Near-Shoemaker mission conditions, where it has been shown that all degree and order coefficients up to degree 8 could be estimated with an error below 10%.

# Preface

I am very pleased to have been able to work on this subject. Passionate about space exploration since I was a child, I was very excited to start this thesis. At the end of this wonderful year, I am still amazed at all the discoveries we can make in this field, and I could not be more motivated to work in this very interesting sector.
This report is submitted as my Master's degree thesis, which is part of the requirements to obtain a Master's degree in Aerospace Engineering from the University of Bologna. The research was carried out at TU Delft during my exchange year under the supervision of Erwin Mooij and Bart Root, my daily supervisors.

First of all, without whom any of this work would have been possible, I would like to thank both my thesis supervisors. Even though we were not able to meet in person because of the pandemic situation, our weekly skype meetings have guided me through the thesis. I really appreciate the fact that you shared your knowledge with me and I really enjoyed the confrontations between engineering and science! You made a lot of valuable suggestions during the meetings and gave me enough freedom to take the directions on my own. I would also like to thank them for their personal support, especially during my lifetime difficulties. You reminded me that health and family are the most important things to take care of.

Secondly, I would like to thank Katia Mathias, who brought me to this "classe verte" when I was at primary school. Since then, my passion about space exploration has only grown, and I really wanted to thank you to have made me discover astronomy and space sciences. This experience was the most amazing for a little girl, who came home knowing what she would do in her life. And here I am, still trying to follow this path.

Thirdly, I would like to thank my family, who have supported me throughout my entire life and this international studies journey. They are the reason why I could have done so much and they are my main motivation. My grandmother, Yasmina, is a strong and inspiring woman who has taught me that when you have faith, nothing is impossible. I could not have moved from South of France to Italy or Italy to the Netherlands without the support of my parents, Soraya and Patrice, who, I must say, are extraordinary. You helped me to pursue my dreams, encouraged me even when you did not understand what I was planning to do and without you, nothing of the best things that happened to me would have been possible. Special mention should be given to my little sister, Audrey, who is my sunshine and who has helped me to believe in myself.

Last but not least, I would like to thank my partner, Lucas, who, throughout the thesis, took care of me and reminded me to eat and sleep. You have helped me stay motivated, you are my main emotional support, and I love you.

# Contents

# Nomenclature

**Abbreviations**

| | |
|---|---|
| $fwhm$ | full width at half maximum |
| AIM | Asteroid Impact Mission |
| AMICA | Asteroid Multiband Imaging CAmera |
| APEX | Asteroid Prospection Explorer |
| AU | Astronomical Units |
| COB | Center-Of-Brightness |
| DDOR | Delta-Differential One Way Range |
| DPR | Dormand-Prince methods |
| DSN | Deep Space Network |
| ECA | Earth-Crossing Asteroid |
| EKF | Extended-Kalman Filter |
| FBS | Fan Beam Sensor |
| FC | Framing Camera |
| FOV | Field-Of-View |
| GNC | Guidance Navigation & Control |
| GRaND | Gamma Ray and Neutron Detector |
| IMP | Inertial Measurement Package |
| IMU | Inertial Measurement Unit |
| IRU | Inertial Reference Unit |
| JPL | Jet Propulsion Laboratory |
| LiDAR | Light Detection And Ranging |
| LOS | Line-Of-Sight |
| LRF | Laser-Range Finder |
| LSC | Least-Squares Collocation |

| | |
|---|---|
| MSI | Multi-Spectral Imager |
| NAVCAM | Navigation Camera |
| NEA | Near-Earth Asteroid |
| NEAR | Near-Earth Asteroid Rendezvous |
| NFT | Natural Feature Tracking |
| NIS | Near Infrared Spectrometer |
| NLR | Near Laser Range-finder |
| OLA | OSIRIS-REx Laser Altimeter |
| ONC | Optical Navigation Camera |
| OSIRIS | Optical, Spectroscopic, and Infrared Remote Imaging System |
| OSIRIS-Rex | Origins Spectral Interpretation Resource Identification Security-Regolith Ex-plorer |
| OTES | OSIRIS-REx Thermal Emission Spectrometer |
| OVIRS | OSIRIS-REx Visible and IR Spectrometer |
| PF | Particle Filter |
| RK | Runge-Kutta methods |
| RW | Reaction Wheels |
| SA | Solar Arrays |
| SPC | Stereophotoclinometry |
| SRIF | Square Root Information Filter |
| SRP | Solar Radiation Pressure |
| STT | Star-Tracker |
| TAGCAM | Touch-and-Go Camera System |
| TOF | Time-Of-Flight |
| TSAS | Two Axis Sun Aspect Sensor |
| UKF | Unscented-Kalman Filter |
| VIR | Visible and Infrared |
| WCG | Weighted Centre of Gravity |
| X REXIS | Regolith X-ray Imaging Spectrometer |

**Greek symbols**

| | |
|---|---|
| $(\alpha, \beta)$ | Control angles, rad |
| $(\alpha, \beta, \lambda)$ | UKF tuning parameters |
| $(\theta, \lambda)$ | Geographical coordinates, rad |
| $(d, \Phi, \lambda)$ | Spherical coordinates, rad |
| $\rho$ | Range, m |
| $\rho$ | Density |
| $\dot{\rho}$ | Range rate, $\mathrm{m.s^{-1}}$ |
| $\sigma$ | Measurement noise |
| $\nu$ | Process noise |
| $\boldsymbol{\omega}$ | Rotational rate vector $\mathrm{rad.s^{-1}}$ |
| $\chi$ | Sigma points |

**Latin symbols**

| | |
|---|---|
| $\mathbf{a}$ | Acceleration, $\mathrm{m.s^{-2}}$ |
| $\mathbf{C_{B/A}}$ | Direction cosine matrix from reference frame A to reference frame B |
| $\mathbf{C}_{ij}, \mathbf{S}_{ij}$ | Spherical harmonics coefficients |
| $f()$ | Process function |
| $\mathbf{F}$ | Force, N |
| $\mathbf{F}_{P/Q}$ | Force exerted on body P by body Q |
| $\mathbf{g}$ | Gravity strength, $\mathrm{m.s^{-2}}$ |
| G | Gravitational constant, $\mathrm{m^2.kg^{-1}.s^{-2}}$ |
| $(\mathbf{i}, \mathbf{j}, \mathbf{k})$ | Unit vectors |
| $\mathrm{m}_p$ | Mass of body p, kg |
| M | Mass, kg |
| $P_{nm}$ | Legendre polynomial of degree n and order m |
| $\mathbf{P}$ | Covariance matrix |
| $\mathbf{P_0}$ | Initial covariance matrix |
| $\mathbf{Q}$ | Process noise covariance matrix |
| $\mathbf{q}_{A/B}$ | attitude vector in the frame B with respect to the frame A |

| | |
|---|---|
| $\mathbf{r}_{i,B}$ | $i_{th}$ vector in the B frame |
| R | Reference radius, m |
| $\mathbf{R}$ | Measurement noise covariance matrix |
| $\mathbf{T}$ | Torque, N.m |
| $\mathbf{T_{B/A}}$ | Transformation matrix from reference frame A to reference frame B |
| $\mathbf{v}$ | Velocity, m.s$^{-1}$ |
| $\mathbf{v_0}$ | Initial velocity vector, m.s$^{-1}$ |
| $\mathbf{V}$ | Potential, J |
| $\dot{x}$ | Velocity, m.s$^{-1}$ |
| $\ddot{x}$ | Acceleration, m.s$^{-2}$ |
| $\mathbf{x}$ | State vector |
| $\mathbf{x_0}$ | Initial position vector, m |
| $\mathbf{X}$ | State and parameters vector |
| $(x_B, y_B, z_B)$ | Coordinates in the spacecraft body frame |
| $(x_I, y_I, z_I)$ | Coordinates in inertial frame |
| $(x_R, y_R, z_R)$ | Coordinates in relative asteroid frame |

**Notations**

| | |
|---|---|
| $a$ | Scalars are represented by italic characters |
| $\mathbf{a}$ | Vectors are written in bold and lowercase font |
| a | Functions and text are written in normal font |
| $\dot{\mathbf{a}}$ | First derivative of a vector |
| $\ddot{\mathbf{a}}$ | Second derivative of a vector |
| $\| \mathbf{a} \|$ | Norm of a vector |
| $\hat{a}$ | Estimate of a |
| $\hat{a}^-$ | *a-priori* value of a |
| $\tilde{a}$ | Noisy value of a |
| $\mathbf{A}$ | Matrices are represented by bold uppercase characters |
| $\mathbf{A}^{-1}$ | Inverse matrix |
| $\mathbf{A}^T$ | Transpose matrix |
| $\mathbf{A}_{ij}$ | Element of a matrix located at the $i_{th}$ row and $j_{th}$ column |
| $\bar{P}$ | The bar represents the normalization |

# 1

# Introduction

Since the discovery in 1801 of the first asteroid named Ceres, interest in these small bodies has only grown. Asteroid missions have been increasingly relevant in past few decades due to the fascinating and complex information that can be obtained from asteroid studies. This thesis will focus on autonomous navigation around asteroids, with a particular interest on the estimation of the gravity field, for such irregular bodies. To do so, a number of aspects need to be discussed, to better understand the theme of this dissertation. First, we will explain why asteroid missions are being conducted, then we will explain briefly what the challenges in this type of environment are, and we will detail and motivate the choice of autonomous navigation.

### Asteroids as a mission target

Asteroids are small, geologically inactive bodies. Although they have experienced considerable collisional evolution since their formation, 4.5 billion years ago, within the disk of gas and dust where the planets were also formed, most of them have not suffered from major geological, thermal or orbital evolution. And this is where the main interest of the study of asteroids lies. Owing to their small size, the original heat of the protosolar nebula was rapidly evacuated by these objects, thereby freezing the initial composition of the protosolar nebula (Binzel et al., 1991). The study of these small bodies therefore gives information on the initial circumstances that occurred at the birth of the Solar System, and the study of their composition can help to understand the origins of the Solar system.

Another interest in asteroids must be understood when staring at the surface of the moon. Covered with craters, we know that in the past, the surface of the moon and the surface of the earth have already experienced many collisions with small bodies. When we talk of collisions with the Earth's surface, it becomes a ritual to invoke the impact of a massive comet or asteroid, 65 million years ago, at the boundary of the Cretaceous and the Tertiary, which was perhaps responsible for the extinction of the dinosaurs. It is therefore important to understand the motion of asteroids in the solar system to predict and maybe avoid future impacts. In particular, the Near-Earth asteroid, which have an orbit similar to the Earth and especially, a subclass called Potentially Hazardous Asteroids, which can be a potential danger for the Earth. Today, in 2020, NASA discovered 2043 PHAs and currently predicts 4700, 1500 of which have a diameter larger than 100 m.[1]

[1] https://cneos.jpl.nasa.gov/stats/totals.html

A third and last interest that can be found in the study of asteroids is economic. Earth's resources are not inexhaustible, and we should expect to be able to access the mineral resources of asteroids in the near future. It is estimated that one cubic kilometre of the M-type, i.e., metallic, asteroid comprises 7 billion tonnes of iron, 1 billion tonnes of nickel and enough cobalt to satisfy global demand for 3,000 years. Asteroids may constitute beneficial space bases for the pre-colonization of the solar system. In reality, thanks to their mineral wealth, they can supply the settlers with building materials as well as their needs for water, oxygen, carbon and nitrogen. In comparison, due to their low mass and thus low gravity, the energy needed to escape the host asteroid is much smaller than the energy necessary to leave Earth.

These three aspects are the main motivations of the asteroids missions. Now we have understood why these missions were conducted, it is interesting to know the technical challenges that asteroid missions have faced in this type of environment.

### Asteroid missions and environment

Our interest in asteroid missions has only grown after the Galileo spacecraft flew by asteroid 951 Gaspra on its way to Jupiter. This success initiated a series of missions devoted to asteroids, each as enriching as the previous mission in terms of technical advancements and scientific research. The first dedicated asteroid mission, named Near-Shoemaker, was devoted to the study of 433 Eros, an Earth-crossing asteroid belonging to the Amor group. This successful mission has produced great developments in terms of navigation, especially due to the unexpected landing phase, which has made this spacecraft the first ever to orbit and land on the surface of an asteroid. The missions that followed have led to a deeper understanding of the processes involved in this type of environment and all the technical advances that have been made possible. However, these missions have faced a number of technical challenges, which have made it clear that the asteroid environment is far more complicated than anticipated.

On its way to the target asteroid, the spacecraft is exposed to general interplanetary forces and disturbances, primarily due to the Sun and the nearest planets. Their effect can be predicted with reasonable precision, as we can acquire information on the distance from these bodies, and we also know the characteristics of these bodies. However, entering the sphere of influence of the asteroid, the environment can be extremely disturbed. It is very difficult to predict the shape of this celestial body, because of the distance and the size of the asteroid. Most of the time, asteroids have a very irregular shape, which leads to an extremely irregular gravity field. Even if its influence is relatively weak, it can severely affect the orbital motion of the spacecraft (Williams et al., 2018). The motion of the spacecraft near the surface can be a great challenge in terms of navigation due to all these irregularities that are difficult to anticipate before the flight. In addition, these disturbances are very interesting to study, because they can provide details on the internal composition of the asteroid. This is why this thesis will focus on estimating the gravity field for asteroid missions. If we can model the gravity field of the asteroid, the on-board knowledge will be enriched and therefore the dynamics of the spacecraft in this environment will be better understood.

Past missions around asteroids have proven that the study of asteroids was feasible, and the success of asteroids-sample return missions such as Osiris-Rex has further our knowledge about navigation around asteroids. We can imagine that in the near future,

Asteroids missions will be more and more frequent. Thus, the navigation around asteroid is and will be of a particular interest.

### Autonomous navigation

To understand why autonomous asteroid navigation is such an important problem to address, we must first answer the basic question: What is a navigation system? The main objective of the navigation system is to answer the not-so-simple question "Where am I?". Included in the Guidance, Navigation and Control System (GNC), which attempts to guide the spacecraft on its trajectory to the target asteroid, we realize the importance of a good navigation system for every mission. Indeed if we are unable to address where the spacecraft is located, it becomes difficult to know where it is heading and how to change its trajectory to meet the location target.

A good navigation system depends on the knowledge that we can give the system to estimate its position via the so-called sensors. The choice of sensors carried by the spacecraft is the first challenge faced in the construction of a navigation system. The number of sensors should be minimised to avoid excessive weight and thus excessive costs. However, the decision must be wise to provide the navigation software with adequate knowledge to determine the position of the spacecraft with sufficient precision. The most commonly used asteroid sensors are Star Trackers, Lidars, and Navcams. These sensors and their combinations are the focus of numerous researchs as they can be a real asset for autonomous navigation, especially with the Navcam which, as we will show later on, can be used for very promising navigation techniques (Owen et al., 2002).

As mentioned above the navigation system is estimating the state of the spacecraft.The navigation system cannot exactly indicate the exact position of the spacecraft. It processes information coming from sensors that may be influenced by noise from the environment or by bias, misalignment or others errors coming directly from the sensors. This measurements are not ideal, and the purpose of the navigation system is to try to eliminate these imperfections to achieve the most precise values, hence the term "estimate". For this process to be carried out, the navigation system should include an estimator, which, based on analytical equations describing the dynamics of the spacecraft and the sensors data, would attempt to determine the real state of the spacecraft. However, a perfect estimation is impossible, and it become important to analyse the final estimation errors and to choose the optimum estimator. The navigation software architecture, with the choice of sensors and filters, will be discussed in Chapter 6 for a more detailed explanation of the navigation software mechanisms.

The last question to be answered is why to develop autonomous asteroid navigation? The first and most simple answer is to reduce operating costs. But it is not the only explanation. Owing to the large distance from the Earth, there is a considerable delay in communication with the spacecraft. It is therefore necessary to make the spacecraft autonomous for this type of mission if we want to improve the safety of the spacecraft during close operations and landings in such disturbed environments.

## 1.2 Research questions

Autonomous asteroid navigation is on its own, a real challenge in many aspects we have already mentioned. The focus of this thesis is, however, on the estimation of the gravity field of the target asteroid, which, due to the irregular shape of these bodies, has a significant effect on the dynamics of the spacecraft while approaching the surface. Accordingly, the main objective of this thesis is to address the following research question:

– ***How to increase the safety of autonomous navigation for asteroid missions?***

With a particular focus on the asteroid gravity field estimation, and therefore to answer the following sub-questions:

***(a) What is the influence of an irregular gravity field on the motion of a spacecraft in the vicinity of asteroids?***

***(b) What is the impact of the gravitational modelling on the navigation accuracy?***

**(c)** ***How can the gravity field be autonomously estimated using only on-board data and measurements?***

## 1.3 Thesis outline

This study is divided into seven chapters starting with the introduction, each of which focuses on a particular theme:

**Chapter 2** : The Mission and studies heritage were addressed in Chapter 2. It will list the previous missions and detail the outcomes and limitations found during those missions. It will also review existing research topics on autonomous asteroid navigation and mission requirements and assumptions will be detailed.

**Chapter 3** : This chapter details the characteristics and properties of the asteroids. Interest in 433 Eros as a target body will be explained.

**Chapter 4** : This chapter will focus on the environment to be simulated. Which bodies are present in the spacecraft environment, which forces and torques are to be considered and how they can be modelled. It will also detail the various gravity field models available to model gravity field of the target asteroid.

**Chapter 5** : This chapter describes every aspect of the Navigation software from hardware to filters. Filters theoretical equations will be derived and each parameter will be explained for a deep understanding of how the estimation process works.

**Chapter 6** : The design of the Simulator will be presented in this chapter. The top-layer software architecture will be explained and every component in the simulator will be detailed. A verification procedure will be conducted for every component of the Simulator.

**Chapter 7** : This chapter will discuss the various scenarios in which the software has been evaluated. The performance of the software will be tested under different conditions to test the limits and find the optimal conditions for the estimation procedure to be carried out. The results of these examples will be explained in depth.

**Chapter 8** : The conclusions and recommendations for future work, based on the results obtained during this thesis will be detailed in this chapter. The results will be discussed, their significance, how they can be interpreted, their validity and their limitations will be assessed.

# 2

# Mission heritage

Over the last few decades, interest in asteroids has evolved. Many technological challenges have been faced by missions, particularly with regard to navigation in such a perturbed environment. Interest in asteroid research will be explained in this chapter, and some of the previous missions will be reviewed, discussing their outcomes and limitations.

## 2.1 Past Asteroid missions

The first close-ups images of asteroids were the work of the Galileo probe, which was approached in 1991 and Ida in 1993 as it travelled to Jupiter. After this successful approach, the interest in asteroids and small-scale missions grew exponentially.

### 2.1.1 Near-Shoemaker

NEAR (Near-Earth Asteroid Rendez-vous) Shoemaker is a space probe launched by NASA on 17 February 1996 to study one of the largest Earth-crossing asteroids, Eros 433, shown in Figure 2.1. It was the first NASA Discovery programme mission, which contributed to several advances in the development of modern navigational strategies to manoeuvre a spacecraft around an irregular body.

The main objective of this 800 kg mass probe, including 56 kg of scientific instrumentation, was to identify the main features of Eros, such as its mass, internal distribution, magnetic field and mineralogical composition (Cheng et Andrew, 2002). To this end, the probe was launched on February 14, 2000, set in orbit around Eros and remained for around a year. The mission ended on 12 February 2001 when, even though it was not planned for such manoeuvres, the spacecraft landed. Against all odds, the spacecraft survived to the landing, and transmitted data and Until 28 February 2001.

Eros' *a-priori* knowledge was not sufficient to allow an accurate design of the orbit, which could have led to unexpected disturbances during the mission, especially in this highly disturbed environment (Owen et al., 2002). The most powerful navigation technique successfully used for the first time during this mission, was optical navigation via Landmark tracking. In addition to the range and radio-metric measurement, these data were used for the asteroid's orbit determination process, gravity and shape modelling, and rotational rate estimation (Williams, 2002).

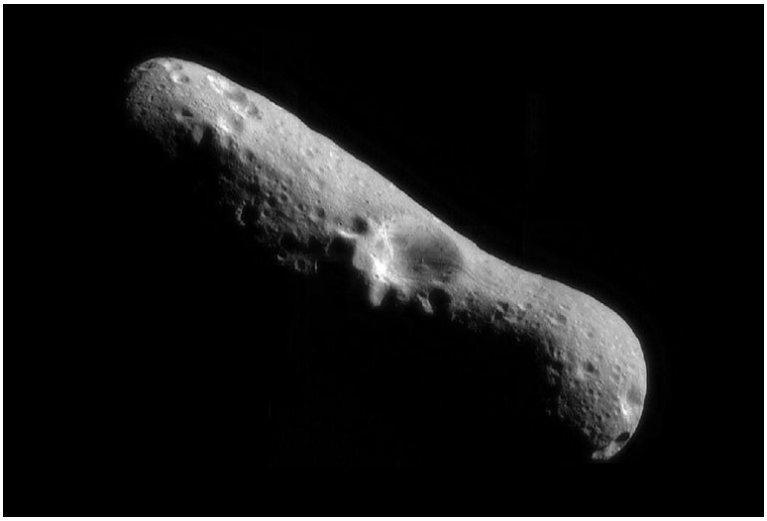

Figure 2.1: Picture of 433 Eros (Image Credit : NASA)

### 2.1.2 Hayabusa

Also known as MUSES-C (Mu Space Engineering Spacecraft), Hayabusa was a Japanese Space Agency (JAXA) space probe. The aim of the project was to research a tiny asteroid named Itokawa and to test new robotic techniques to carry back to Earth a soil sample of the asteroid.

The asteroid probe was launched in 2003, and in 2005 it met with Itokawa, shown in Figure 2.2. Due to the difficulty of navigation in a very low gravity environment, several unsuccessful landing attempts were made before a small sample was obtained. Contact with the probe was very difficult because of the great distance between the planet and the asteroid. Hayabusa carried a star-tracker, IMU and a two-axis Sun-aspect sensor for inertial measurements, as well as optical cameras, lidar, and laser-range finder (LRF) for relative navigation. A three-month approach was scheduled (Hashimoto et al., 2010) after the rendezvous in August 2005. The on-board equipment could not provide sufficient information to estimate the key physical parameters during this process, because of the poor gravity of Itokawa and because the approach was made on a straight line. Therefore, 3 km away from the centre of mass of the asteroid, an orbit phase was scheduled, requiring high navigation protection procedures to prevent collisions with the surface of the asteroid. Since Hayabusa moved towards the asteroid in a straight line, an accurate asteroid gravitational field estimation was not needed for navigation in the first mission phase (Yoshikawa et al., 2006). Instead an assessment of the solar radiation pressure and gravity in the trajectory was used to estimate the mass.

### 2.1.3 Rosetta

To analyse and collect data on the core composition of comet 67p/Chouriusumov-Guerassimenko, Rosetta was launched by the European Space Agency on 2 March 2004. This research mission's main purpose was to investigate the origin and relationship of comets with the

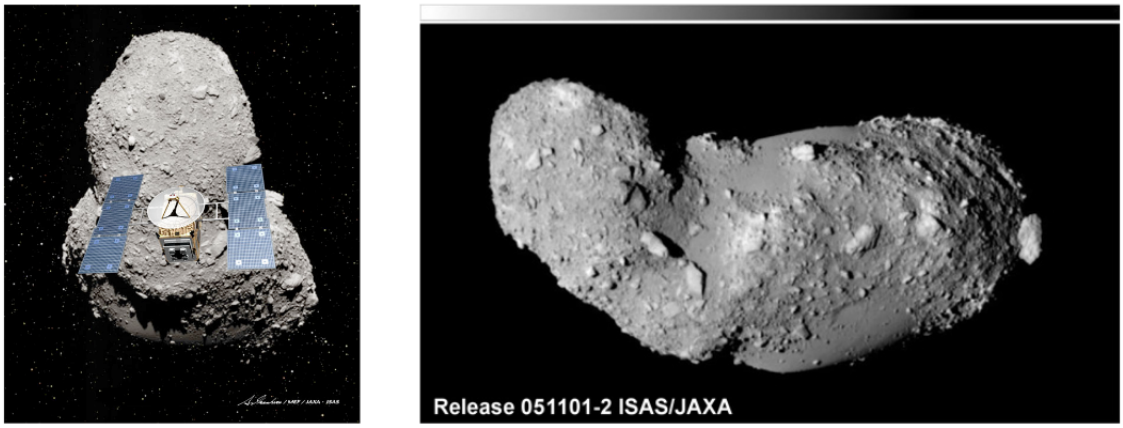


Figure 2.2: Hayabusa spacecraft and the asteroid Itokawa (Yoshikawa et al., 2006).

origin of the Solar system. Rosetta is the sixth spacecraft that observe a comet from a short distance, but the first to orbit a comet and carry a lander to the surface. On 12 November 2014, Philae landed on the surface. In many aspects, this project was a real technological challenge. Until the spacecraft met the target, the main parameters, the gravity and the physical parameters such as mass remain undetermined. As the trajectory was very difficult to forecast, because of this lack of knowledge, a versatile strategy to cover for the uncertainties had to be adopted. In addition, the probe had to be autonomous during critical phases, which is a real challenge for safety and navigational design, due to the substantial Earth-comet distance (Munoz et al., 2012). The trajectory of the spacecraft was estimated by radiometric monitoring from ground stations on Earth, such as the Doppler range or the DDOR (Delta-Differential One Way Range), which provided reliable data on the Solar System barycenter. However, this knowledge was not sufficient to describe the approach trajectory relative to the comet, primarily due to significant uncertainties about the comet and its environment (Godard et al., 2015).

Accurate relative navigation could only be achieved by using optical navigation methods with on-board optical cameras taking pictures of the comet's surface, defining directions from Rosetta to the comet's centre and enhancing relative navigation performance (Castellini et al., 2014).

### 2.1.4 Dawn

Dawn was a NASA probe launched in 2007, the mission of which was to study Vesta and Ceres, the two major bodies of the Main Belt. The observations began in 2011, first orbiting Vesta and then Ceres, and ended in 2018. It was the ninth mission of NASA's Exploration Program. The DAWN mission was the first to use only optical navigation for relative navigation with radiometric and Doppler data for absolute navigation. No altimeters or star-trackers were used, only two navigation cameras (FCs) were carried for redundancy. Optical navigation cameras have been used for scientific purposes as well as for the orbit determination and gravity modelling (Konopliv et al., 2014).

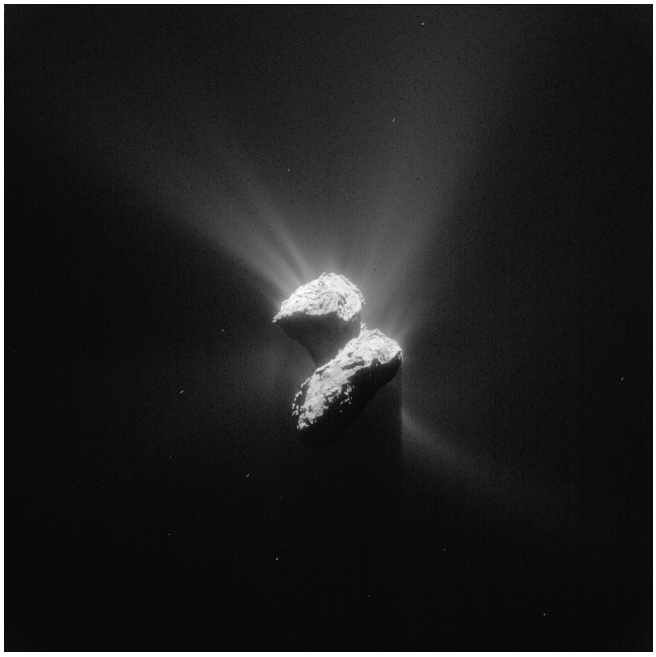

Figure 2.3: Picture of the comet Tchouri taken by the NavCAMs of Rosetta, 5 June 2015. (Image Credit : ESA)

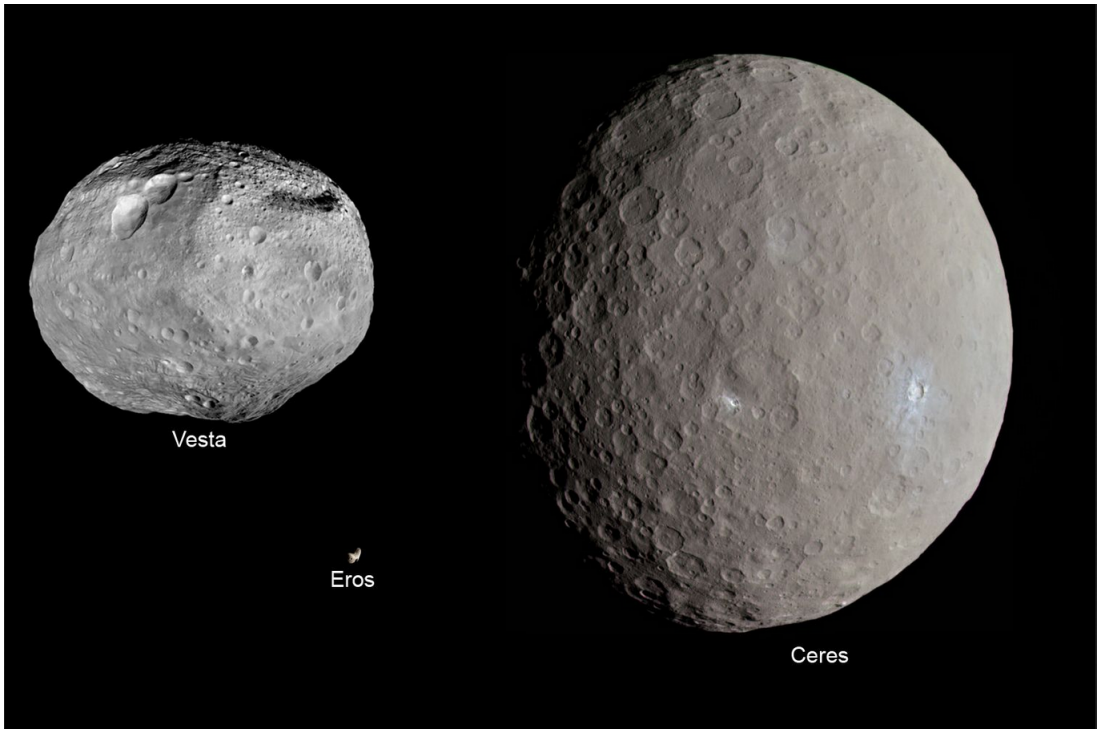


Figure 2.4: Comparison of Ceres, Vesta and Eros (Image Credit : NASA)

### 2.1.5 Osiris-Rex

OSIRIS-REx (Origins-Spectral Interpretation-Resource Identification-Security-Regolith Explorer) is a NASA mission launched on September 8, 2016 to research and carry back a sample of the Earth-crossing asteroid named Bennu.

The main objective of this mission is to collect data that will allow us to better understand the Solar System's formation process. The primary elements of the Solar System that the asteroid has retained can be isolated by retrieving a sample from the surface. It is the first mission by NASA to send an asteroid sample back to Earth. In terms of navigation and flight dynamics, this mission faced many difficulties, such as very accurate manoeuvring and orbiting around a very small asteroid, at low altitude, to precisely map the surface. The sample has been obtained by a robotic arm after landing on the surface, requiring surface navigation. The return to earth is expected to take place in 2023.

Launch and interplanetary phase navigation was made by Radio metric tracking using Nasa Deep Space Network and DDOR to estimate the absolute state of the spacecraft (McMahon et al., 2018). The approach of Bennu was made by Optical Navigation Tracking and lidar, to estimate the relative state of the spacecraft with respect to the asteroid. During this mission, a new navigation technique called Natural Feature Tracking (NFT) was introduced and tested. To evaluate the trajectory, the NFT uses image analysis. It compares features previously determined during earlier stages of the missions with on-board data of known features during landmark tracking to assess the spacecraft's attitude and uses extended Kalma, filter to update the position and velocity based on the previous spacecraft state.

## 2.2 Autonomous navigation research

Autonomous navigation is a very broad topic, as it covers all stages of the navigation process, from the sensors to the estimation technique. Numerous research has been carried out in this area, and it is still a very active research topic to study for future missions.

### 2.2.1 Current research objectives and results

The asteroid environment, while dominated by the gravitational field effect of this body, is generally a highly disturbed environment. As we have seen before, asteroids are usually small and may have very irregular shapes. These properties of asteroids contribute to a very complex dynamic system, which makes it very difficult to orbit around them. Orbits can be quite tough to anticipate and thus it is complicated to ensure safe navigation and prevent collisions with the surface. The interest in landing asteroids makes it even more difficult to ensure the safety of spacecraft. Moreover, since the shape and rotation of the asteroid are not known beforehand, the spacecraft must provide a complex and robust GNC system to approach, meet and land safely on the asteroid. That is why autonomous navigation is being studied for this kind of mission, to improve on-board knowledge and therefore improve navigation safety.

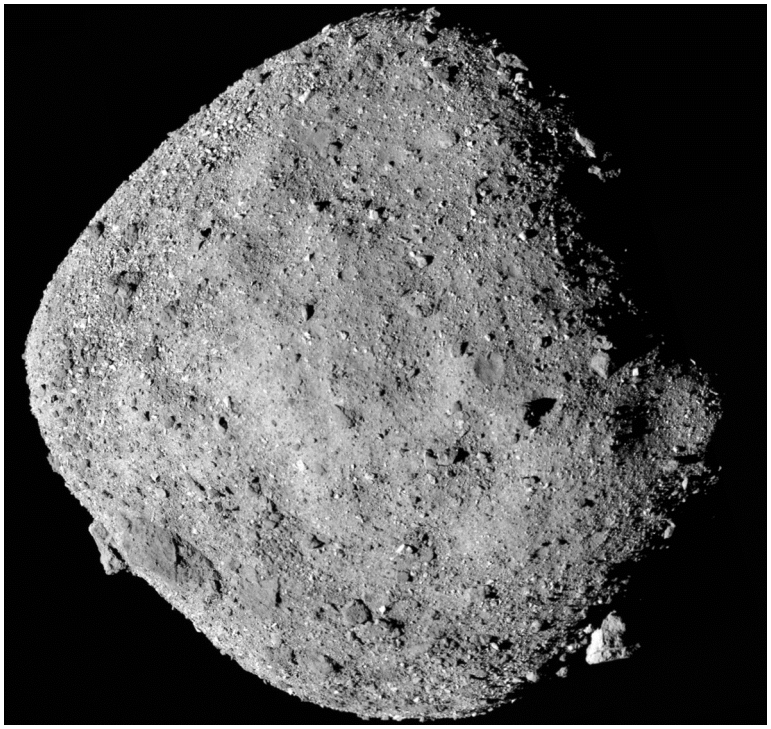

Figure 2.5: Image of Bennu taken by polycams of Osiris-Rex mission before spacecraft arrival (Image Credit:NASA)

We should think of the work of Mooij et al. (2009), which studied the gravitational modelling of a diamond-shaped asteroid, Steins, for autonomous navigational purposes, and which is the main basis of this thesis. They have shown that the spherical harmonics model diverges near to the surface and therefore it is wiser to use a polyhedral shape approximation or a triaxial ellipsoid model. However, the last two models are seen to be 20 times slower than the spherical harmonics model.

Kubota et al. (2010) discuss an autonomous GNC system for the MUSES-C spacecraft and the Rendez-vous and Landing Conditions. Gil-Fernandez et al. (2019) demonstrate HERA's GNC technology, developed to maintain a balance between navigation safety, flight operations, payload and spacecraft characteristics and time constraints. The GNC system depends on a vision-based navigation system with a landmark tracking as well as an attitude-based approach. Autonomous navigation based on optical tracking is a very promising technique, particularly for asteroid landings. The new autonomous navigation algorithm for optical navigation is described in the work of Shuang et al. (2013), which achieved a position error and a velocity error of less than 1 m and 0.1 m/s respectively.

### 2.2.2 Msc Thesis heritage

The studies already done by fellow students at TU Delft have been reviewed to support our research. We can think of the work of Razgus (2016), who used a dual-quaternion approach to investigate the relative navigation in the vicinity of asteroids. He compared two separate approaches, the Cartesian coordinates for position and the attitude quaternions,

and the double quaternions approach. The two methods, he concluded, were quite similar. Some of the models that he developed will be reused in the future study, for example for the asteroid and its environment. We may also think of the study of Moreno Villa (2018), which examined the motion of satellites around small bodies. A GNC simulator was designed to test the behaviour of the orbit determination methods used in ground control centres. The results showed a difference in magnitude between the long and cross-track directions and the radial direction, due to a lack of information on the line of sight of the optical measurements, which could not be removed. Both of these master's thesis will be used as a basis for the development of our simulator, as they already developed a navigation software and simulator, and they both worked in asteroids environments.

## 2.3 Outcomes, limits and initiatives

Outcomes and drawbacks of navigation systems observed during previous missions will be evaluated in this section. The conclusions, assumptions and mission requirements that result from this analysis will be detailed.

### 2.3.1 Outcomes and Limits

Future asteroid missions would require a high degree of guidance, navigation and control autonomy to minimise costs and to perform more complex missions. During previous missions, different navigation strategies have been used. Near-Shoemaker faced a lot of navigation challenges due to the unusual shape of the asteroid. In addition to optical landmark tracking, it uses Radiometric Doppler and Range tracking to navigate around Eros. The SRIF filter was used to approximate the physical parameters of Eros, but the calculation of mass was quite difficult. Owing to the very low gravity of Eros, a high accuracy of navigation and low reaction time became very necessary to prevent escape or crash on the surface. As a result, the highly disturbed orbit at the time of the arrival at Eros was very hard to anticipate and the data was very slow to converge. Navigation camera images were analysed on Earth to identify landmarks, which makes this process very expensive in terms of workload and time loss.

Hayabusa encountered similar issues. The landmark tracking, which was processed on Earth, was a very heavy task for the navigation team. Navigation was intended to be entirely autonomous on the approach of Itokawa, but due to the malfunction of the reaction wheel and the complex shape of Itokawa, it was not possible to locate the centre of mass of the asteroid. Hybrid ground-based optical navigation was therefore used instead of autonomous navigation. Gravity simulation of Itokawa were carried out using periods of no thrust but the accuracy was poor due to the direct trajectory of the spacecraft.

Rosetta showed some weaknesses in the absolute navigation system. The star-trackers used to determine the absolute location of the spacecraft became disturbed by the debris of the comet and the increasing activity of the comet. Star trackers help monitor the attitude of the spacecraft by guiding the high-gain antenna to Earth for communication. Thus, as this condition arose, the high-gain antenna began to drift away from Earth, and communications with the spacecraft were almost lost. It has been demonstrated that star-trackers cannot function independently in such a noisy environment.

The initial Osiris-Rex mission was to use only Lidar for autonomous navigation, but a new system, a natural tracking feature, was added due to reliability issues. The NFT framework depends on the integration of images captured by optical navigation systems with an on-board catalogue. Since this device was brought late in the mission process, it was not completely used during this mission, but this system has an immense potential for future missions.

These missions have contributed to the development of many techniques essential for precise navigation. Kim et al. (2007) developed a Multiplicative Expanded Kalman Filter to approximate the relative state of the spacecraft with high precision, based on optical-navigation measurements. The outcome of this research is an estimate of the state of the asteroid as well as the state of the spacecraft. Many on-board optical estimation algorithms have been developed for small-body exploration, based on the results of previous missions and the shortcomings of current missions, such as the AIM mission. The importance of autonomy has been emphasised, and the incorporation of camera measurements into the on-board spacecraft estimator has been a significant topic of past research. We should think of the work of Hashimoto et al. (2010), which uses the estimator for the asteroid return sample mission. Adding a laser range to optical navigation as with the Osiris-Rex mission, significantly improved navigation accuracy. The NFT can be used to lower the laser range error, which can be very high based on the shape of the asteroid.

### 2.3.2 Mission requirements

Missions requirements can be discussed according to the mission heritage information.

**REQ-MIS-01** 433 Eros will be chosen as a reference asteroid for the thesis.

**REQ-MIS-02** The asteroid will be visited by the spacecraft and the results will be compared to existing models built during the NEAR mission.

**REQ-MIS-03** The spacecraft will be designed on the basis of the Near-Shoemaker spacecraft, weighing 800 kg, with a cubic shaped body of 1.7 m length and two solar panels with dimensions $1.2 \times 1.8$ m.

**REQ-MIS-04** The mission should be based on the Near mission. First, a flyby at 1200 km will be conducted to estimate the SRP and an *a-priori* of the $\mu$ parameter value, then a 200 km orbit to estimate $\mu$ more accurately, and to attempt the estimation of the $J_2$ and first-order harmonics coefficients. At 50 km from the surface, an attempt to estimated the spherical harmonics coefficients will be made and confirmed with a 35 km altitude orbit, who should terminate the estimation.

**REQ-MIS-05** The trajectory should be designed to ensure maximum time with sufficient illumination conditions for optical navigation, i.e., the phase angle (the angle between the direction of the Sun and the spacecraft's relative position vector) must remain within the range of 20° to 70°.

**REQ-MIS-06** The mission shall be planned to ensure optimum surface coverage, i.e., the inclination should be as near as possible to 90. In addition, repeat orbits must be avoided.

**REQ-MIS-07** The spacecraft shall navigate autonomously without the intervention of the ground station.

**REQ-MIS-08** The spacecraft is equipped with a star tracker for absolute attitude measurement.

**REQ-MIS-09** The spacecraft is equipped with Lidar and optical navigation cameras for relative state measurement and the creation of a digital elevation model to characterise the surface of the asteroid.

**REQ-MIS-10** The spacecraft carries an accelerometer to estimate the solar radiation pressure in the early characterisation phase.

**REQ-MIS-11** The navigation system should be able to estimate the gravity field of the asteroid as well as its rotational rate and the inertial state of the spacecraft.

**REQ-MIS-12** The trajectory should remain a collision-free course at all times, which means that the distance between the asteroid and the spacecraft cannot be less than the error on the state of the spacecraft.

**REQ-SYS-01** The spacecraft should be able to navigate around an asteroid, regardless of its physical characteristics.

**REQ-SYS-02** For optimum landmark navigation the phase angle should be constricted between 20°and 70°, that the surface seen by the camera is illuminated.

**REQ-SYS-03** The mass of the asteroid and the SRP force shall be determined with a 3-sigma accuracy of at least 10%.

**REQ-SYS-04** The state of the spacecraft should be estimated with a precision of 10 m for the position and 1 mm/s for the velocity, with 3-sigma confidence.

**REQ-SYS-05** The gravity field coefficients should be determined at least up to the order/degree 8 with a 3-sigma accuracy of at least 10%.

**REQ-MAT-01** The software should be able to run on a computer with the following characteristics: i5-6200U CPU, dual-core 2.30-2.40 GHZ, 8Go RAM. The simulation time should not exceed one day in total for each scenario.

### 2.3.3 Assumptions

The assumptions of the missions are the following :

- At the beginning, only the distance between the Earth and the asteroid is known, as well as a gross estimate of the mass and shape of the asteroid.
- The first part of the spacecraft's trajectory, from the Earth to the asteroid's encounter, is not considered. This part of the journey is assumed to be well designed in advance, without any disruptive body encounter.
- The physical parameters of the asteroid remain unknown, until the spacecraft is close enough to determine those parameters by itself.

- The only perturbations present in the environment will be the SRP force and torques, the gravitational effect of the asteroid and the third-body perturbation from the Sun.
- In the Simulator, the gravity field of the asteroid will be modelled with a spherical harmonics model up to degree and order 22, with coefficients obtained from the NEAR mission.
- The SRP force is assumed to be estimated in the early characterisation phase with an accelerometer, the estimation will not be conducted in this thesis.
- After the early characterisation phase, the surface of the asteroid will be scanned and the landmarks will be identified. Their coordinates will be stored on-board for the next phases.
- The motion of the asteroid around the Sun will not be taken into account.
- We can assume a constant rotational rate for the asteroid, to be determined by the navigation process. No nutation or precession effects will be taken into account.
- The spacecraft is able to navigate around asteroids only, comets being the source of extra noise due to their geological activity.
- We will use ideal sensors, which means that the sensors have no scaling errors or misalignment
- No image processing will be done during the thesis. The navigation camera will output noisy pixel coordinates of landmarks.
- Only the estimation of the required states and parameters will be done. During this time, we assume that the position and velocity of the spacecraft will be autonomously controlled.

# 3

# Asteroids

Asteroids, also called minor planets, are small bodies made up of rocks, metals and gazes, with lengths ranging from a few metres to hundreds of kilometres. While the origin of asteroids is still one of the most complex problems in cosmology, the prevailing hypothesis is that they are made up of residual fragments of the initial protoplanetary disc. They are therefore considered to provide valuable information about the genesis of the Solar System. This chapter will detail asteroid properties and their classification.

## 3.1 Physical and Dynamical Properties

The primary recognised feature of asteroids is their diversity. They vary in scale, form, colour, chemical and mineralogical composition from each other, which makes them so distinctive. This particularity makes asteroid missions much more complicated, since for navigation and trajectory design, the dynamic properties of the target object are very important.

## 3.2 Mass, Shape and Size

The Rosetta probe showed in detail the Tchouri Comet's irregular structure and very steep surface. The Solar System is full of different shapes of these small celestial objects. However, some objects are almost spherical, such as planets, the Sun, or the Moon. This is mainly due to the fact that the electrostatic force of these bodies exceeds the gravitational force. Thus, their gravity field dominates the inner strength of the planets, which contributes to an equilibrium shape.

It is the electrostatic force that dominates a less massive object. However, its range is restricted to a few interatomic distances, unlike gravitational force. Therefore, it has no effect on the body's overall form. This is why small celestial objects may have an irregular shape and thus an irregular gravity field, such as Tchouri, whose size is a few kilometres. It has been shown that an asteroid's shape can also be influenced by spin rates (Holsapple, 2001) and distinguished from hydrostatic equilibrium. It is possible to observe different shapes of asteroids, as shown in Figure 3.1.

Mass estimation of asteroids is very important for enhancing the understanding of inner planetary motion. Typically, estimating the mass of an asteroid from ground-based

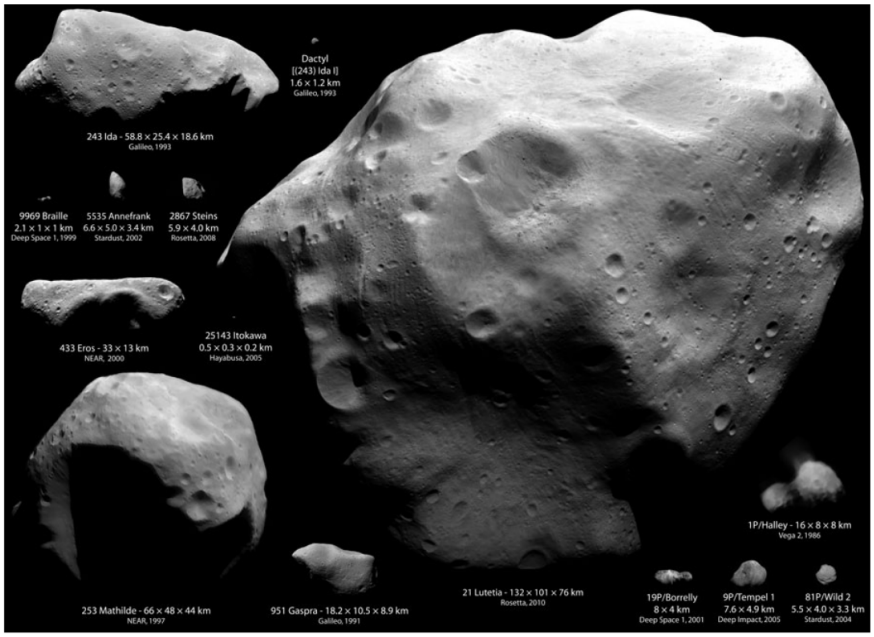


Figure 3.1: Various shapes of asteroids (Image credit: NASA)

measurements is very difficult and errors can be greater than 50%. Two key methods are used to estimate an asteroid mass from ground-based observation, a dynamic method and an astrophysical estimation method. The dynamical approach is based on observations of the impact of asteroid-related gravitational disturbances on other objects in the surrounding region of this asteroid. This method provides direct mass measurements and, as shown by Ivantsov and Anatoliy (2008), can lead to relative errors of less than 50%.

Another way to estimate the mass of the asteroid is to study the effect of the asteroid on a spacecraft during a mission. Optical observations, Doppler and range measurements of the spacecraft orbiting can be used to calculate the mass of the asteroid as shown by Yeomans et al. (2000) during the Near Shoemaker mission. The mass can also be determined by observing the effect of the asteroid on the predicted trajectory. As shown by Yeomans et al. (1998), during the flyby of 253 Mathilde by the Near-Shoemaker spacecraft, the impact of the gravitational disturbance on the spacecraft was sufficient to estimate the mass using the tracking data. Using the optical data collected from navigation cameras, an estimate of the volume can be made when the spacecraft is close enough to cover the whole body with the cameras. The volume can also be determined by astronomical infrared measurements. It makes it possible to estimate the so-called bulk density of the asteroid. Asteroid bulk density measurements may provide insight into the internal structure or porosity of the object.

## 3.3 Rotational rates

Study of the rotation of asteroids is essential in understanding the structure and formation of asteroids. Celestial bodies rotate due to the accumulated angular momentum during their creation and the additional angular momentum due to collisions with other

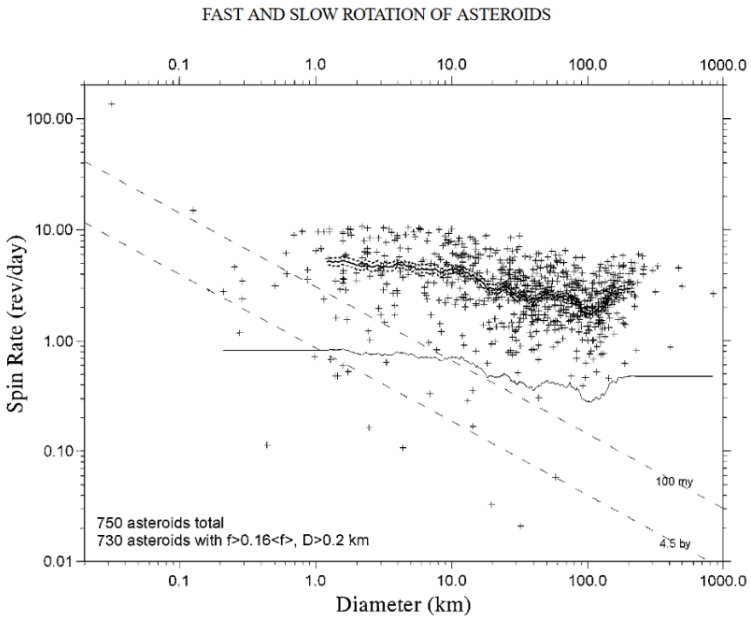


Figure 3.2: Asteroids spin rate vs diameter plot (Hughes, 1983).

bodies. Rotational rates also have a major impact on the orbiting spacecraft, which is why knowledge of this rate is critical for navigation and trajectory design. In addition to light-curve results, rotation studies provide details on the internal structure of the asteroid. Although several studies have been performed in this area, the understanding of the relationship between asteroid properties and rotational speeds is still not well understood.

Many asteroids rotate uniformly and have a rotation period ranging from very fast (T = 1.3 min) to very slow (T = 2.400 hours). Hughes (1983) has shown that there is a relationship between the rotational rate and the size of the asteroid, as shown in Figure 3.2. The bold solid curve is the geometric mean spin rate vs. diameter, the thin solid curve is the limit used to exclude slow rotators. Constant time-scale damping lines of non-main-axis rotational motion (thin dotted lines) are also plotted. From this figure, we can see that increasing the diameter causes the mean rotational rate to decrease.

As written by Pravec and Harris (2000), the population of asteroids can be distinguished. It has been shown that there is a limit in the spin rate for asteroids with a diameter greater than 40 km, which I s approximately 2.4 hours. This limitation can be explained by the fact that most of these asteroids are made up of rubles that will break apart at higher spin speeds. There are two distinct populations of asteroids smaller than 40 km in diameter, slow and quick rotators. For the smallest asteroids with a diameter of 0.15 km the spin rate can be very high, up to 1.3 min and can be understood by their monolithic composition. Among Near Earth asteroids, a significant fraction of the fast rotators are binary systems. They are probably the product of the disturbance of the tidal waves during their passage near planets.

The composition of asteroids may also have an influence on their rotation period. Indeed as Harris and Burns (1979) indicates, Type-C asteroids have a rotation time of 20% slower than Type-S asteroids. This indicates that C-type asteroids are less compact

or less dense than other types. While most asteroids have one main axis of rotation, a small fraction of them have an additional axis of rotation that can be correlated with precession and nutation effects, and this can lead to unexplained rotations such as the Toutatis asteroid. Its rotation is the product of two distinct forms of motion around two axes with a period of 5.4 and 7.3 Earth days respectively. Its shape and its specific rotation could be the result of several collisions.

## 3.4 Classification

Asteroids can be categorised using their distribution within the Solar System, their chemical composition and configuration.

### 3.4.1 Spatial location

Main groups of asteroids based on their locations within the Solar system are:

**The Main Belt of Asteroids:** Between the orbits of Mars and Jupiter, the largest group of asteroids in our Solar System is located at a distance of two to four astronomical units (au). Around 720,000 objects from this belt have been listed so far (2019). Due to orbital resonance phenomenon, the impact of the gravitational field of Jupiter has stopped all these bodies from forming a planet and is the source of the Kirkwood gaps, almost empty areas found in the middle and on the edges of the belt.

**Jupiter Trojans:** Trojan asteroids share their main body's orbit around the Sun, and are centred around the Sun-Jupiter system's $L-4$ and $L-5$ Lagrange points. In the region of Jupiter, the largest Trojan asteroids are found, hence the name of the Jupiter Trojans.

**Near Earth asteroids (NEAs):** Asteroids with an orbit similar to the orbit of the Earth with a radius of perihelion equal to or less than 1.3 au. Earth-crossing asteroids (ECAs) are asteroids with a radius of aphelion equal to or less than 1,381 au (Mars-Sun distance) and whose orbits cross the orbit of the Earth. Potentially Dangerous Asteroids (PHAs) are a specific and significant class of NEAs for which the trajectory passes very close to Earth and could cause catastrophic damage to the Earth.

**Centaures:** They are known to be minor planets that gravitate between the Gas Giants' orbits. Owing to the intense impacts of the outer planets, they usually have unstable orbits.

**Kuiper Belt and trans-Neptunian objects:** There are asteroids whose orbit is beyond the orbit of Neptune. The Kuiper belt is a ring similar to the Main Belt located in the trans-Neptunian zone, but much broader, wider and much more massive. It is mainly made up of bodies of small sizes and three dwarf planets, Pluto, Makémaké, and Hauméa.

### 3.4.2 Chemical composition

The composition of the asteroids is assessed, as written by Shestpalov and Golubeva (2020), according to their optical spectra measuring the reflected light. This classification scheme is called asteroid spectral classification. Even if the chemical composition of the asteroids is very complex, depending on their mineral composition, it allows the asteroids to be divided into different groups. The following are the primary types:

- C-Type asteroid: The most common known asteroids (around 75%) are carbonaceous asteroids. They are distinguished by a very dark colour and their structure, without light and volatile elements such as ice, is similar to the primitive Solar System.
- S-Type asteroids: They are mostly composed of silicates, which are moderately white and composed primarily of iron, magnesium and nickel. They are the second most common type, with 17% of the known asteroids.
- M-Type asteroids: They have a composition that is partly known and corresponds to the rest of the asteroids. They are distinguished by a bright surface, and some of them are often made of an iron-nickel alloy.

### 3.4.3 Configuration

Asteroid configuration helps us to classify them into three categories: single asteroids, binary asteroids contact, and binary asteroid systems. The configuration affects the asteroid's shape, which can be from very irregular to nearly spherical. Single asteroids are bodies with only one element and their irregular shapes define them. They constitute 20% of the Solar System's asteroids. Binary systems are the composition of a primary asteroid and a secondary asteroid, orbiting around their common barycenter .They constitute roughly 17% of the NEAs. Finally, contact binaries are binary systems whose components have gravitated towards each other before direct physical contact was formed. It is possible to perceive them as a single body consisting of two lobes. Since most asteroids are irregularly shaped, predicting their gravity field is very difficult. They can be pitted or crated on the surface and that is why it is necessary to know their characteristics in detail to ensure secure missions

## 3.5 Interest in 433 Eros

433 Eros was discovered on August, 13, 1898 by August Charlois, in Nice, France, and by Gustave Witt, in Berlin, Germany. It is a Near-Earth asteroid, meaning that its orbit is approaching or crosses the orbit of the Earth. It is very useful to understand this class of asteroids and in particular, potentially hazardous objects (PHOs) to anticipate and prevent possible Earth impacts. From a chemical point of view, Eros primarily consists of silicates and thus belongs to asteroids of type S. It belongs to the group of Amors, also known as Earth-grazing asteroids, a group of small bodies which do not cross the Earth's orbit. Eros is following an elliptical trajectory, with a 1.13 AU perihelion and a 1.78 AU aphelion. The trajectory is inclined of 10.8°with respect to the ecliptic, with an average

Table 3.1: Characteristics of 433 Eros

| | |
|---|---|
| Size | 33 km x 13 km x 13 km |
| Approximate mass: | $7.2 \times 10^{15}$ kg |
| Rotation Period: | 5.270 hours |
| Orbital Period: | 1.76 years |
| Spectral Class: | S |
| Semi major Axis: | 1.458 AU |
| Perihelion Distance: | 1.13 AU |
| Aphelion Distance: | 1.78 AU |
| Orbital Eccentricity: | 0.223 |
| Orbital Inclination: | 10.8 deg |
| Geometric Albedo: | 0.16 |

distance from the Sun of 1.46 AU[1]. The general characteristics of Eros are resumed in the Table 3.1. All the data collected during the NEAR mission, such as shape, gravity models, and landmark data are available on a dedicated website.[2].

The (NEAR)–Shoemaker mission was a breakthrough in that it reflected the realistic navigation of a spacecraft in the most seriously disturbed orbital environment a spacecraft has ever encountered. In addition, all future asteroid orbital missions will encounter conditions close to those experienced by NEAR at Eros in some way. It is therefore very interesting to take this asteroid as a reference for this study, particularly since its highly irregular shape contributes to a highly irregular gravitational field, and therefore the modelling of this gravitational field could be a very tough challenge. In addition, numerous models are currently available for the Eros shape and gravity field, which can be used as a reference for the results obtained during this thesis.

[1]https://nssdc.gsfc.nasa.gov/planetary/text/eros.txt Accessed on: 27-04-2020
[2]https://sbn.psi.edu/pds/resource/nearbrowse.html Accessed on: 27-04-2020

# 4

# Orbital Mechanics and Flight environment

The asteroid environment and spacecraft dynamics will be presented in this section. It will reveal the technical characteristics of the spacecraft to be used in the simulator, as well as the properties of the asteroid and the disturbing forces that can encounter the spacecraft around this kind of body. The Near-Shoemaker mission will be used as a reference for this thesis, so we will be studying the asteroid 433 Eros.

## 4.1 Spatial representation

Details on the reference frames and coordinate systems used to describe positions and attitudes in the real environment will be provided in this section.

### 4.1.1 Reference frames and Cartesian coordinates

The motion of the spacecraft and the asteroid in the environment is represented by three reference frames, from which the Cartesian coordinates can be obtained, as shown in Figure 4.1:

**"Inertial" reference frame:** It is a non-rotating frame and is assumed to be non-accelerating with respect to the stars' reference frame, originating at the asteroid's centre of gravity. The X-axis is set by use of the vernal equinox. This reference frame is used both to explain Eros' rotation and to describe the spacecraft's inertial state. In this reference frame, the coordinates are denoted by $(x_I, y_I, z_I)$.

**Asteroid reference frame:** This reference frame, since it rotates with the asteroid, is non-inertial. It is again fixed to the asteroid's centre of gravity, but with the X-axis fixed to the asteroid's prime meridian, selected by Near scientists, and equator, and the Z-axis parallel to the axis of rotation. The prime meridian defines the zero-degree longitude line, while the equator defines the zero-degree latitude line. This reference frame is used to describe, with respect to the asteroid, the relative state of the spacecraft. The coordinates in this reference frame will therefore be denoted as $(x_R, y_R, z_R)$.

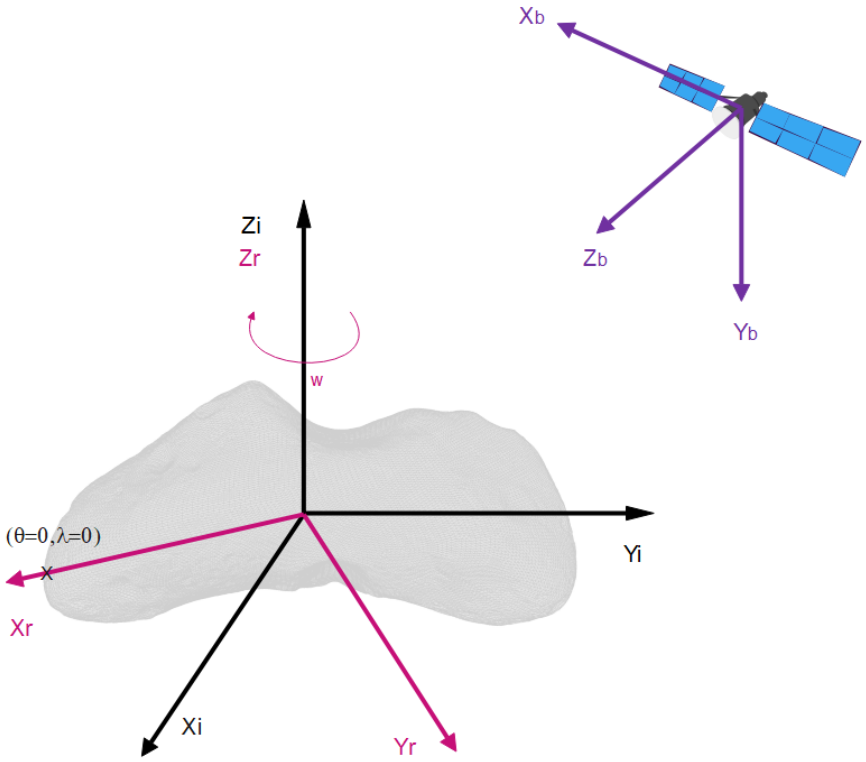


Figure 4.1: Reference frames

**Body Reference frame:** This reference frame is fixed to the spacecraft, with the axis coinciding with the principal inertial moments. The Z-axis is aligned with the line-of-sight of the camera, and parallel to the solar panels is the X-axis. This reference frame is used to explain both the rotational motion and the pointing of the instruments of the spacecraft. The coordinates are denoted by $(x_B, y_B, z_B)$ in this reference frame.

### 4.1.2 Sphere-based coordinates

In addition to Cartesian coordinates used to describe the motion of the spacecraft, sphere-based coordinates are used. These coordinates are fixed to the asteroid system, which means that they are rotating with the asteroid, and are thus determined with respect to the reference frame of the asteroid, as shown in Figure 4.2. The two systems of coordinates are:

**Spherical coordinates:** Consisting of three components, the distance $d$, the colatitude $\Phi$, the angle between the position vector of the Z-axis and the position vector of the spacecraft, and the latitude $\lambda$, the angle between the prime meridian and the position vector projection of the X-Y plane. A triple $(d, \Phi, \lambda)$ can define the coordinates of the spacecraft. This coordinate system enables the asteroid's gravitational field to be computed in a much simpler way.

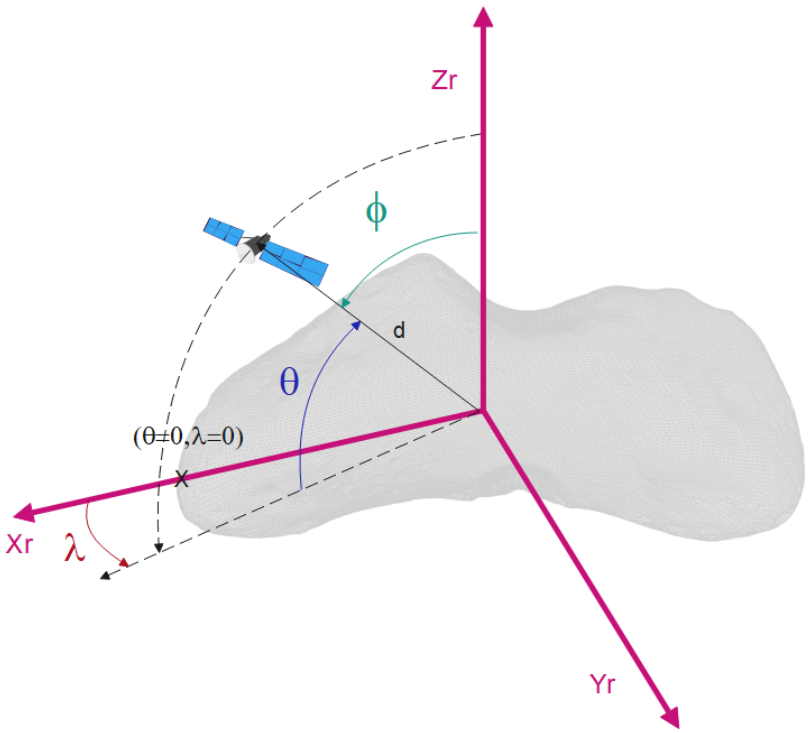


Figure 4.2: Spherical and geographic coordinates system

**Geographical coordinates:** Represented by the $(\theta, \lambda)$ pair, the geographical coordinates provide information on the relative location of the spacecraft projection on the asteroid surface. $\theta$ is the angle of latitude, and $\lambda$ is the angle of longitude. This method is very useful when the asteroid is rotating, to determine the force acting on the spacecraft due to the highly irregular gravity field of the asteroid.

### 4.1.3 Frame transformations

We will need to switch from one reference frame to another in the simulator. This can be done by using a transformation matrix, which enables a vector to be transformed from the perspective of the old reference frame to the new one. The transformation does not alter the vector itself but changes its components to preserve its representation in the new reference frame.

If we consider a $(X, Y, Z)$ reference frame, called A, to which we apply an arbitrary axis rotation, the resulting frame $(X', Y', Z')$, called B, is shown in Figure 4.3. We can write the vector coordinates in the new reference frame, that is:

$$\begin{aligned} r_{X'} &= \mathbf{r} \cdot \mathbf{i}' = (r_X \mathbf{i} + r_Y \mathbf{j} + r_Z \mathbf{k}) \cdot \mathbf{i}' = r_X \mathbf{i} \cdot \mathbf{i}' + r_Y \mathbf{j} \cdot \mathbf{i}' + r_Z \mathbf{k} \cdot \mathbf{i}' \\ r_{Y'} &= \mathbf{r} \cdot \mathbf{j}' = (r_X \mathbf{i} + r_Y \mathbf{j} + r_Z \mathbf{k}) \cdot \mathbf{j}' = r_X \mathbf{i} \cdot \mathbf{j}' + r_Y \mathbf{j} \cdot \mathbf{j}' + r_Z \mathbf{k} \cdot \mathbf{j}' \\ r_{Z'} &= \mathbf{r} \cdot \mathbf{k}' = (r_X \mathbf{i} + r_Y \mathbf{j} + r_Z \mathbf{k}) \cdot \mathbf{k}' = r_X \mathbf{i} \cdot \mathbf{k}' + r_Y \mathbf{j} \cdot \mathbf{k}' + r_Z \mathbf{k} \cdot \mathbf{k}' \end{aligned} \tag{4.1}$$

with $(\mathbf{i}, \mathbf{j}, \mathbf{k})$ and $(\mathbf{i}', \mathbf{j}', \mathbf{k}')$ the unit vector of the original and rotated reference frame respectively. These equations can be written in a more compact way, that is:

$$\begin{pmatrix} r_{X'} \\ r_{Y'} \\ r_{Z'} \end{pmatrix} = \begin{bmatrix} \mathbf{i} \cdot \mathbf{i}' & \mathbf{j} \cdot \mathbf{i}' & \mathbf{k} \cdot \mathbf{i}' \\ \mathbf{i} \cdot \mathbf{j}' & \mathbf{j} \cdot \mathbf{j}' & \mathbf{k} \cdot \mathbf{j}' \\ \mathbf{i} \cdot \mathbf{k}' & \mathbf{j} \cdot \mathbf{k}' & \mathbf{k} \cdot \mathbf{k}' \end{bmatrix} \begin{pmatrix} r_X \\ r_Y \\ r_Z \end{pmatrix} = \mathbf{T_{B/A}} \begin{pmatrix} r_X \\ r_Y \\ r_Z \end{pmatrix} \tag{4.2}$$

with $\mathbf{T_{B/A}}$ the transformation matrix from the reference frame A to the reference frame B. The inverse transformation can be applied by:

$$\begin{pmatrix} r_X \\ r_Y \\ r_Z \end{pmatrix} = \mathbf{T_{A/B}} \begin{pmatrix} r_{X'} \\ r_{Y'} \\ r_{Z'} \end{pmatrix} \tag{4.3}$$

where:

$$\mathbf{T_{A/B}} = \mathbf{T^T_{B/A}} \tag{4.4}$$

Using the direction cosine matrix (DCM) is another way of computing the rotation from a reference frame to another. The unit vectors of the B reference frame, in the A reference frame, can be written as:

$$\begin{aligned} \mathbf{i}' &= \cos\theta_{11}\mathbf{i} + \cos\theta_{21}\mathbf{j} + \cos\theta_{31}\mathbf{k} \\ \mathbf{j}' &= \cos\theta_{12}\mathbf{i} + \cos\theta_{22}\mathbf{j} + \cos\theta_{32}\mathbf{k} \\ \mathbf{k}' &= \cos\theta_{13}\mathbf{i} + \cos\theta_{23}\mathbf{j} + \cos\theta_{33}\mathbf{k} \end{aligned} \tag{4.5}$$

where the $\theta_{ij}$ corresponds to the angles between the corresponding unit vectors, as shown in Figure 4.4. Therefore:

$$\begin{pmatrix} r_{X'} \\ r_{Y'} \\ r_{Z'} \end{pmatrix} = \begin{bmatrix} \cos\theta_{11} & \cos\theta_{2} & \cos\theta_{31} \\ \cos\theta_{12} & \cos\theta_{22} & \cos\theta_{32} \\ \cos\theta_{13} & \cos\theta_{23} & \cos\theta_{33} \end{bmatrix} \begin{pmatrix} r_X \\ r_Y \\ r_Z \end{pmatrix} = \mathbf{C_{B/A}} \begin{pmatrix} r_X \\ r_Y \\ r_Z \end{pmatrix} \tag{4.6}$$

The direction cosine matrix $\mathbf{C_{B/A}}$, which represents the attitude of the B-frame in relation to the A-frame, can be used to transform a vector from a reference frame to another frame.

## 4.2 Asteroid Environment

During the NEAR mission, a spherical harmonics model of the shape and gravity field of 433 Eros was made by Miller et al. (2002). Using radiometric tracking data, optical images and the NEAR laser rangefinder (NLR) to determine the shape, rotational rate and gravity field of Eros, NEAR spacecraft were injected into many different orbits. To determine a 24th degree and order shape model, the NLR and optical data from a 50 km altitude orbit were used. In parallel, the radiometric data, together with the optical data, were used to in the orbit determination process determine the gravity field of Eros up to 15 degrees and order, from a 35 km altitude orbit. The shape model integration given by the NLR shape model, assumed a constant density. Since the results of this model are very close to those obtained by the orbit determination process, it indicates

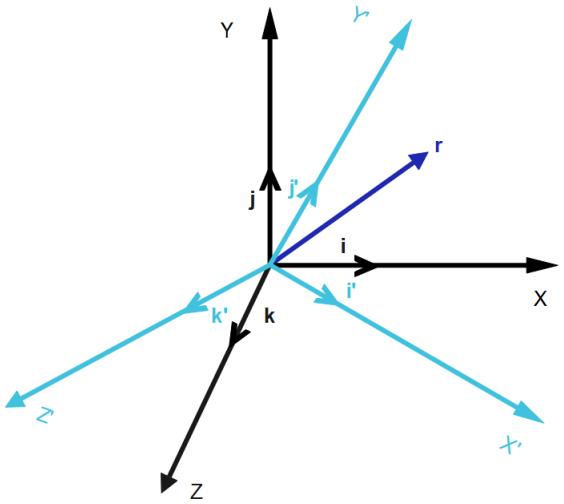


Figure 4.3: Rotation of a reference frame around an arbitrary axis

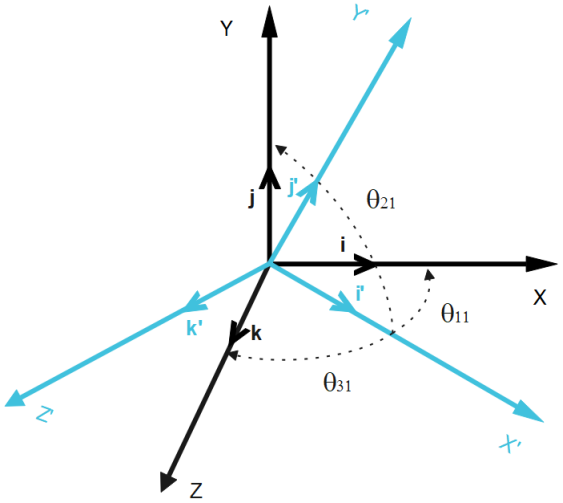


Figure 4.4: Direction cosines angles

that the density of Eros is almost uniform on a large scale (1% variation for 35 km). After the mission, the data collected was post-processed to create more precise models, such as the Chanut et al. (2014) polyhedron shape model and the Garmier et al. (2002) ellipsoid model. To determine stable orbits around Eros, the polyhedron model was used, as shown in Figure 4.12a. Chanut et al. (2014) has identified a minimum radius of 36 km for direct, equatorial and circular stable orbits and a minimum radius of 31 km for any other stable orbit. Only in elliptical orbits can be found stable at lower altitudes.

### 4.2.1 Asteroid gravity field

Asteroids are defined by their complex shape and limited size. This feature, along with the rotational speed of the asteroid, contributes to a complex dynamic situation in the vicinity of asteroids. The gravitational field is relatively weak, but as it is the main source of disturbance near the surface of the asteroid, gravitational disturbances can be very large. They can lead to substantial deviations in the nominal trajectory of a spacecraft. Awareness of this gravitational field may also provide details about the inner structure and mass distribution of the celestial body.

Due to the large perturbations, the spacecraft would face high risks of collision with the surface of the asteroid, if the gravitational field is not modelled correctly. Two models are generally used to model the gravitational field of such bodies, polyhedral modelling and spherical harmonic expansion. Those models have been studied by Werner and Scheeres (1996) who came to the conclusion that polyhedron model was the most accurate model, while harmonics modelling suffered from convergence and accuracy problems. An ellipsoidal harmonic expansion can also be used, as written by Garmier et al. (2002), to model the gravity fields of asteroids with an elongated shape. For Eros, this model leads to more accurate results.

This section will explain the various ways of modelling an asteroid's gravity field, and will provide the gravity field model of Eros with details about the accuracy of these methods and their performance.

#### Point Mass approximation

The simplest way to model the gravity field of a body is to use the point mass approximation. As Newton's Law of Gravitation states, the gravitational force between two point masses distant in the vacuum, is an attractive force and can be written as proportional to the masses and inversely proportional to the square of the distance between the two point masses:

$$\mathbf{F}_{P/Q} = G\frac{m_P m_Q}{d^2}\mathbf{e}_{PQ} \tag{4.7}$$

with $\mathbf{F}_{P/Q}$ the force acting on the body $Q$, by the body $P$, $m_P$ and $m_Q$ masses of the two bodies, $\mathbf{e}_{PQ}$ the unit vector in the direction of the centre of mass of the body 2, and $d$ the distance between the two masses.

Using the second law of Newton, we can write the gravitational acceleration $\mathbf{a}$ due to body $Q$ acting on a body $P$:

$$\mathbf{a}(P) = -Gm_Q\frac{\mathbf{x}_P - \mathbf{x}_Q}{|\mathbf{x}_P - \mathbf{x}_Q|^3} \tag{4.8}$$

where $\mathbf{x}_P$, $\mathbf{x}_Q$ are the position vectors of the bodies $P$ and $Q$, respectively.

If multiple bodies are in the spacecraft environment, the summation of all the individual accelerations enables the identification of the total field strength. This representation is not very accurate, since it does not take into account the effect of the shape of the bodies on the gravitational field, but still yields a good approximation, especially when the bodies are far from the spacecraft. If we consider a volume mass, integrating all the elements $dm = d\Omega$ makes it possible to find the gravitational field of this volume.

Table 4.1: Gravitationnal acceleration acting on a spacecraft located at d=250 km from the centre of the body.

| Body | Point Mass gravitationnal acceleration (d=250 km, m.s$^{-2}$) |
|---|---|
| Eros 433 | $-7.04 \times 10^{-6}$ |
| Itokawa | $-3.74 \times 10^{-11}$ |
| Kleopatra | $-0.0050 \times 10^{-3}$ |

The point mass gravity model, shows a uniform gravitational acceleration for a spacecraft located at a certain distance from the centre. It results in a perfect stable circular orbit when no other disturbances are taken into account. If the distance from the centre of the body is increased, the gravitational acceleration decreases. This model gives the first approximation of the gravity field, since it does not take into account any variation of shape or density within Eros. Despite this, the first approximation is sufficient to characterise the intensity of the gravity field, which is very low due to the small mass and size of Eros. The gravitational disturbances due to the irregular shape or density of the asteroid are getting much smaller by increasing the distance to the centre of Eros. The point mass approximation is more than adequate at a sufficient distance from the centre to simulate the effect of the asteroid on the dynamics of a spacecraft. The gravitational field intensity of the asteroids Kleopatra and Itokawa are shown as a comparison in Table 4.1. We can see that the Itokawa gravity field is much smaller than the other two bodies gravity field, mainly because of the difference in size and mass.

### Spherical harmonics

A way of modelling the gravitational field of a celestial body is the spherical harmonic representation. It consists of an expansion of the gravitational potential into a harmonic series, by computing the harmonic coefficients (Werner and Scheeres, 1996). Harmonics coefficients can be estimated using radio tracking data, NLR data or other measurements techniques. The gravity potential can be approximated up to a certain order and degree. Some convergence problems can be found by computation for the gravity field inside the sphere, therefore the spherical harmonic expansion can only be used outside of the reference sphere, the radius of this sphere usually being the maximum radius of the body.

The Laplace equation of the gravity potential in spherical coordinates can be written has (Wakker, 2015):

$$V = \frac{GM}{R}\left\{\sum_{n=0}^{\infty}\sum_{m=0}^{\infty}\left(\frac{R}{r}\right)^{n+1}\bar{P}_{nm}(\sin\theta)[\bar{C}_{nm}\cos(m\lambda)+\bar{S}_{nm}\sin(m\lambda)]\right\} \tag{4.9}$$

With $r$ the distance between the spacecraft and the centre of mass of the body, $R$ the reference radius, which is most of the time the maximum radius of the body, and ($\lambda$,$\theta$) longitude and latitude respectively. $\bar{P}_{nm}$ represent the normalized Legendre associated polynomials of the first kind, and $\bar{C}_{nm}$, $\bar{S}_{nm}$ are called spherical harmonics coefficient. Those coefficients are zero to the first order if the centre of mass of the body coincides with the origin of the chosen body-fixed frame. By increasing the order and degree with

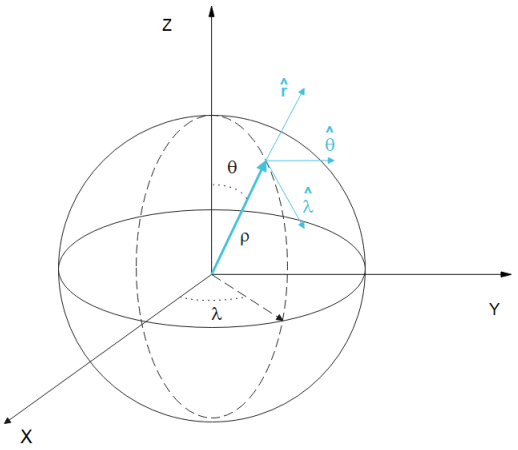


Figure 4.5: Spherical coordinates.

the order of expansion, we can obtain complex models of the gravity field, as we can see in Figure 4.6. The zonal harmonics corresponds to $m = 0$, and therefore the superposition of the Legendre polynomials describe variations with latitude. The sectorial harmonics are defined by $n = m$, and divide the sphere into sectors. For $n \neq m$, the tesseral harmonics are described and thus reflect how the number of nodal lines is distributed over the nodal meridians and parallels.

The acceleration acting on the spacecraft can be computed using the gradient of the potential in spherical coordinates:

$$\mathbf{g_A} = \nabla V = \frac{\partial V}{\partial r}\hat{\mathbf{r}} + \frac{1}{r}\frac{\partial V}{\partial \theta}\hat{\boldsymbol{\theta}} + \frac{1}{r\sin\theta}\frac{\partial V}{\partial \lambda}\hat{\boldsymbol{\lambda}} \tag{4.10}$$

where $(\hat{\mathbf{r}}, \hat{\boldsymbol{\theta}}, \hat{\boldsymbol{\lambda}})$ are the unit vectors in spherical coordinates, as shown in Figure 4.5.

Analysis of low order and degree spherical harmonics coefficients

The effect of low order spherical hamonic terms may be related to the shape, mass and density characteristics of Eros. The analysis of these terms can provide important information on the shape and distribution of mass within the attracting body, as well as useful information on the centre of gravity position.

**Degree** $n = 1$

The terms of the first order spherical harmonics relate to the position of the centre of mass of the attracting body. If the coefficient $c_{10}$ is non-zero, the centre of mass of the body is shifted in the direction of the z-axis, which is parallel to the main axis of rotation. The coefficients $c_{11}$ and $s_{11}$ are related to the shift of the centre of gravity in the direction of the x-and y-axis. These coefficients provide useful information on the distribution of mass within the attracting body.

**Degree** $n = 2$

[1]Image taken from: http://users.umiacs.umd.edu/ ramani/cmsc878R/09_15_11_Factorization_Laplace_Helmholtz_Lecture5.pdf

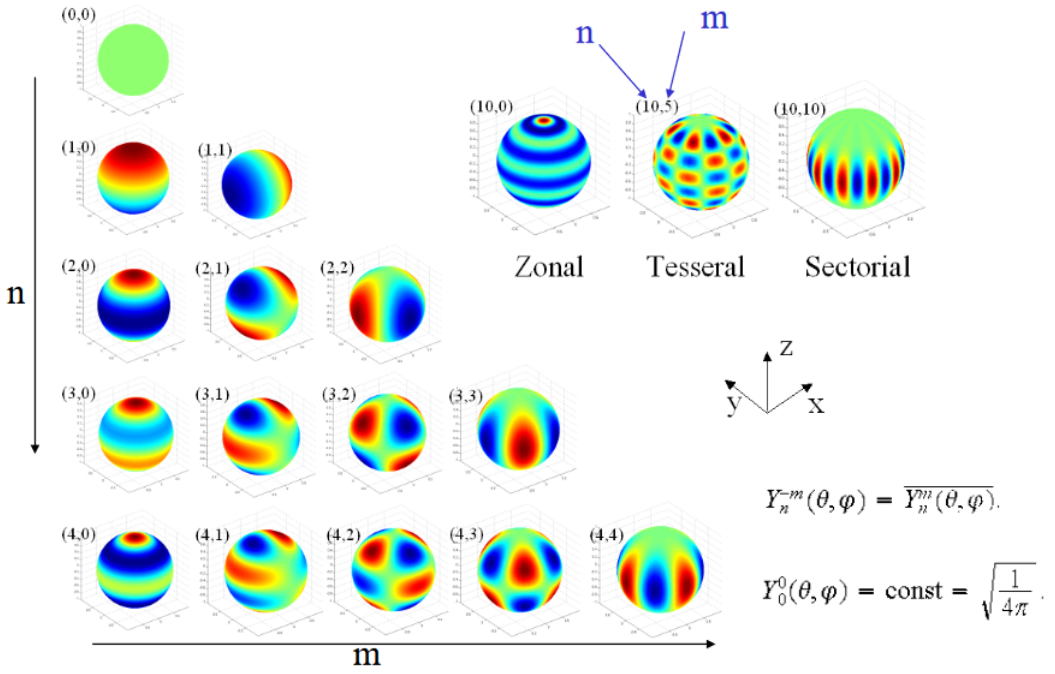


Figure 4.6: Spherical harmonics modelling representation. Red areas represent positive values while blue areas represents negative values.[1]

The $c_{20}$ coefficient is associated with the $J_2$ perturbation. It is one of the greatest disturbances that can be experienced around the earth. In the equatorial region, the coefficient $c_{20}$ represents a mass excess and is related to the flattening of the poles of the attracting body. For the Earth, this coefficient magnitude is ten times greater than any other coefficient. The $c_{21}$ and $s_{21}$ coefficients represent a mass excess and a deficiency in the opposite northern and southern quadrants. If these coefficients are different from zero, the inertia axis may rotate around the rotation axis, and the body may rotate. This effect is called a precession. The coefficients $c_{22}$ and $s_{22}$ are related to the sector quadrants and represent the ellipticity of the equator in the x and y directions. The ellipticality of the equator can be derived directly from the analysis of these coefficients.

**Degree $n = 3$**

The last coefficient that can be related to the shape of the attracting body is the $c_{30}$ coefficient. The $J_3$ perturbation due to this coefficient is called a pear-shaped perturbation, because it represents a pear-shaped distribution of the body's mass.

**Degree $n > 3$**

Higher degree spherical harmonics terms can not be neglected when considering orbiting around complex shaped bodies. The $c_{40}$ coefficient, although not related to any kind of geometry, allows the potential of an ellipsoid to be refined, while the other degrees may have a non-negligible effect on the dynamics of the spacecraft.

Gravitational and shape model of Eros 433 In the work of Miller et al. (2002), the gravitational field, the shape and the rotational rate of Eros have been determined using data obtained during the Near-Shoemaker mission by direct integration of the equations

Table 4.2: Gravity harmonics coefficients of Eros from Near-Shoemaker archives

(a) NLR coefficients

| Coefficient ($R_0 = 16.0$ km) | Solution: Spacecraft dynamics | Solution: Shape model integration |
|---|---|---|
| $C_{10}$ | 0 | 0.001175 |
| $C_{11}$ | 0 | −0.000348 |
| $S_{11}$ | 0 | 0.000088 |
| $C_{20}$ | −0.052478 (.000051) | −0.052851 |
| $C_{21}$ | 0 | 0.000102 |
| $S_{21}$ | 0 | 0.000012 |
| $C_{22}$ | 0.082538 (.000061) | 0.083203 |
| $S_{22}$ | −0.027745 (.000035) | −0.028033 |
| $C_{30}$ | −0.001400 (.000030) | −0.001747 |
| $C_{31}$ | 0.004055 (.000006) | 0.004083 |
| $S_{31}$ | 0.003379 (.000006) | 0.003404 |
| $C_{32}$ | 0.001792 (.000016) | 0.002129 |
| $S_{32}$ | −0.000686 (.000016) | −0.000836 |
| $C_{33}$ | −0.010337 (.000027) | −0.010456 |
| $S_{33}$ | −0.012134 (.000027) | −0.012247 |
| $C_{40}$ | 0.012900 (.000070) | 0.013077 |
| $C_{41}$ | −0.000106 (.000014) | −0.000145 |
| $S_{41}$ | 0.000136 (.000015) | 0.000165 |
| $C_{42}$ | −0.017495 (.000035) | −0.017656 |
| $S_{42}$ | 0.004542 (.000030) | 0.004589 |
| $C_{43}$ | −0.000319 (.000044) | −0.000312 |
| $S_{43}$ | −0.000141 (.000044) | −0.000195 |
| $C_{44}$ | 0.017587 (.000062) | 0.017729 |
| $S_{44}$ | −0.008939 (.000061) | −0.009048 |

(b) Shape model integration

| n | m | $\bar{C}_{nm}$ | $\bar{S}_{nm}$ |
|---|---|---|---|
| 0 | 0 | 1 | 0 |
| 1 | 0 | $1.17578583\times10^{-3}$ | 0 |
| 1 | 1 | $-3.48442759\times10^{-4}$ | $8.76645269\times10^{-5}$ |
| 2 | 0 | $-5.28514887\times10^{-2}$ | 0 |
| 2 | 1 | $1.02129351\times10^{-4}$ | $8.31482741\times10^{-2}$ |
| 2 | 2 | $1.17164118\times10^{-5}$ | $-2.81976945\times10^{-2}$ |
| 3 | 0 | $-1.74665867\times10^{-3}$ | 0 |
| 3 | 1 | $4.08678974\times10^{-3}$ | $-8.40192875\times10^{-4}$ |
| 3 | 2 | $3.40082018\times10^{-3}$ | $-1.04925252\times10^{-2}$ |
| 3 | 3 | $2.12743267\times10^{-3}$ | $-1.22164205\times10^{-2}$ |
| 4 | 0 | $1.30771127\times10^{-2}$ | 0 |
| 4 | 1 | $-1.44936922\times10^{-4}$ | $-3.13023342\times10^{-4}$ |
| 4 | 2 | $1.647971980510\times10^{-4}$ | $-1.94651001\times10^{-4}$ |
| 4 | 3 | $-1.76473039\times10^{-2}$ | $1.76937286\times10^{-2}$ |
| 4 | 4 | $4.62396512\times10^{-3}$ | $-9.11827527\times10^{-3}$ |

of motion. Another spherical harmonics model was built during the first phase of the Eros approach, where radiometric data was used to approximate the shape of Eros, and the spherical harmonic coefficients were deducted from the shape model.

The coefficients of the spherical harmonics for Eros were obtained from the Near-Shoemaker archives[2], obtained by integration of the shape model. The reference frame used to compute the spherical harmonics coefficients was based on the IAU94 reference frame (Davies et al., 1996), with a declination of 17.232°, a right ascension of 11.363°and a prime meridian at 326°. Using the spherical harmonic coefficients up to degree 22 of the gravity model solution derived from the numerical integration of the shape model, the Eros gravity potential and gravity strength may be determined. The spherical harmonic coefficients used by Miller et al. (2002) and the models are shown in Table 4.2 only up to degree and order 4, with a reference density of 2.6212 g.cm$^3$. A number of conclusions can be drawn from a single observation of the first coefficients. Since the value of $C_{00}$ is not set to zero, this means that the centre of gravity is different from the centre of mass of Eros. In fact, the centre of gravity shift is small, equal to $[-9.6, +2.4, +32]$ metres, in x, y and z respectively. The values $C_{21}$ and $S_{21}$ are responsible for the off-diagonal moment of inertia. These coefficients are different from zero in our representation, which means that the reference frame is rotated in comparison to the spherical equatorial reference frame.

The spherical harmonics model, taking into account the irregular shape of Eros, has a higher resolution than the point mass gravity model. Gravitational disturbances are stronger when the spacecraft is above the two elongated poles and smaller when the

[2]https://sbn.psi.edu/pds/resource/nearbrowse.html accessed 05-06-2020

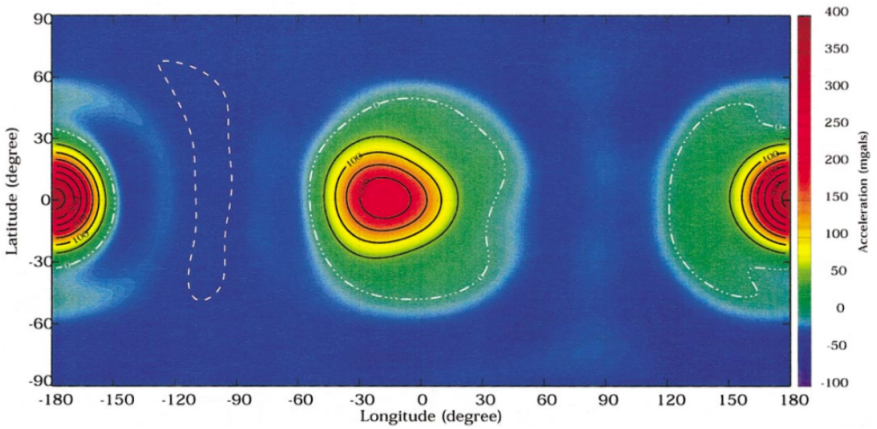


Figure 4.7: Radial acceleration of Eros gravity field, up to degree and order 8, on a sphere of 16 km radius (Miller et al., 2002).

spacecraft is between the two poles, as shown in Figure 4.7, where the gravity field of Eros has been computed up to order and degree 8, on a sphere of 16 km radius.

The resolution of the gravity field can have a huge impact on a dynamic model. In reality, the resolution of the Eros gravity field is infinite, which means that the order and degree of expansion are infinity. It is not possible to have such an infinite resolution in our model, as it would take an infinite amount of time. Increasing the resolution, and therefore the order and degree of expansion, means increasing the accuracy, but also the time of propagation and estimation. It is therefore important to determine the degree and order such as the approximation of the gravity field is sufficient for the study and for which the modelling time is as short as possible. It can be seen in 4.8 where spherical harmonics up to degrees 2 and 22 are compared. Indeed, the gravitational map of the spherical harmonics at degree and order 22 shows a higher resolution. It is also important to establish a link between the distance to the centre, the resolution and the degree of expansion of the spherical harmonics. Increasing the distance to the centre of Eros, the disturbances coming from the irregular shape and density of Eros will fade away. As can be seen in Figure 4.9, the gravity maps look more uniform for the 1500 km orbit sphere. In other words, if we are far enough from the centre of Eros, we can consider the gravitational field of Eros to be uniform. Getting closer to the surface, the major disturbances will begin to disrupt the motion of the spacecraft, and the gravity resolution 'felt' by the spacecraft will increase by decreasing the distance to the surface of Eros. Wee can see by comparing Figure 4.10 and Figure 4.8b, that the 2nd order and degree gravity maps looks a lot like the 22 order and degree map. It is widely known that one of the main disturbances that a spacecraft may encounter is the $J_2$ disturbance, which is related to the $c_{20}$ coefficient. This disturbance is related to the flattening of the body. While it can only be appropriate to take the $J_2$ disturbance around Earth, it can be seen that for Eros, other disturbances can have a major effect on the motion of the spacecraft.

### Polyhedron modelling

Polyhedron modelling is an accurate way to model highly irregular-shaped bodies such as asteroids. It consists of a 3D model of the surface, most of the time assuming constant

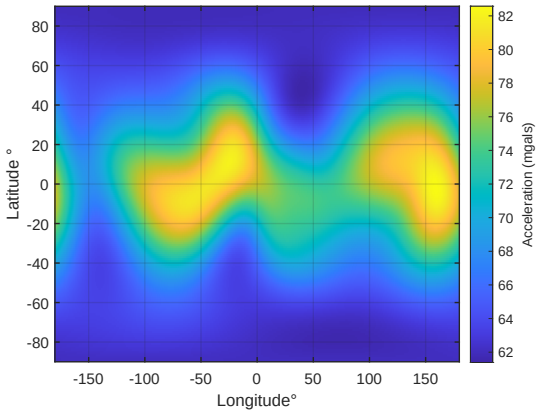


(a) Gravity acceleration, spherical harmonics up to degree 22.

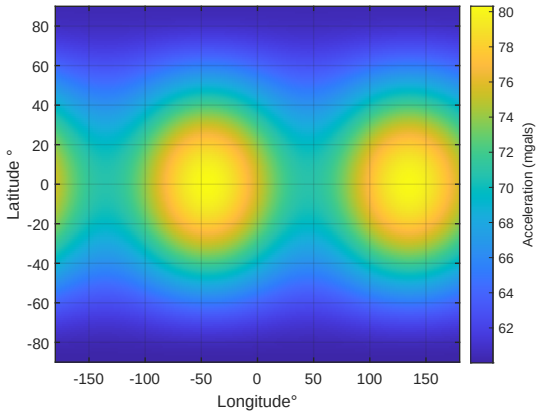


(b) Gravity acceleration, spherical harmonics up to degree 2.

Figure 4.8: Acceleration of Eros gravity field, up to degree and order 2 and 22, using the coefficients collected during the Near mission.

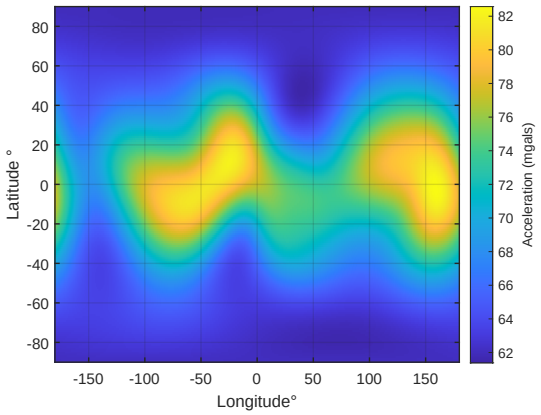


(a) Gravity acceleration on a sphere of 25 km radius.

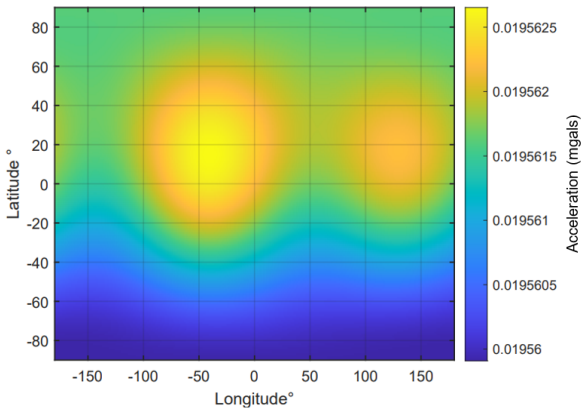


(b) Gravity acceleration on a sphere of 1500 km radius.

Figure 4.9: Acceleration of Eros gravity field, up to degree and order 22, using the coefficients collected during the Near mission.

density inside the body (which is, most of the time, not the case). This way of modelling the gravity field has been studied by Werner and Scheeres (1996) who have shown that this method leads to better results, and allows to model the gravity field inside of the sphere, which is not the case for the spherical harmonics model. A polyhedron is a solid model composed of multiple plane faces like triangles. Every face is connected through its straight edges or at its vertices (isolated points). This model leads to even better results than the spherical harmonics model, when the shape is highly irregular, such as the shape of Kleopatra. The accuracy of the model is fully dependent on the number of faces chosen to model the body and the density distribution. Therefore, increasing the number of faces leads to a more accurate model. The expression of the gravity potential

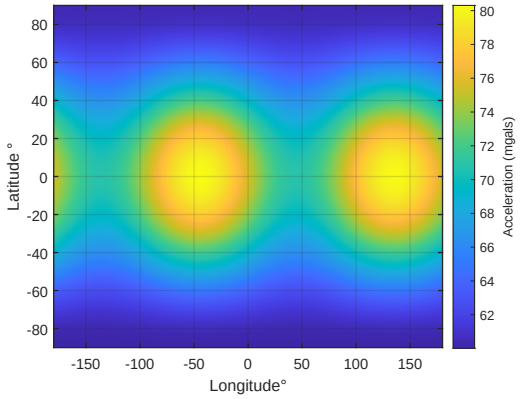


Figure 4.10: Acceleration of Eros gravity field, up to degree and order 2, on a 25km sphere.

has been derived by Werner and Scheeres (1996), and can be written:

$$V = \frac{1}{2}G\rho \sum_{e \in edges} \mathbf{r}_e \mathbf{E}_e \mathbf{r}_e L_e - \frac{1}{2}G\rho \sum_{f \in faces} \mathbf{r}_f \mathbf{E}_f \mathbf{r}_f \omega_f \tag{4.11}$$

with :

$$\mathbf{E_e} = \mathbf{n}_A (\mathbf{n}_{12}^A)^T + \mathbf{n}_B (\mathbf{n}_{21}^B)^T \tag{4.12}$$

$$\mathbf{E_f} = \mathbf{n}_f (\mathbf{n}_f)^T \tag{4.13}$$

$$L_e = \ln \frac{r_i + r_j + e_{ij}}{r_i + r_j - e_{ij}} \tag{4.14}$$

$$\omega_f = \arctan \frac{\mathbf{r}_i \cdot \mathbf{r}_j \times \mathbf{r}_k}{r_i r_j r_k + r_i(\mathbf{r}_j \cdot \mathbf{r}_k + r_j(\mathbf{r}_k \cdot \mathbf{r}_i) + r_k(\mathbf{r}_i \cdot \mathbf{r}_j)} \tag{4.15}$$

With $G$, gravitational parameter, $\rho$ mean density of the body, $\mathbf{r}_e$ and $\mathbf{r}_f$ are the distances from the edges and the face respectively to the spacecraft. $\mathbf{n}_A$, $\mathbf{n}_B$ and $\mathbf{n}_f$ are the unit vectors normal to the faces, and $\mathbf{n}_{12}^A$ and $\mathbf{n}_{21}^B$ are the unit vectors normal to the edges of the associated faces as shown by the Figure 4.11. The dimensionless factor $\omega_f$ summed over the surface, gives a solid angle, which is a very useful angle in the detection of possible collisions of the spacecraft with the asteroid. Vectors $\mathbf{r_i}$, $\mathbf{r_j}$, and $\mathbf{r_k}$ are shown in Figure 4.11, and $e_{ij}$ is the length of the edges. The gravitational attraction can be written as:

$$\mathbf{g_p} = \nabla V = -G\rho \sum_{e \in edges} \mathbf{E}_e \mathbf{r}_e L_e + G\rho \sum_{f \in faces} \mathbf{E}_f \mathbf{r}_f \omega_f \tag{4.16}$$

Although this method leads to a highly accurate model of the shape of the asteroid, and therefore to a highly accurate model of the gravity field, it is computationally and memory demanding when asking for high resolutions. The spherical harmonics model

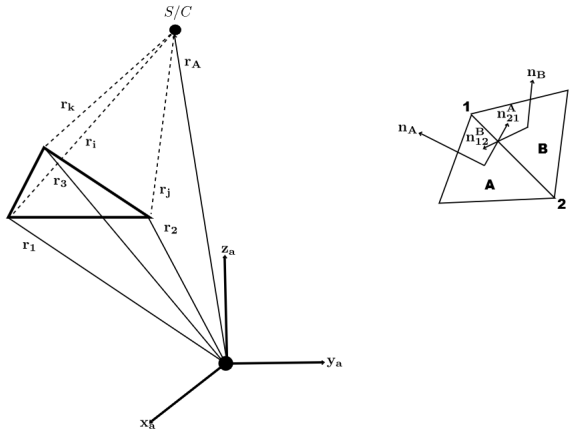


Figure 4.11: Polyhedron gravity model elements (Werner and Scheeres, 1996)

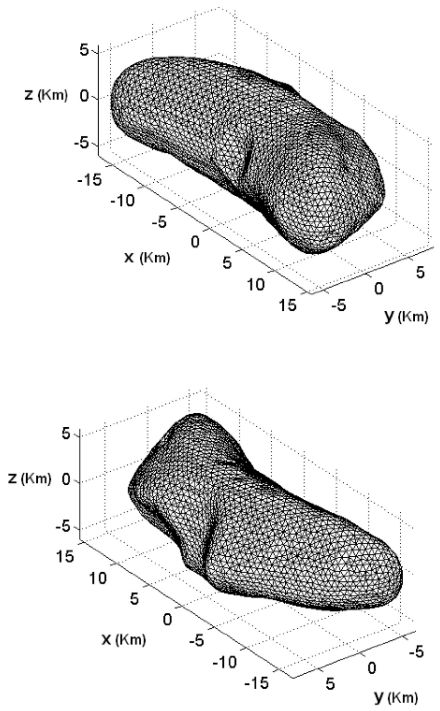


(a) Polyhedron model of 433 Eros, two perspectives (Chanut et al., 2014).

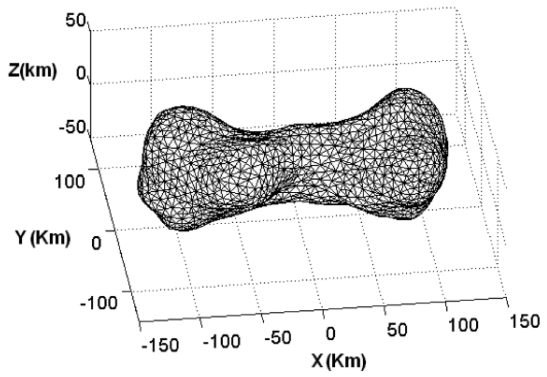


(b) Polyhedron model of the asteroid Kleopatra (Chanut et al., 2015).

Figure 4.12: Polyhedron models

must be preferred because of its computational efficiency when the resolution is the same, i.e. the number of faces selected for the polyhedron leads to approximately the same results compared to the spherical harmonics model. The choice of the model should therefore be made according to the accuracy required, taking into account the storage and performance of the on-board computer.

### 4.2.2 Solar environment

In the vicinity of a spacecraft, the complex environment is significantly disturbed, which has an important impact on the behaviour of the spacecraft. Asteroid missions are highly sensitive to the numerous disturbing spacecraft accelerations, including the third-body perturbation. We will only consider the major disturbances the spacecraft will experience in our simulator model i.e., the disturbances due to the Sun. Gravity fields of asteroids are relatively small, because of their small size, and the SRP is now a significant disruption to the proximity of such asteroids. This effect can, in certain peculiar situations, be stronger than the than the third-body perturbation. The SRP accelerations are pushing the spacecraft in the opposite direction from the Sun's position.

#### Third-body perturbation

Because of its heavy mass, the Sun has a non-negligible effect on the dynamics of a spacecraft in the Solar System. We may opt to view the Sun as the primary attractive body, or only as a disturbing body, depending on the distances between the asteroid, the Sun and the spacecraft. Two imaginary limits, the Hill's sphere and the Sphere of Influence can be used to describe the impact of the Sun in the proximity of the asteroid. The dynamical problem can be reduced to the well-known two-body problem under the asteroid's Sphere of Influence, where only the gravitational influence of Eros is taken into account, and where the Sun's gravitational effect is negligible. The region above this limit, where the Sun can be called a disturbing body, is defined by the Hill sphere. Indeed, the sphere of influence is included within Hill's sphere. The acceleration acting on the spacecraft taking into account the point mass gravity effect of the main-attractive body M, and the point-mass gravity effect of the perturbing body P can be written as:

$$\ddot{\mathbf{r}}_{\mathbf{s}} = -GM_m \frac{\mathbf{r_s}}{||\mathbf{r}||^3} + GM_p\left(\frac{\mathbf{r_{ps}}}{||\mathbf{r_{ps}}||^3} - \frac{\mathbf{r_p}}{||\mathbf{r_p}||^3}\right) \tag{4.17}$$

where:

$$\begin{aligned} \mathbf{r_p} &= x_p - x_m \\ \mathbf{r_s} &= x_s - x_m \\ \mathbf{r_{ps}} &= x_s - x_p \end{aligned} \tag{4.18}$$

Are the vectors between the spacecraft, the Sun and the main attractive body, as shown in Figure 4.13.

The perturbing acceleration, $\mathbf{a_p}$ is maximum when the three bodies are aligned. The SOI can be computed using the fact that, on the boundaries we must satisfy:

$$\frac{\mathbf{a_{p,Sun}}}{\mathbf{a_{main,body}}} = \frac{\mathbf{a_{p,body}}}{\mathbf{a_{main,Sun}}} \tag{4.19}$$

Therefore:

$$r_{SOI} = ||\mathbf{r_p}||\left(\frac{M_{main}}{M_{Sun}}\right)^{\frac{2}{5}} \tag{4.20}$$

The sphere of Hill can be computed using:

$$r_H \approx a(1-e)\left(\frac{M_{main}}{3M_{Sun}}\right)^{\frac{1}{3}} \tag{4.21}$$

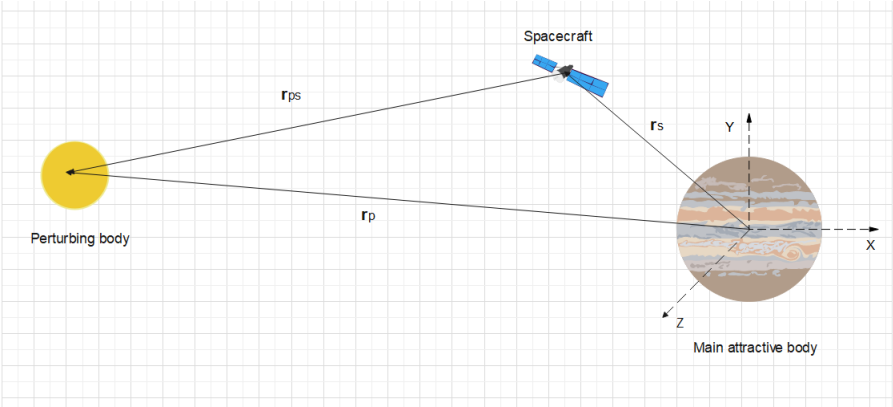


Figure 4.13: Third-body perturbation geometry

with a the semi-major axis and e the eccentricity of the orbit of the lightest body around the more massive body. For Eros, $r_H \approx 1752$ km and $r_{SOI} \approx 352$ km. These values are only indicative, because due to the shape of Eros, the calculation does not take into account the irregular field of gravity, but can give a first approximation of what we expect.

### Solar-radiation pressure

The SRP can have a great influence on a spacecraft trajectory, and can even be dominant over Solar gravitation, especially for large spacecraft. Several manoeuvers can be done to differentiate these two perturbations, to characterise them separately. At a certain distance from the asteroid, the SRP is twice the effect of a gravitational disturbance due to the asteroid, which allows this perturbation to be modelled, removed from the navigation filter, and an accurate model of the asteroid's gravity field can be developed later on in the mission.

Several models can be used to model the Solar radiation pressure as shown by Jean et al. (2019). The model chosen is very important, because the effect of the SRP can lead to large periodic variations. Modifications in the orbital elements can be predicted using the Lagrange planetary equations and modelled, as shown by Scheeres (1999).

If the spacecraft can be decomposed into illuminated surfaces, the sum of force resultant of the SRP over the N illuminated planes can be determined by Markley and Crassidis (2013) :

$$\mathbf{F}_{SRP} = -P_{\odot} \sum_{i=1}^{N} \cos\theta_i A_i ((1-\epsilon)\mathbf{e}_{\odot,i} + 2\epsilon \cos\theta_i \mathbf{n}_i) \tag{4.22}$$

$P_{\odot}$ is the Solar radiation pressure, $\theta_i$ is the angle of incidence of the incoming radiation over the $i^{th}$ plane, $A_i$ is the area of the $i^{th}$ plane, $\mathbf{e}_{\odot,\mathbf{i}}$ and $\mathbf{n_i}$ are unit vectors, as shown in Figure 4.14. The SRP torque, torque induced by the SRP force can be computed as

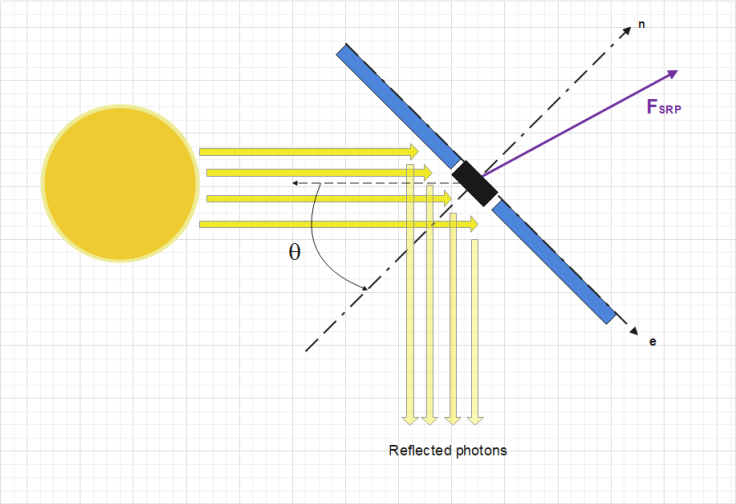


Figure 4.14: Solar radiation pressure

follows (Mukundan, 1990):

$$\mathbf{T}_{SRP} = \begin{pmatrix} U_{cp} \\ V_{cp} \\ W_{cp} \end{pmatrix} \times \mathbf{F}_{SRP} \tag{4.23}$$

with $(U_{cp}, V_{cp}, W_{cp})$ the coordinates of the centre of pressure. To minimise the effect of the SRP pressure, some orbits have to be preferred to the others due to their stability with respect to this perturbing acceleration. For example, orbits that are included in the ecliptic plane and in the Solar plane-of-sky are shown to be more stable in their orbital elements (Scheeres, 1999).

Since we do not dispose of a real spacecraft and asteroid to test our navigation software, their dynamics need to be modelled. This chapter will present the design and architecture of the simulator whose main objectives are to generate the state of the spacecraft as well as the attitude of the spacecraft and the asteroid with respect to the inertial frame. It will detail the concepts and architecture of every part of the simulator. The simulator is divided into two main modules, the asteroid dynamics and the spacecraft dynamics.

## 4.3 Asteroid kinematics

The motion of the asteroid results in a coupling of its trajectory around the Sun, with its its rotation. In the work of Souchay et al. (2003), it has been shown that the obliquity angle, i.e., the angle between the perpendicular to the orbital plane and the rotation axis, is approximately 89°for Eros, resulting in a very low precession rate. We will therefore neglect this precession effect, taking care only of the main rotation. The rotation rate of Eros is believed to be constant, revolving around the Z-axis, and equal to 5.27 h.

According to Markley and Crassidis (2013), the attitude of the asteroid can be computed at each time using the following relation:

$$\dot{\mathbf{C}}_{\mathbf{A/I}} = -\boldsymbol{\omega}_{\boldsymbol{A/I}} \times \mathbf{C}_{\mathbf{A/I}} \tag{4.24}$$

with $\mathbf{C}_{\mathbf{A/I}}$ the direction cosine matrix representing the attitude of the asteroid with respect to the inertial frame, and $\boldsymbol{\omega}_{\boldsymbol{A/I}}$ is the rotational rate vector of the asteroid with respect to the inertial frame, expressed in the asteroid frame. The asteroid attitude is very useful to transform the state and measurements vector from the body frame to the inertial frame, when needed.

## 4.4 Spacecraft properties

The spacecraft to be used in the simulations is similar to the Near spacecraft and has a total mass of 818 kg, with a dry mass of 487 kg, which means that 331 kg of propellant is carried by the spacecraft. The mass is a very important parameter to take into account during the spacecraft design, to reduce the amount of propellant that is needed for the maneuvers. A total $\Delta v$ of 1450 m/s can be produced by the Near spacecraft[3], which is composed of an octogonal body carrying all the instruments, and four rectangular solar panels, as shown by the figure 4.15.

The dimension of the body are resumed in the Table 4.3. The spacecraft reference frame used is shown in the Figure 4.15 and the origin is located at the centre of mass of the body.

The solar panels are attached to the body at the points (0 0.85 1.7), (0 -0.85 1.7), (-0.85 0 1.7) and (0.85 0 1.7) in this reference frame. Therefore, the total length of the body in the X and Y-axis is 5.3 m.

The moments of inertia can be calculated using the parallel axis theorem, since the spacecraft can be divided into two simple bodies, namely the solar panels and the cubic-shaped body. The mass of the solar panels is $M_s = 46.1$ kg each and the octogonal-shaped body has a mass of $M_b = 302.6$ kg. The inertia tensor for the main body can, therefore, be calculated as follows:

$$\mathbf{I_b} = \begin{bmatrix} \frac{1}{12}M_b(l_y^2 + l_z^2) & 0 & 0 \\ 0 & \frac{1}{12}M_b(l_x^2 + l_z^2) & 0 \\ 0 & 0 & \frac{1}{12}M_b(l_y^2 + l_x^2) \end{bmatrix} \tag{4.25}$$

Table 4.3: Dimensions of Near spacecraft

| | Body | Solar Panels |
|---|---|---|
| X dimension | 1.7 m | 1.2 m |
| Y dimension | 1.7 m | 1.8 m |
| Z dimension | 1.7 m | |

[3]https://nssdc.gsfc.nasa.gov/planetary/near.html Accessed on: 23-05-2020

where $M_b$ is the mass of the body, $l_x$, $l_y$ and $l_z$ are the X, Y, and Z-dimension respectively. Therefore, after replacing the terms by their numerical values, we can write the inertia tensor for the cubic-shape body:

$$\mathbf{I_b} = \begin{bmatrix} 145.8 & 0 & 0 \\ 0 & 145.8 & 0 \\ 0 & 0 & 145.8 \end{bmatrix} \text{kg.m}^2 \tag{4.26}$$

Because the solar panels are shifted with respect to the main rotation axis, the calculation of their inertial tensor should include a correction. In addition, with respect to the other length, the dimension of the solar panels on the Z-axis is negligible, and is assumed to be zero. The inertia tensor can be calculate for the solar panels located around the X-axis and for those around the Y-axis.

$$\mathbf{I_{sx}} = \begin{bmatrix} \frac{1}{12}M_s d_y^2 + M_s \lambda_x^2 & 0 & 0 \\ 0 & \frac{1}{12}M_s d_x^2 & 0 \\ 0 & 0 & \frac{1}{12}M_s (d_y^2 + d_x^2) \end{bmatrix} \tag{4.27}$$

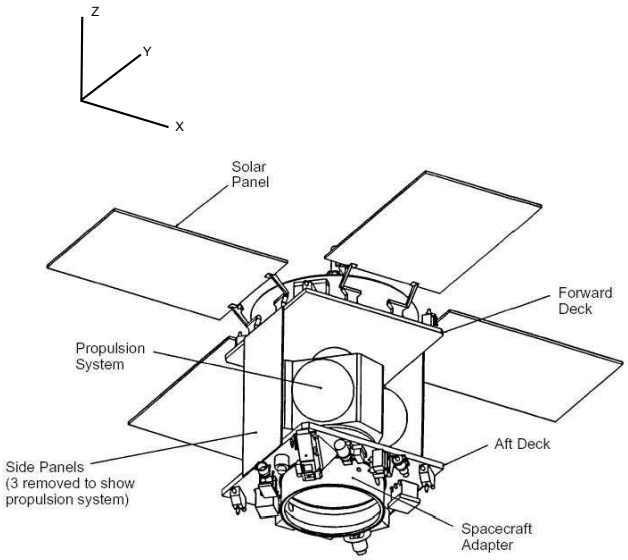


Figure 4.15: Near-Spacecraft spacecraft characteristics (Credit : NASA)

$$\mathbf{I_{sy}} = \begin{bmatrix} \frac{1}{12}M_s d_y^2 & 0 & 0 \\ 0 & \frac{1}{12}M_s d_x^2 + M_s \lambda_y^2 & 0 \\ 0 & 0 & \frac{1}{12}M_s (d_y^2 + d_x^2) \end{bmatrix} \tag{4.28}$$

with $d_x$, $d_y$, $d_z$ the dimensions of the solar panels along the X, Y, and Z axis respectively, and $\lambda_x$, $\lambda_y$ the displacement of their rotation axis along the X and Y axis respectively, with a value of 1.2 m for both. Therefore, the inertia tensor of a unique solar panel located at X-axis is:

$$\mathbf{I_{sx}} = \begin{bmatrix} 78.8 & 0 & 0 \\ 0 & 5.5 & 0 \\ 0 & 0 & 17.9 \end{bmatrix} \text{kg.m}^2 \tag{4.29}$$

and for the solar panels at the Y-axis:

$$\mathbf{I_{sy}} = \begin{bmatrix} 5.5 & 0 & 0 \\ 0 & 78.8 & 0 \\ 0 & 0 & 17.9 \end{bmatrix} \text{kg.m}^2 \tag{4.30}$$

and for the total body:

$$\mathbf{I_{total}} = \mathbf{I_b} + 2\mathbf{I_{sx}} + 2\mathbf{I_{sy}} = \begin{bmatrix} 230.2 & 0 & 0 \\ 0 & 230.26 & 0 \\ 0 & 0 & 163.7 \end{bmatrix} \text{kg.m}^2 \tag{4.31}$$

Comparing these results with other spacecrafts found in literature, such as the mission developed by Gasbarri and Pisculli (2015), where the inertial tensor is the following:

$$\mathbf{I_p} = \begin{bmatrix} 12540 & 0 & 0 \\ 0 & 1109 & 0 \\ 0 & 0 & 12431 \end{bmatrix} \text{kg.m}^2 \tag{4.32}$$

and the Envisat (ESA's veteran satellite) inertia tensor (Virgili et al, 2014):

$$\mathbf{I_{Envisat}} = \begin{bmatrix} 170230 & 0 & 0 \\ 0 & 124825 & 0 \\ 0 & 0 & 129112 \end{bmatrix} \text{kg.m}^2 \tag{4.33}$$

We can assume that our results are within the range of feasibility since it depends on the size of the spacecraft. The last technical aspect that needs to be taken into account in our study is the spacecraft's reflectivity. For determining the reflection properties of the spacecraft, a simple model, consisting of a cubic shape for the body and rectangular plates with the dimensions of the solar panels, can be used. The model consists, therefore, of 8 faces-4 for the main body and 4 for the two solar panels-with 4 vertices for each face. The reflectivity of the solar panels is $\epsilon = 0.21$ as written by Montenbruck and Gill (2001), and the body has a reflectivity of $\epsilon = 0.5$, higher to avoid excessive heating and structural damage than for the solar panels.

## 4.5 Spacecraft dynamics

In the simulator, the actual position, attitude and velocity of the spacecraft are produced at each time. To do so, the forces and torques acting on the spacecraft are integrated to find the state vector of the spacecraft. This method will be detailed in this section.

### 4.5.1 Equations of motion

The equations of motion for a spacecraft orbiting an asteroid are the following:

$$\begin{aligned} \frac{d\mathbf{x}}{dt} &= \mathbf{v} \\ \frac{d\mathbf{v}}{dt} &= \mathbf{a} = \frac{\mathbf{F}}{m} \end{aligned} \tag{4.34}$$

where $\mathbf{x}$, $\mathbf{v}$, $\mathbf{a}$ are the position, velocity and acceleration vectors respectively, and $\mathbf{F}$ represent the sum of the forces acting on the spacecraft, i.e:

$$\mathbf{F} = \mathbf{F}_g + \mathbf{F}_{SRP} + \mathbf{F}_{3pb} \tag{4.35}$$

where $\mathbf{F}_g$ is the gravitational force induced by the asteroid gravity field, $\mathbf{F}_{SRP}$ is the Solar radiation pressure resulting force, and $\mathbf{F}_{3bp}$ is the third-body perturbation force due to the Sun's influence. Since the asteroid is rotating, the three resultants forces are expressed in separate frames. $\mathbf{F}_g$ is expressed in the asteroid rotating frame, while the other forces do not depend on the relative attitude of the spacecraft with respect to the asteroid, and are instead expressed in the inertial frame. We can write the acceleration of the spacecraft in the inertial frame:

$$\mathbf{a}_I = \mathbf{C}_{\mathbf{I/R}}\mathbf{a}_{g,R} + \mathbf{a}_{SRP,I} + \mathbf{a}_{3bp,I} \tag{4.36}$$

with

$$\mathbf{C}_{\mathbf{I/R}} = {\mathbf{C}_{\mathbf{R/I}}}^T \tag{4.37}$$

being the direction cosine matrix from the asteroid relative frame to the inertial frame.

### 4.5.2 Spacecraft attitude dynamics

The spacecraft attitude is also generated by the simulator at each time step. Euler's rotation equations are differential equation, which can represent the rotation of a rigid body, using a rotating reference frame with axes set to the body and parallel to the body's main inertia axes, and can be written as:

$$\mathbf{I}\dot{\boldsymbol{\omega}} + \boldsymbol{\omega} \times (\mathbf{I}\dot{\boldsymbol{\omega}}) = \mathbf{T} \tag{4.38}$$

with $\mathbf{T}$ the applied torque, $\mathbf{I}$ The moment of inertial and $\boldsymbol{\omega}$ the rotational rate of the spacecraft. In our simulator, only the SRP torque will be taken into account. This

equation allows the rotation vector of the spacecraft to be retrieved at each time phase and hence the attitude vector to be produced.

### 4.5.3 Integration

Runge-Kutta techniques are used is the real-world simulator, to propagate and derive velocity and position from the acceleration vectors, as well as generate the rotation rate vector at each time step. They are related to the basic method of Euler integration (one-step method), which is used in the estimator to predict the *a-priori* value of the velocity and position at the next time step, from the acceleration, as we will see in detail in chapter 5. An precise estimate of the next point is achieved using the information of the preceding points and their derivatives. Runge Kutta methods are the most commonly adopted methods, because they lead to reasonably reliable results with easy implementation and without unnecessary computational load. They are classified into two sub-families: variable-step sizes and fixed-step sizes.

Several $k_i$ points are picked between two time steps to evaluate the function. If this assessment is completed, the information of all intermediate points is used to calculate the next step. The first step is to estimate the first derivative of the variable to be calculated, based on the time and the variable itself as follows:

$$\frac{dy}{dt} = f(y, t) \tag{4.39}$$

The general structure of the Runge-Kutta method is as follows:

$$k_i = f(t_n + \Delta t c_i, y_n + \Delta t \sum_{i=1}^{m} a_{ij} k_i) \tag{4.40}$$

$$y_{n+1} = y_n + \Delta t \sum_{i=1}^{m} b_i k_i \tag{4.41}$$

with:

$$\sum_{i=1}^{m} a_{ij} = c_i \sum_{i=1}^{m} b_i = 1 \tag{4.42}$$

The coefficients used in the integration method, $a$, $b$ and $c$, depend on the order of the Runge-Kutta method. These values are very important to achieve a consistent numerical scheme and should conform with equation (4.42) to be zero-stable, i.e., to preserve numerical disruptions (Hahn, 1967). These coefficients can be found in the so-

called Butcher tableau (Butcher, 1987):

$$\begin{array}{c|cccc} c_1 & a_{11} & a_{12} & \dots & a_{1s} \\ c_2 & a_{21} & a_{22} & \dots & a_{2m} \\ \vdots & \vdots & \vdots & \ddots & \vdots \\ c_m & a_{m1} & a_{m2} & \dots & a_{mm} \\ \hline & b_1 & b_2 & \dots & b_m \\ & b_1^* & b_2^* & \dots & b_m^* \end{array} \tag{4.43}$$

The Butcher tableau determines whether the approach is implicit or explicit. If future stage data are used to approximate the current stage, the process is considered implicit and if not, results in a lower triangular matrix with a null diagonal. When the truncation error due to the transition from continuous to discrete time is much faster than the time step used for the $\Delta\ t$ discretization, the process is said to be consistent. The truncation error, which is the difference between the true and the truncated solution, can be determined and the accuracy defined by the following equation (Mathews and Fink, 1999):

$$\lim_{\Delta t \to 0} \frac{y_n - y(t_n)}{\Delta t} = 0 \tag{4.44}$$

with:

$$\frac{y_n - y(t_n)}{\Delta t} = y'_n + o(\Delta t^{p+1}) \tag{4.45}$$

The order of the Runge-Kutta method $p$ is defined by Equation (4.45).

If the method is consistent and zero-stable, it is a converging method, which implies that the difference between the measured value and the actual value tends to be zero. If this error is very small, the model can be very reliable.

In numerical analysis, the variable-step approach can be used to solve the EOM, to reduce errors and to ensure stability. It is especially useful because there is a large difference in the size of the derivative. If the error increases and the solution increases, the integrator decreases the time step. Generally, the truncation error, calculated using two different order methods, is used to measure the new time step, mainly:

$$\Delta t_{n+1} = n \Delta t_n \left( \frac{\epsilon_{trunc,n}}{\epsilon_{trunc,n+1}} \right)^{\frac{1}{p+1}} \tag{4.46}$$

In the simulator, a variable-step Runge-Kutta integrator is used to derive the real position and velocity vectors from the acceleration value at each time step. The simulink environment configures the appropriate method to calculate the results quicker and with sufficient precision, therefore the Runge-Kutta 45 (RK45) integrator will be used. However, in the estimator, we will use the simple Euler method to evaluate the *a-priori* value of the position and velocity at the next stage, both for simplicity and computational speed.

# 5

# Navigation

The navigation system will be examined in this chapter. It consists of sensors, the main objective of which is to collect data from the environment, and a filter to remove the noise coming from the sensors and to accurately estimate the state of the spacecraft and the interesting parameters.

## 5.1 Loosely-coupled systems

For most simulations, we have chosen to use noisy observations as a measurement model. It is a basic model that we can use, because it does not need any sensors to be modelled. This first method leads to optimal results, because the sampling time during which the measurements are delivered is not taken into account. Therefore, measurements are assumed to be given at any estimating step. However, by playing with the noise from these measurements and the number of measurements that we provide to the filter, we can have an insight into how the filter behaves. In the model, we can use various types of measurements. The first noisy data that could be used is the noisy position vector. Given in the inertial or relative reference frame, this measurement can be used for most simulations. The Gaussian noise is chosen as an additive and the measurement can be written as:

$$\tilde{\mathbf{x}} = \mathbf{x} + \boldsymbol{\nu_x} \tag{5.1}$$

The range is another measurement that can be used in the simulator. It can be seen as a distance from the surface, assuming that the spacecraft is always pointing to the asteroid, and can be calculated by:

$$\tilde{\rho} = ||\mathbf{x} - \mathbf{x_{surf}}|| + \nu_\rho \tag{5.2}$$

with $\mathbf{x_{surf}}$ the coordinates of the intersection of the surface with position vector of the spacecraft.

The range will provide the filters with additional information by simply taking the derivative:

$$\tilde{\dot{\rho}} = \frac{d\tilde{\rho}}{dt} \tag{5.3}$$

with $\dot{\rho}$ the range rate. Although these measurements do not take into account specific sensor problems such as biases, misalignments or scaling errors, it may be useful to provide an idea of the efficiency of the filter in such a"ideal" situation. However, real sensors will have more measurements and informations to give to the filters, so we cannot say that in this ideal situation, the filtre will behave better than when using real sensors.

## 5.2 Proposed sensors

Our spacecraft, which is based on the Near-Shoemaker spacecraft, can be equipped with a Star-Tracker for attitude measurements, as well as navigation cameras and a lidar for relative navigation. An accelerometer is also added to measure the SRP force.

### 5.2.1 Star-Tracker

The star-tracker is a widely used instrument during past missions. It allows the determination of the state of the spacecraft with respect to the stars present in the field-of-view of the camera. It can obtain the inertial attitude of the spacecraft, by comparing the position of the stars in the images taken, with an on-board library. The star-tracker output is given in Euler angles, mainly $\Phi, \theta, \Psi$, corresponding to the roll, pitch and yaw angles respectively.

Since we will assume perfect calibration of the star-tracker, no misalignment or scale-factors will be taken into account. Therefore, we will only assume noise, simulated as white noise with zero mean for each angle, with the associated variances $\sigma_\Phi$, $\sigma_\theta$, $\sigma_\Psi$. Usually, the axis in the direction of the line of sight suffers more from noise than the two others axis. The values of the deviations are taken from the Rosetta spacecraft, with $\sigma_\Phi = 45$ arcsec, and $\sigma_\theta = \sigma_\Psi = 5$ arcsec (Buemi et al., 1999). In this model, the roll axis is shown to be the least accurate compared to the pitch and yaw axis.

The characteristics of the star-tracker of Rosetta are listed in table 5.1. Even if these characteristics does not belongs to the Near-Shoemaker STT, they can be used as they represent possible values for every component of this sensor.

### 5.2.2 Navigation Cameras

One promising technique of navigation for past and future missions is called Landmark Tracking. This technique is achieved by the use of Navigation Cameras (NAVCAM), which scan the surface of the body looking for recognisable features. Knowing the position of these features, the navcam helps to know the relative position of the spacecraft in relation to these features. Navcams are also used in early characterisation phases to construct the shape model of the interesting body. The implementation of Landmark Tracking for Autonomous Navigation was studied by Gaskell (2005), who focused on the use of this technique for landings. The landmark tracking technique has many advantages and makes it possible to overcome problems due to the long delay in communication with the DSN used for classical navigation. Optical cameras are taking images that can be processed on-board, which includes the data edition, the centroid fitting and the noise filtering (Vasile et al., 2000), which is a significant advantage compared to other navigation

Table 5.1: Characteristics of the star-tracker of the Rosetta spacecraft (Buemi et al., 1999).

| **Characteristics** | **Value** |
|---|---|
| Field of View | $16.4 \times 16.4$ deg$^2$ |
| Dynamic range | 1.7 to 5.5 mi |
| Stars simultaneously tracked | Up to 9 |
| Accuracy: | |
| Roll axis | 45 arcsec |
| Pitch axis | 5 arcsec |
| Yaw axis | 5 arcsec |
| Update rate | 2.5 Hz |
| Output format | Quaternions |
| Mass | 8 kg |
| CCD detector | $1024 \times 1025$ pixels |
| Focal length | 46 mm |
| Diameter optical system | 29 mm |

techniques. Optical navigation using features tracking was first successfully used during the Near Mission, around Eros. Using small craters or recognisable features such as large rocks, this technique allows the position to be measured with a precision of a few metres.

The first step in acquiring Navcam measurements is the image processing part. It consists of a series of techniques to detect and analyse the image through different algorithms to find recognisable features. In this thesis, this part of the acquisition will not be implemented in the software, but the method is shown in Figure 5.1. The first step in the process of optical navigation is to obtain images of the grey surface or target area. The on-board software then autonomously pre-processes the image, and several methods are used to detect and monitor the features. The objective of Canny Edge detection is to identify edge points in the gradient direction (Shuang et al., 2013), i.e., where a maximum of the gradient magnitude exists. The noise should be suppressed by the algorithm to detect edges, but the main downside of noise suppression is the loss of useful edge knowledge. Therefore, a trade-off between the noise and the accuracy of the information about the edges needs to be made. The pseudo-edge elimination process is very important for the rest of navigation. It enables real edges to be separated from, for instance, the edges created by the shadow of the Sun. The algorithm will retrieve the pseudo-edges and remove them from the model, taking into account the camera angle with respect to the Sun and the Sun's location in the area. After these steps, to project the outline of the body or the features on the picture plane, the fitting of the limb profile is achieved. At the end, to maintain trace of the features, the centroid of the landmarks or the body should be identified. The centroid-fitting phase uses the fitting of the body-shape and the techniques of edge detection to create the planet or body equation.

The simplest optical navigation measurement model is the pinhole camera model. This model assumes that a single ray is emitted by every point in the target area. Thus, each ray is mapped to a point on the focal plane (Shuang et al., 2013). The following model describes the relationship between the landmark coordinates $(x_{LM}, y_{LM}, z_{LM})$ and

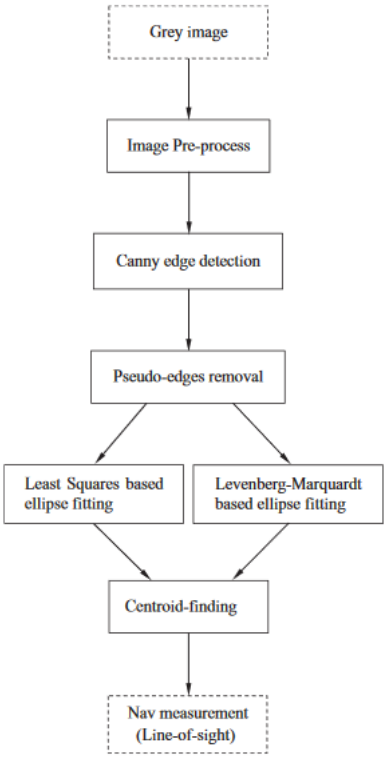


Figure 5.1: Image processing procedure(Shuang et al., 2013).

the associated pixel $(u, v)$:

$$\begin{aligned} u &= \frac{x_{LM,c}}{z_{LM,c}} f \\ v &= \frac{y_{LM,c}}{z_{LM,c}} f \end{aligned} \tag{5.4}$$

with $u$, $v$ the coordinates of the point in the focal plane, $f$ the focal length of the camera and $(x_{LM,c}, y_{LM,c}, z_{LM,c})$ are the coordinates in the camera-fixed frame. $z_{LM,b}$ corresponds to the distance between the point $(x_{LM}, y_{LM}, z_{LM})$ and the pinhole. Taking into account the fact that the projective plane has a finite number of pixels, and that a pixel has a size p, the real pixels coordinates are:

$$\begin{aligned} u &= \frac{x_{LM,c}}{z_{LM,c}} \frac{f}{p} \\ v &= \frac{y_{LM,c}}{z_{LM,c}} \frac{f}{p} \end{aligned} \tag{5.5}$$

Since we will not simulate the image processing part, we must add certain measuring errors in the pixels, i.e.:

$$\begin{aligned} \tilde{u} &= u + \delta u \\ \tilde{v} &= v + \delta v \end{aligned} \tag{5.6}$$

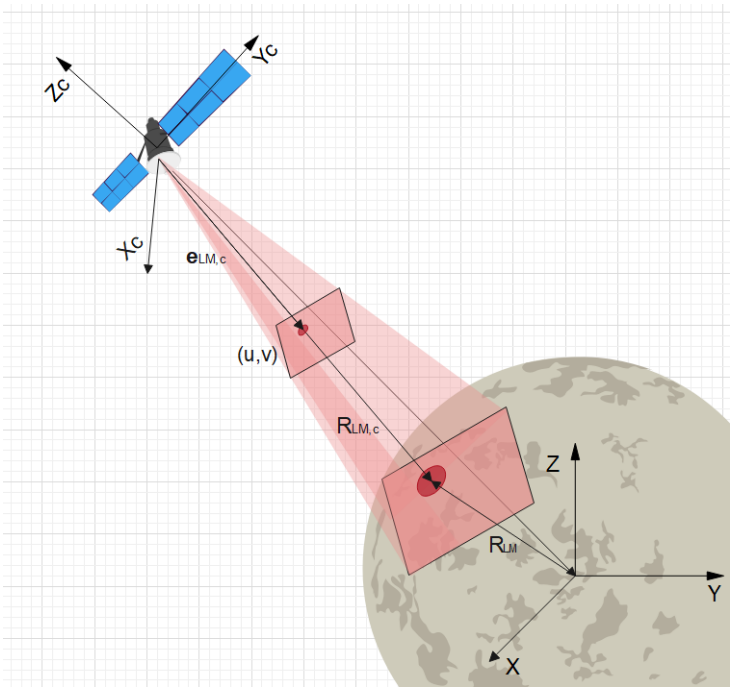


Figure 5.2: Navcam geometry

whit $\delta u$, $\delta v$ are white noises with zero-mean. The line-of-sight vector $e_{i,C}$ corresponds to the line between the $i^{th}$ image point, and the camera-exposure centre, as shown in Figure 5.2. In the camera-fixed frame, the line-of-sight vector is:

$$\mathbf{e}_{i,b} = \frac{1}{\sqrt{\tilde{u}_i^2 + \tilde{v}_i^2 + f}} \begin{pmatrix} \tilde{u}_i \\ \tilde{v}_i \\ f \end{pmatrix} \tag{5.7}$$

where $v_i$ and $u_i$ are the coordinates of the point where the $i^{th}$ point ray is projected on the image plane. A transformation is necessary to change the line-of-sight vector form the camera-fixed frame to the inertial frame:

$$\mathbf{e}_{i,I} = \mathbf{C_{I/B}} \mathbf{e}_{i,B} \tag{5.8}$$

with $\mathbf{C_{B/I}}$ the transformation matrix from body frame to inertial frame, since we assume that the camera is following the attitude of the spacecraft. Navigation camera properties are introducing some measurement noise, which can be modelled as follows:

$$\tilde{\mathbf{b}}_{i,I} = \mathbf{m}_i(\mathbf{x}) + \boldsymbol{\sigma}_i \tag{5.9}$$

with $\tilde{\mathbf{b}}_{i,I}$ the line-of-sight measurement from the $i^{th}$ landmark, $\mathbf{x}$ denotes the state of the spacecraft and $\boldsymbol{\nu}$ is the navigation-camera noise, modelled as white Gaussian noise

with zero mean. Thus, if $\mathbf{R}_i$ is the noise covariance matrix representing the measurements errors, we obtain (Shuang et al., 2013):

$$\begin{aligned} E[\boldsymbol{\sigma}_i] &= 0 \\ E[\boldsymbol{\sigma}_i \boldsymbol{\sigma}_i^T] &= \mathbf{R}_i \delta_{ij} \end{aligned} \tag{5.10}$$

Image processing is a highly complex task, involving several different algorithms to manipulate NavCam image data. Due to the complexity of this method, image processing will therefore not be part of this thesis, and the Navcams will show the landmarks' noisy pixel locations.

### 5.2.3 Lidar

The lidar (light detection and ranging) is a powerful navigation sensor based on the analysis of the properties of a beam of light returned to its emitter. Unlike radar that uses radio waves or sonar, which uses acoustic waves, lidar uses light (from visible, infrared or ultraviolet spectrum), most of the time a laser. In general, the concept of telemetry (determining the distance of an object) involving a significant proportion of lidar applications involves the use of a pulsed laser. The distance is given by calculating the interval between a pulse's emission and a reflected pulse's detection, recognising the speed of light. Another class of speed modulation based applications uses a fine emission spectrum (a fixed frequency) laser. It is the Doppler-Fizeau effect, which is the change in the reflected and received wave frequency, which makes it possible to calculate the object's speed. Many other parameters (gas concentrations and individual particles, density, temperature, etc.) can affect the measurements in the atmosphere and other diffusive media. The lidar is less wavelengthy, allowing for much smoother modulation and greater time and spatial resolution for a reduced instrument size relative to radar technologies. Lidar lasers, however, can not penetrate very diffusive media like thick clouds or soil surfaces and require a extremely accurate calibration.

The Lidar sends the ideal laser beam to the target and uses the reflected light to research the target characteristics by studying the received signal and comparing it to the transmitted signal. It calculates the distance to the target by measuring the time-of-flight of the obtained pulse and can be used to determine the range rate by measuring the range at the next time stage. Lidars can be used to highlight some of the surface properties by examining the received signal, such as the surface slope and the roughness of the surface.

In our software model, we will only use lidar to measure the range and range-rate of the spacecraft with respect to Eros, since we assume that the surface mapping of the asteroid was done earlier in the mission. However, we must take into account the fact that the relative distance from the surface of the asteroid to a random point can not provide direct information on the actual location of the spacecraft. This distance is only useful if we already know the location of this surface point in the asteroid frame. This condition will be valid if we use the already projected landmarks for which we already know the location. This model assumes that we can point the laser to the nearest landmark, which is not true for every lidar model. However, we will assume that the laser is pointing in the desired direction by the use of a mirror system, and that the lidar will work in

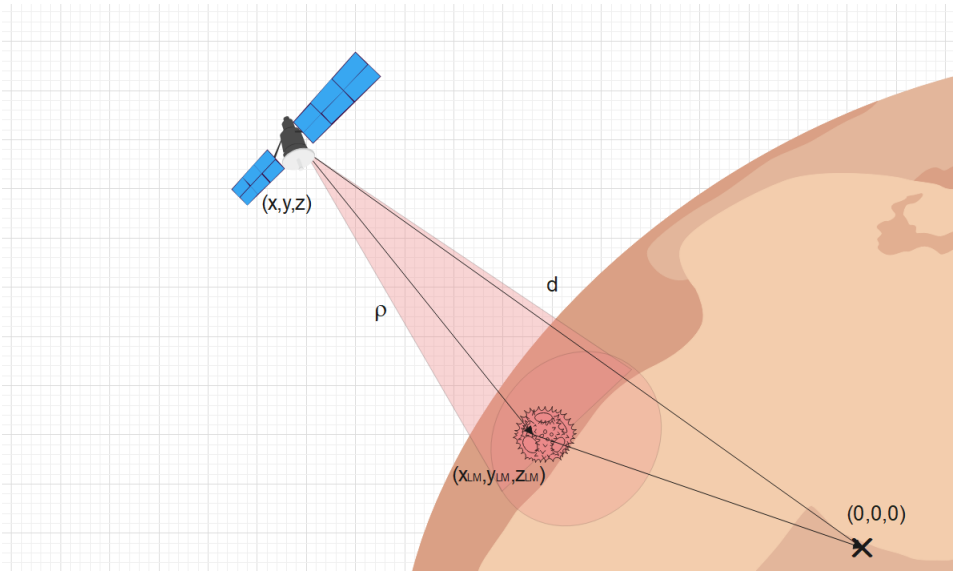


Figure 5.3: Lidar geometry

combination with the Navcam to output measurements. The range of the spacecraft can be calculated as follows:

$$\rho = \sqrt{(x - x_{LM})^2 + (y - y_{LM})^2 + (z - z_{LM})^2} \tag{5.11}$$

where $(x_{LM}, y_{LM}, z_{LM})$ are the coordinates of the landmark, and $(x, y, z)$ the coordinates of the lidar in the asteroid frame, as shown in Figure 5.3. Moreover,

$$\rho = c\frac{t}{2} \tag{5.12}$$

where $t$ is the time-of-flight (TOF), i.e., the time between the sent and received light pulse, and c is the speed of light. We can compute the range resolution:

$$\Delta\rho = c\frac{\Delta t}{2} \tag{5.13}$$

with $\Delta t$ the resolution of time measurements. When the Navcam can provide information on the landmarks in its FOV, the lidar will point in the direction of the landmarks to determine the range using the TOF, and the data at the previous time step will also be used to determine the range-rate of the spacecraft. Although lidar may suffer from pointing and bias errors, measurement errors are usually due to the instrument itself and the asteroid environment and surface topography. Measurement errors can be modelled as follows:

$$\begin{aligned} \tilde{t} &= t + \sigma_t + \sigma_r \\ \tilde{\rho} &= c\frac{\tilde{t}}{2} \\ \sigma_l &= \sigma_t + \sigma_r \\ E[\sigma_l] &= 0 \\ E[\sigma_l \sigma_l] &= R_t \end{aligned} \tag{5.14}$$

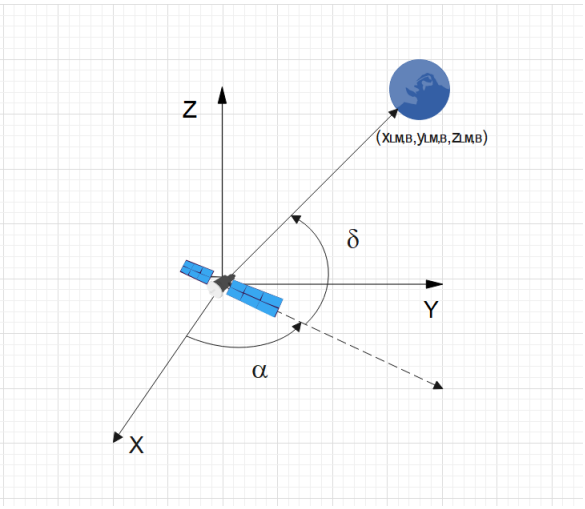


Figure 5.4: Lidar control angles

with $\nu_t$ white-Gaussian noise in the range of nano-seconds, which represents the error in time due to the environment, and with $\nu_r$, the resolution error. $R_l$ is the noise covariance representing the measurements errors. In tandem with the navcam, observations can be reconstructed using the $\alpha$ and $\beta$ lidar commanded angles, which can be calculated by the following formula:

$$\begin{aligned} \alpha &= \arctan \frac{y_{LM,b}}{x_{LM,b}} \\ \delta &= \arctan \frac{z_{LM,b}}{\sqrt{x_{LM,b}^2 + y_{LM,b}^2}} \end{aligned} \tag{5.15}$$

where $(x_{LM,b}, y_{LM,b}, z_{LM,b})$ are the Landmarks coordinates in the spacecraft reference frame. $\alpha$ and $\delta$ are called azimuth and elevation angles respectively, are shown in Figure 5.4, and are obtained from the camera image, with the following pointing errors:

$$\begin{aligned} \tilde{\alpha} &= \alpha + \Delta\alpha \\ \tilde{\delta} &= \delta + \Delta\delta \end{aligned} \tag{5.16}$$

The measurement vector for the lidar sensor, from the $i_{th}$ landmark is given by:

$$\tilde{\mathbf{h}}_\mathbf{i} = \begin{pmatrix} \rho_i \\ \dot{\rho}_i \\ \alpha_i \\ \delta_i \end{pmatrix} + \boldsymbol{\sigma_{l,i}} \tag{5.17}$$

Hence, this sensor gives information on the location of the spacecraft, but also direct information on the relative velocity of the spacecraft, with a good accuracy.

## 5.3 Estimators

Kalman filtering is a well-known algorithm for estimating unknown variables and parameters based on real-time measurements. It can be used for estimating the state vector, as well as for estimating external parameters. In the simplest case, where we would have to deal with a linear system that we would like to know the evolution over time, we might have used the Kalman Linear filter. However, there are only a few linear systems in the real world. The linear Kalman filter can therefore no longer be applied. Extended Kalman and Unscented Kalman filter have been developed to deal with such problems. Since they are well documented, we know that they can produce very accurate results in complex situations, without being too difficult to implement. They will therefore be used in our estimation process. The Extended and Unscented Kalman filters will be presented in this section.

### 5.3.1 Extended Kalman Filter

The Extended Kalman Filter (EKF) is an extension of the Linear Kalman Filter (LKF). The Linear Kalman Filter is an effective tool to estimate the state of the system in a noisy environment. However, it can only be applied to linear cases, which is not very useful in real cases, that are mostly non-linear. As shown by Welch and Bishop (2006), Tapley et al. (2004) and Mooij (2019), a discrete non linear system is expressed by:

$$\mathbf{x}_{k+1} = \mathbf{f}(\mathbf{x}_k, \mathbf{u}_k, \mathbf{w}_k) \tag{5.18}$$

We can express the sensors measurements as:

$$\mathbf{z}_k = \mathbf{h}(\mathbf{x}_k, \mathbf{v}_k) \tag{5.19}$$

where $\mathbf{u}$ is the input vector, $\mathbf{z}$ is the measurement vector, $\mathbf{x}$ is the state of the spacecraft and $\mathbf{v}$ and $\mathbf{w}$ are noise contributions. We denote by $k$ the current time step, and $k-1$ the previous time step. The first goal of the filter is to build an *a-priori* estimate of the spacecraft:

$$\hat{\mathbf{x}}_k^- = \mathbf{f}(\hat{\mathbf{x}}_k^-, \mathbf{u}_{k+1}, \mathbf{0}) \tag{5.20}$$

The current *a-priori* state estimation is done using the previous *a-posteriori* state of the spacecraft. Moreover, we can compute an estimate of the measurements:

$$\hat{\mathbf{z}}_k = \mathbf{h}(\hat{\mathbf{x}}_k^-, 0) \tag{5.21}$$

By linearization of the previous equations, we can approximate the state and the measurements, as shown by Welch and Bishop (2006) and Mooij (2019):

$$\mathbf{x}_{k+1} \approx \hat{\mathbf{x}}_{k+1}^- + \mathbf{A}_k(\mathbf{x}_k - \hat{\mathbf{x}}_k) + \mathbf{W}_k\mathbf{w}_k \tag{5.22}$$

$$\mathbf{z}_k \approx \hat{\mathbf{z}}_k^- + \mathbf{H}_k(\mathbf{x}_k - \hat{\mathbf{x}}_k) + \mathbf{V}_k\mathbf{v}_k \tag{5.23}$$

In these equations, the state and measurement vectors are expressed as a function of the current state, and *a-priori* estimations of the next time state.

The noise parameters can be expressed as Gaussian noise with 0 mean:

$$p(\mathbf{v}_k) \sim N(0, \mathbf{R}_k) \tag{5.24}$$

$$p(\mathbf{w}_k) \sim N(0, \mathbf{Q}_k) \tag{5.25}$$

Matrices $\mathbf{R}_k$ and $\mathbf{Q}_k$ are the measurement-noise and process-noise matrices, respectively. Matrices $\mathbf{A}_k$, $\mathbf{W}_k$, $\mathbf{H}_k$, $\mathbf{V}_k$ are called Jacobians, and are defined as follows:

$$\begin{aligned}
\mathbf{A}_k &= \left.\frac{\partial \mathbf{f}}{\partial \mathbf{x}}\right|_{(\hat{\mathbf{x}}_k, \hat{\mathbf{u}}_{k+1}, \mathbf{0})} \\
\mathbf{H}_k &= \left.\frac{\partial \mathbf{h}}{\partial \mathbf{x}}\right|_{(\hat{\mathbf{x}}_k^-, \mathbf{0})} \\
\mathbf{V}_k &= \left.\frac{\partial \mathbf{h}}{\partial \mathbf{v}}\right|_{(\hat{\mathbf{x}}_k^-, \mathbf{0})} \\
\mathbf{W}_k &= \left.\frac{\partial \mathbf{f}}{\partial \mathbf{w}}\right|_{(\hat{\mathbf{x}}_k, \hat{\mathbf{u}}_{k+1}, \mathbf{0})}
\end{aligned} \tag{5.26}$$

Since we have introduced approximations for the state of the spacecraft, an error with respect to the real state can be calculated:

$$\begin{aligned}
\hat{\mathbf{e}}_{xk}^- &\equiv \mathbf{x}_k - \hat{\mathbf{x}}_k \approx \mathbf{A}_{k-1}(\mathbf{x}_{k-1} - \hat{\mathbf{x}}_{k-1}) + \boldsymbol{\varepsilon}_k \\
\hat{\mathbf{e}}_{zk}^- &\equiv \mathbf{z}_k - \hat{\mathbf{z}}_k \approx \mathbf{H}_k(\hat{\mathbf{e}}_{xk}^-) + \boldsymbol{\eta}_k
\end{aligned} \tag{5.27}$$

With $\boldsymbol{\varepsilon}$ and $\boldsymbol{\eta}$ linear approximations of the noise, with the following distributions:

$$p(\boldsymbol{\varepsilon}_k) \sim N(\mathbf{0}, \mathbf{W}_{k-1}\mathbf{Q}_{k-1}\mathbf{W}_{k-1}^T) \tag{5.28}$$

$$p(\boldsymbol{\eta}_k) \sim N(\mathbf{0}, \mathbf{V}_k\mathbf{R}_k\mathbf{V}_k^T) \tag{5.29}$$

We can define the prediction error, as the difference between the *a-posteriori* and the *a-priori* errors, which should be equal to a scaled measurement residual:

$$\hat{\mathbf{e}}_k^- \equiv \mathbf{x}_k - \hat{\mathbf{x}}_k^- = \mathbf{K}(\hat{\mathbf{e}}_{zk}^-) \tag{5.30}$$

This equation is the key to find the *a-posteriori* state estimation:

$$\hat{\mathbf{x}}_k = \hat{\mathbf{x}}_k^- + \mathbf{K}(\mathbf{z}_k - \hat{\mathbf{z}}_k^-) \tag{5.31}$$

Thus, the covariance matrix can be written as (Mooij, 2019):

$$\mathbf{P}_{k+1}^- = \mathbf{A}_k\mathbf{P}_k\mathbf{A}_k^T + \mathbf{W}_k\mathbf{Q}_k\mathbf{W}_k^T \tag{5.32}$$

And the gain $\mathbf{K}$ can be written as:

$$\mathbf{K}_k = \mathbf{P}_k^-\mathbf{H}_k^T(\mathbf{H}_k\mathbf{P}_k^-\mathbf{H}_k^T + \mathbf{V}_k\mathbf{R}_k\mathbf{V}_k^T)^{-1} \tag{5.33}$$

With :

$$\mathbf{P}_k = (\mathbf{I} - \mathbf{H}_k\mathbf{K}_k)\mathbf{P}_k^- \tag{5.34}$$

The EKF filter is widely used in state estimation. It results in fast convergence compared to other methods, and leads to highly accurate results when the system is almost linear. When the system is highly non-linear, other methods might be preferred, such as the Unscented Kalman filter for better performance.

### 5.3.2 Unscented Kalman Filter

The Unscented Kalman Filter (UKF) is an improvement of the EKF, as written by Wan and Van Der Merwe (2000). The EKF can cover significant uncertainties by using a first order linearization of the equations of motion. The UKF uses a deterministic sampling approach to provide more precise results, describing the state with a collection of sigma points. This set is fed to a non-linear EOM, which allows the filter to estimate the uncertainties up to the third order.

At each time step, the filter is fed with the sigma points, which have been carrefully selected to contain maximum statistical characteristics of the state variables. The so-called Unscented transformation will calculate those statistical characteristics. If we consider a random variable $\mathbf{x}$ in our non-linear function $\mathbf{y} = g(\mathbf{x})$, a matrix of sigma vectors $\chi_i$ should be built to estimate the statistical characteristics of the output, defined as follows:

$$\begin{aligned}
\chi_{0,k} &= \bar{\mathbf{x}}_k \\
\chi_{i,k} &= \bar{\mathbf{x}}_k + \sqrt{(L+\lambda)(\mathbf{P}_{\mathbf{x},k} + \mathbf{Q}_{k+1})}\Big|_i \qquad \text{for} \quad i = 1, .., L \\
\chi_{i,k} &= \bar{\mathbf{x}}_k - \sqrt{(L+\lambda)(\mathbf{P}_{\mathbf{x},k} + \mathbf{Q}_{k+1})}\Big|_{i-L} \qquad \text{for} \quad i = L+1, .., 2L
\end{aligned} \tag{5.35}$$

We can define the associated weights to the corresponding sigma:

$$\begin{aligned}
W_0^{(m)} &= \frac{\lambda}{L+\lambda} \\
W_0^{(c)} &= \frac{\lambda}{L+\lambda} + (1 - \alpha^2 + \beta) \\
W_i^{(m)} &= W_i^{(c)} = \frac{1}{2(L+\lambda)} \qquad \text{for} \quad i = 1, .., 2L
\end{aligned} \tag{5.36}$$

with $\mathbf{P}_\mathbf{x}$ the covariance matrix, $\bar{\mathbf{x}}$ the mean value of the random variable, $L$ the dimension of $\mathbf{x}$ and thus $2L + 1$ is the dimension of the sigma matrix. $\lambda = \alpha^2(L + \kappa) - L$ is a scaling parameter, $\alpha$ determines the spread of the sigma points around $\bar{\mathbf{x}}$, $\kappa$ is another scaling parameter, most of the time equal to zero, and $\beta$ gives information about the $\mathbf{x}$ distribution.

Similarly to the EKF, the UKF is updating the state at every time step, but now adding the sigma point computed through the previous equations. The sigma matrix can be computed by the following non-linear equation:

$$\boldsymbol{\chi}_{k+1|k} = f(\boldsymbol{\chi}_k, \mathbf{u}_k, \mathbf{v}_k) \tag{5.37}$$

This equation can be used to find the current estimated *a-priori* state vector and covariance matrix, as shown by Julier and Uhlmann (2004):

$$\begin{aligned}\hat{\mathbf{x}}_{k+1}^{-} &= \sum_{i=1}^{2L+1} W_i^{(m)} \boldsymbol{\chi}_{i,k+1|k} \\ \mathbf{P}_{\mathbf{x},k+1}^{-} &= \sum_{i=1}^{2L+1} W_i^{(m)} (\boldsymbol{\chi}_{k+1|k} - \hat{\mathbf{x}}_{k+1}^{-})(\boldsymbol{\chi}_{k+1|k} - \hat{\mathbf{x}}_{k+1}^{-})^T\end{aligned} \tag{5.38}$$

Applying the unscented transform to the measurement equations results in finding the *a-priori* measurements and covariance matrix associated through the following equations:

$$\begin{aligned}\boldsymbol{\zeta}_{k+1|k} &= f(\boldsymbol{\chi}_{k+1|k}, \mathbf{w}_k) \\ \hat{\mathbf{z}}_{k+1}^{-} &= \sum_{i=1}^{2L+1} W_i^{(m)} \boldsymbol{\zeta}_{i,k+1|k} \\ \mathbf{P}_{\bar{\mathbf{z}},k+1} &= \sum_{i=1}^{2L+1} W_i^{(m)} (\boldsymbol{\zeta}_{k+1|k} - \hat{\mathbf{z}}_{k+1}^{-})(\boldsymbol{\zeta}_{k+1|k} - \hat{\mathbf{z}}_{k+1}^{-})^T\end{aligned} \tag{5.39}$$

If we consider $M$ measurements, $\zeta_{k+1|k}$ corresponds to a set of $M \times 2L + 1$ sigma measurements points. Similarly to the EKF, the a-posteri state can be written as:

$$\hat{\mathbf{x}}_k = \hat{\mathbf{x}}_k^{-} + \mathbf{K}(\mathbf{z}_k - \hat{\mathbf{z}}_k^{-}) \tag{5.40}$$

The equation for the covariance propagation is the following:

$$\mathbf{P}_{\mathbf{x},k}^{-} = \mathbf{P}_{\mathbf{x},k} + \mathbf{K}_k \mathbf{P}_{\mathbf{z},k}^{-} \mathbf{K}_k^T \tag{5.41}$$

with the Kalman gain:

$$\mathbf{K}_k = \mathbf{P}_{\mathbf{xz},k} \mathbf{P}_{\bar{z},k}^{-1} \tag{5.42}$$

and the cross-covariance matrix can be found by:

$$\mathbf{P}_{\mathbf{xz},k+1} = W_i^{(m)} (\boldsymbol{\chi}_{k+1|k} - \hat{\mathbf{x}}_{k+1}^{-})(\zeta_{k+1|k} - \hat{\mathbf{z}}_{k+1}^{-})^T \tag{5.43}$$

The Unscented Kalman Filter can be used under non-linear conditions, where the EKF efficiency is not enough. It requires more computational time but leads to significant improvements in results, especially when the system is highly non-linear.

### 5.3.3 Kalman filters tuning

To be used efficiently, the Kalman filters covariance and measurement matrices must be optimised. One very popular way to tune the Kalman filter is through trial and error.

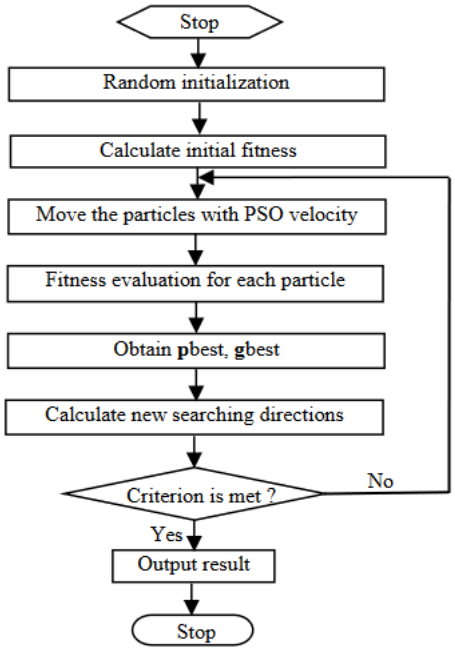


Figure 5.5: PSO pseudo-code

But this technique is time-consuming and not optimal. Other approaches such as Genetic Algorithms (Rapp, 2004) and Particle Swarm Optimisation algorithms (Jatoth and Kumar, 2009) can be implemented. Gene theory is used in the Genetic Algorithm in which the genetic code is encoded by each individual in society. Particle Swarm optimisation is a population-based stochastic search algorithm that is inspired by the social behaviour of bird flocking and fish schooling. PSO was preferred over GA for the simplicity of implementation to tune the Kalman filters.

Starting with an arbitrarily initialised swarm population, each PSO individual flies through the N-dimensional solution space and recalls the best position they encountered. Each particle in the swarm is described by its position and velocity. The position and velocity of the particles at each iteration are updated according to the following equations:

$$\mathbf{v}_i(k+1) = w\mathbf{v}_i(k) + c_1\text{rand}()(\mathbf{p}_{best}(k) - \mathbf{x}_i(k)) + c_2\text{rand}()(\mathbf{g}_{best}(k) - \mathbf{x}_i(k)) \tag{5.44}$$

$$\mathbf{x}_i(k+1) = \mathbf{v}_i(k+1) + \mathbf{x}_i(k) \tag{5.45}$$

With $w$, $c_1$, $c_2$ weights corresponding to the inertia weight, and cognitive and social accelerations respectively.The pseudo-code of the PSO is shown in Figure 5.5.

Some PSO parameters can be chosen freely, such as acceleration coefficients, $c_1$ and $c_2$, together with random vectors, which control the stochastic influence of cognitive and social components on the total velocity of the particle. The PSO parameters are summarized in Figure 5.2.

Table 5.3: PSO results

| | **Trial and error result** | **PSO result** |
|---|---|---|
| $\mathbf{q_1}$ | 1e-09 | 1.03e-14 |
| $\mathbf{q_2}$ | 1e-11 | 2.64e-12 |
| $\mathbf{q_3}$ | 1e-16 | 2.21e-18 |

| **Parameters** | **Value** |
|---|---|
| $c_1$ | 2.5 |
| $c_2$ | 2.5 |
| w | 0.4-0.9 |

Table 5.2: Tuning parameters of the PSO

To reduce the computational time in the PSO optimisation, the covariance matrix must be decomposed into two sub-matrices, according to the following equation:

$$\mathbf{Q} = \begin{pmatrix} q_1 & q_2 & q_3 \end{pmatrix} \begin{bmatrix} 1 & 0 & 0 \\ 0 & 1 & 0 \\ 0 & 0 & 1 \end{bmatrix} \tag{5.46}$$

where $q_1$, $q_2$ and $q_3$ are the free parameters to tune. The values of the covariance matrix $Q$ must also be constricted between minimum and maximum values to be optimised by the PSO. The values of $Q$ are constricted between $[10^{-20}, 10^{-2}]$ for this optimiser. The fitness function that must be minimised by the PSO is the mean-square error, which can be calculated according to the following equation:

$$MSE = \frac{1}{N} \sum_{1}^{N} (y_k - \hat{y}_k) \tag{5.47}$$

The results of the PSO optimisation are displayed in Table 5.3.

# 6

# Simulator design

The design of an autonomous navigation software is presented in this chapter. The main purpose of this navigation software is to be able to predict at each stage the state of the spacecraft, the rotational rate of the asteroid and the spherical harmonic coefficients, to make navigation around the asteroid more autonomous.

## 6.1 State and parameters vector

The simulator outputs the spacecraft's state and attitude vectors, as well as the asteroid's attitude. Navigation software will use data from the sensors to determine the location and velocity of the spacecraft, as well as the spherical harmonic coefficients and the rotational speed and attitude of the spacecraft, which would be needed to estimate the same parameters in the next time step. The state and parameter vector that will be output from the navigation software is as follows:

$$\mathbf{X} = \begin{pmatrix} \mathbf{x}_I \\ \mathbf{v}_I \\ \boldsymbol{\omega}_{R/I} \\ \mathbf{C}_{ij} \\ \mathbf{S}_{ij} \\ \mathbf{q}_{R/I} \end{pmatrix} \tag{6.1}$$

where $\mathbf{x}_I$, $\mathbf{v}_I$ are the position and velocity vectors of the spacecraft in the inertial frame, $\mathbf{C}_{ij}$ and $\mathbf{S}_{ij}$ are the spherical harmonics coefficients of degree i and order j, and $\omega_{R/I}$ and $\omega_{R/I}$ are the rotation rate and attitude vectors of the asteroid with respect to the inertial frame. These states and parameters are the only vectors required to compute the state of the spacecraft at the next time step, using the spherical harmonics model to estimate the gravity field of the asteroid.

## 6.2 Top-level simulator architecture

The simulator is divided into four main blocks, each of which focuses on a specific task. The complete architecture is shown in Figure 6.1 and consists of:

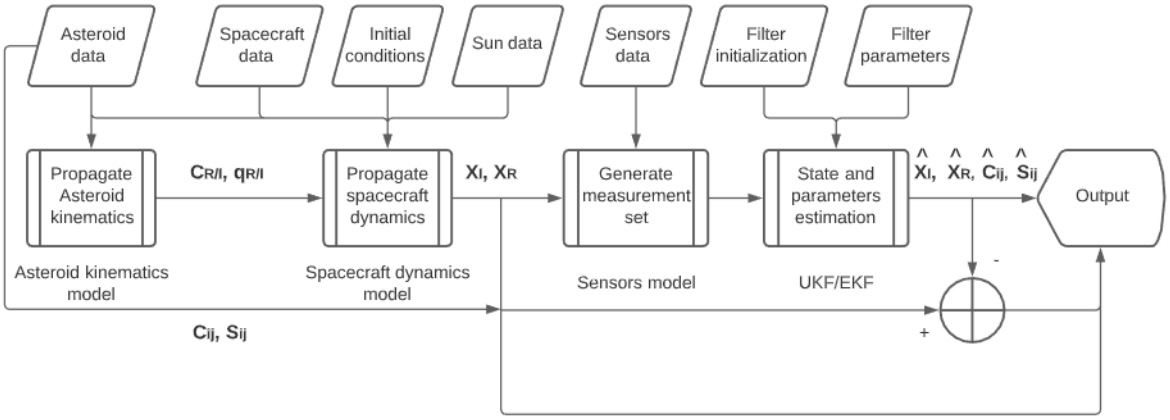


Figure 6.1: Simulator architecture

**Asteroid kinematics model** : This block uses asteroid data to simulate the rotation of the asteroid. The outputs of this block are the relative attitude of the asteroid with respect to the inertial frame, and the direction cosine matrix for frame transformation between the relative and inertial references frame.

**Spacecraft dynamics model** : Using the gravity model, the Sun data and the output of the first block, this block propagates the dynamics of the spacecraft starting with given initial conditions.

**Sensors model** : Depending on the choice of sensors and their models, this blocks output noisy measurements based on the real state and attitude vectors of the spacecraft.

**Navigation filters** : This block outputs the estimated states and parameters based on *a-priori* values, measurements and given analytical models. The filters must be initialised with parameters and optimum covariance matrices, pre-processed by the PSO.This block refers to the autonomous and on-board algorithm that the spacecraft would be carrying.

## 6.3 Asteroid gravity modelling

For this study, we will assume that the main gravitational influence of the spacecraft is due to the gravitational field of the asteroid. The asteroid orbit around the Sun will be neglected, and it is assumed that no other bodies are disturbing the dynamics of the environment except the asteroid, the spacecraft and the Sun.

Figure 6.2: Eros polyhedron shape model

### Polyhedron Shape model

A polyhedron model of Eros was implemented using shape data obtained during the Near-Shoemaker mission, with 49150 facets of resolution, as shown in Figure 6.2. Using the polyhedron model of the gravity field, the gravitational potential and acceleration acting on a spacecraft due to the polyhedron shape model, can be computed. The polyhedron gravity field algorithm is shown in Figure 6.3. The gravitation acceleration due to the asteroid was calculated with this polyhedron gravity model on a sphere of 25 km and a radius of 250 km, as shown in Figure 6.4. On the two figures, as expected, we can see the two elongated poles of Eros, represented by the regions where the acceleration is much stronger. For the 250 km sphere, we can also note that the differences in gravitational accelerations are smaller, leading to a more uniform gravity map. That can be explained by the fact that the disturbances due to the irregular shape are also decreasing with the distance, since the acceleration decreases with the distance to the centre.

### Spherical harmonics gravity field

In the Simulator, the spherical harmonics model of the gravity field of Eros was implemented using the data obtained during the near-mission and up to degree and order 22. As we will show, this resolution is sufficient to characterise the gravity field with sufficient precision and has the benefit of reducing the computational loads that can be obtained using the polyhedron gravity model. The algorithm used to construct the spherical harmonics gravity field is shown in figure 6.5.

The gravity field of Eros with the spherical harmonics model based on the shape model spherical harmonics coefficients is shown in Figure 6.6 on a 25 km sphere. The graphs are showing the two poles of Eros, where the acceleration is maximum.

### Conclusion

Spherical harmonics up to degree 22 and polyhedron gravity models with 3897 vertices and 7790 faces have been simulated for 433 Eros to compare results. While the polyhedron model is very accurate, it is computationally expansive compared to the spherical harmonic model. Reducing the number of faces and resolution, the computational time reduces with the accuracy of the model. It does however, contribute to a similar gravity

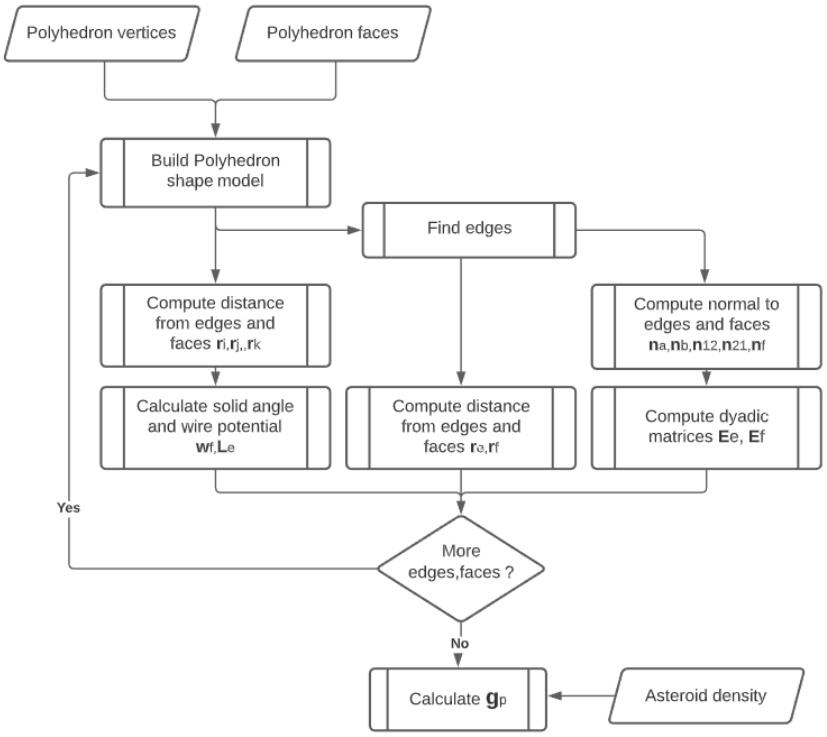


Figure 6.3: Polyhedron gravity algorithm

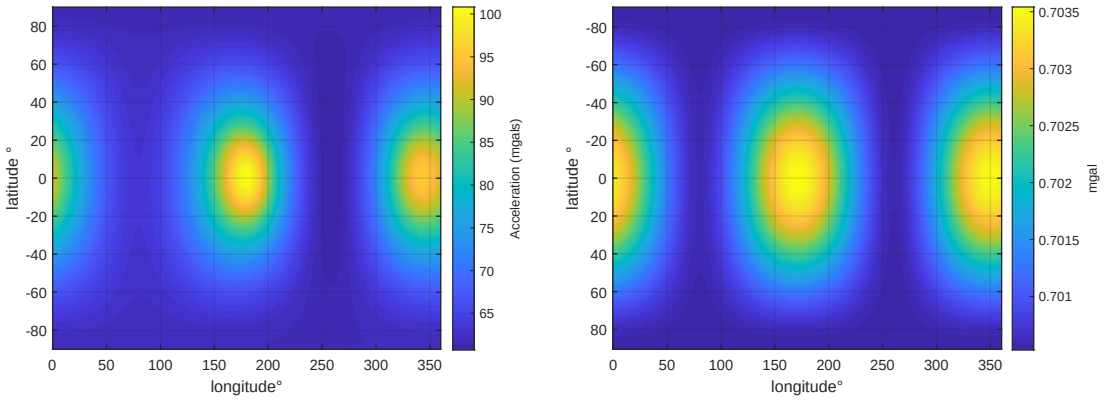


(a) 25 km sphere radius

(b) 250 km sphere radius

Figure 6.4: Gravity acceleration acting on a sphere of 25 km and 250 km radius.

field model where the shape of Eros can be identified. Errors increase by decreasing the distance to the centre of the asteroid and the maximum residuals between the two models in a 35 km sphere are shown in Figure 6.7 for the chosen resolutions. We can see in the Figure that these errors are small, especially considering such low altitude orbits. However, they are dependant on the resolutions chosen both for the polyhedron and spherical harmonics models. We have selected the resolution of the polyhedron model and the resolution of the spherical harmonics according to our CPU limitations. Reducing the

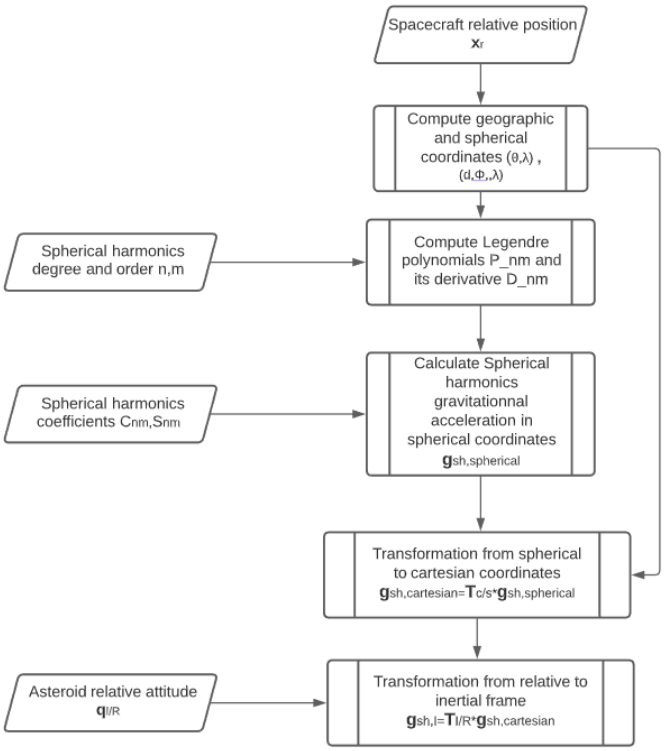


Figure 6.5: Spherical harmonics gravity algorithm

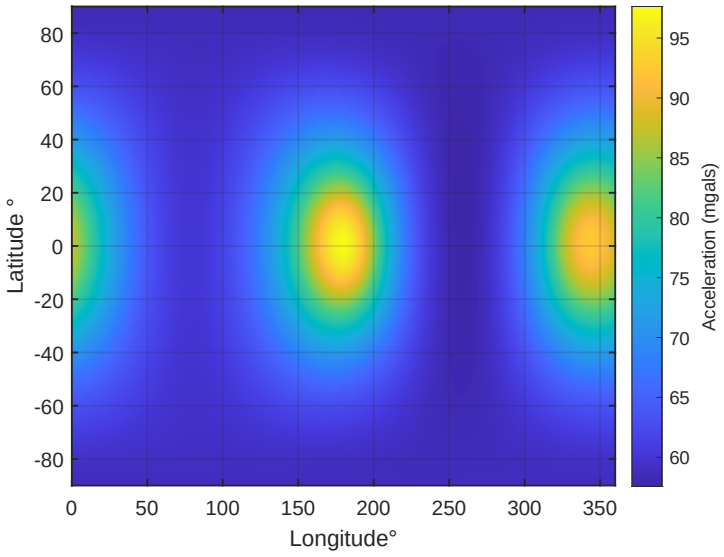


Figure 6.6: Spherical harmonics gravity acceleration felt on a 25 km sphere.

degree and order of spherical harmonic expansion, the residuals would be greater. However by reducing the resolution of the polyhedron, the residuals decrease until we reach almost the same resolution of the spherical harmonics because we have chosen a higher resolution for the polyhedron model, and then start to increase again. In the navigation

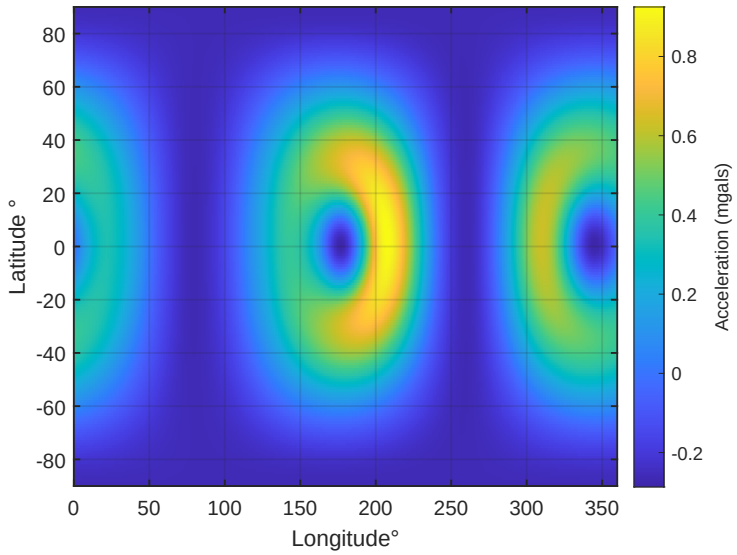


Figure 6.7: Spherical harmonics/Polyhedron gravity residuals on a 35 km sphere.

process, it is easier to use the spherical harmonics model to be computationally effective, but this model cannot be used for the last mission or landing phases due to the fact that the spherical harmonics are only true outside the reference sphere and can lead to divergences close to the surface. A polyhedron model or other gravity model should be chosen for the last mission phase.

## 6.4 Sensors models

Among the sensors, Navcam and Lidar require more complex modelling. In this section, their algorithm will be detailed.

### 6.4.1 Navcam

The navcam algorithm used in the simulator model, resumed in Figure 6.8, can be divided into three parts:

- Creation of the environment: create a polyhedron model and produce Landmarks on the surface.
- Detection of the landmarks: are the landmarks in the field of view of the camera, and are the lightning conditions adequate to be able to see the landmarks?
- Generation of measurements: map the Landmark coordinates on the pixel plane to produce the corresponding measurement vector.

To create landmarks at certain locations on the shape model, the landmark generation technique must be used. Landmarks are recognisable surface features, such as craters or

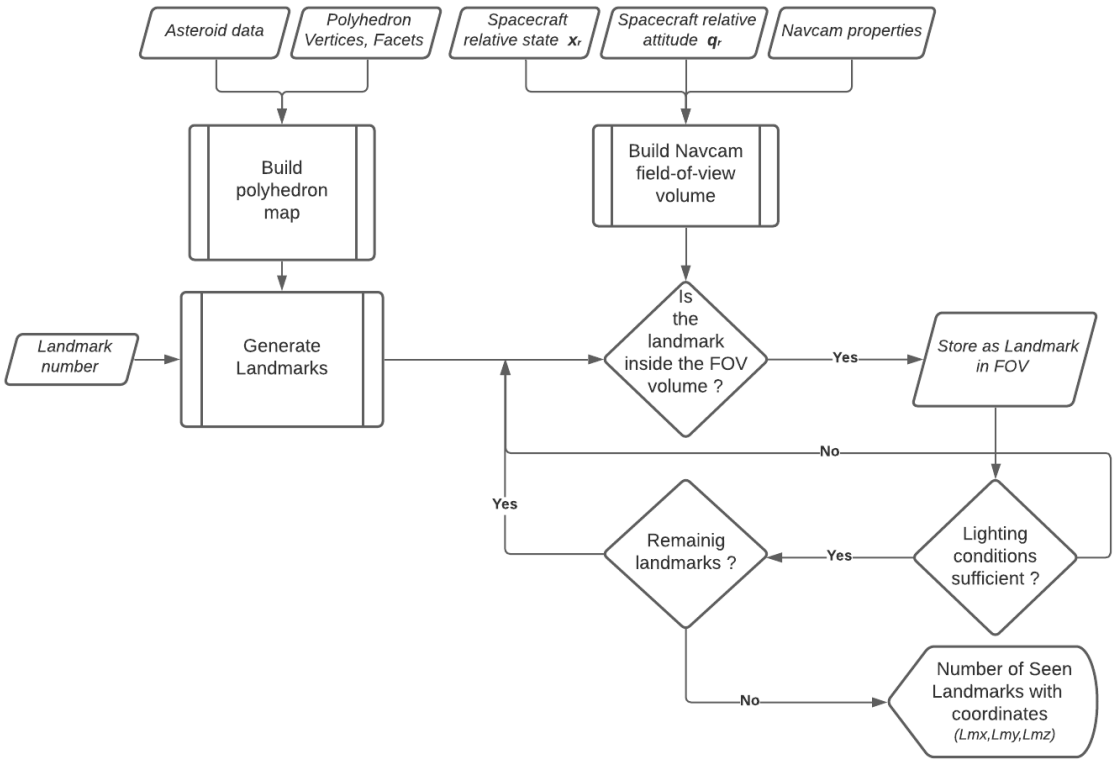


Figure 6.8: Navcam landmarks detection algorithm

ridges, typically attributed to various impacts and events that a navigation camera can detect, which may form the base of the optical navigation process. In this thesis, on the surface of the asteroid, we will create random landmarks, although in fact a pre-process of the asteroid images must be performed to determine the positions of the real landmarks. However, since the exact position of these landmarks can not be known for our thesis, we must consider the landmarks as a random distribution. The distribution of the landmarks over the triangles can be written as (Osada et al., 2002), if we consider a polyhedron model of triangular faces:

$$\mathbf{P} = (1 - \sqrt{r_1})\mathbf{A} + \sqrt{r_1}(1 - r_2)\mathbf{B} + \sqrt{r_1}r_2\mathbf{C} \tag{6.2}$$

with $\mathbf{A}$, $\mathbf{B}$ and $\mathbf{C}$ vertices of a triangle, and $r_1$, $r_2$ random numbers such that $r_1$,$r_2 \in [0, 1]$. The total number of landmarks can be decided on the basis of previous 433 Eros models. We will generate 4600 Landmarks on the surface of Eros on the model of Gaskell et al. (2006), as shown in Figure 6.9.

Once the landmarks are generated over the surface of the asteroid, an algorithm is used to identify the landmarks that are present in the FOV to convert them into vector measurements, based on the spacecraft state and attitude. The first step is to define which landmarks are in the camera's FOV as shown in Figure 6.10. If the Landmark coordinates are located inside this volume, they are stored as Landmarks seen by the algorithm. The lightning conditions are one more condition that should be verified for the landmark to

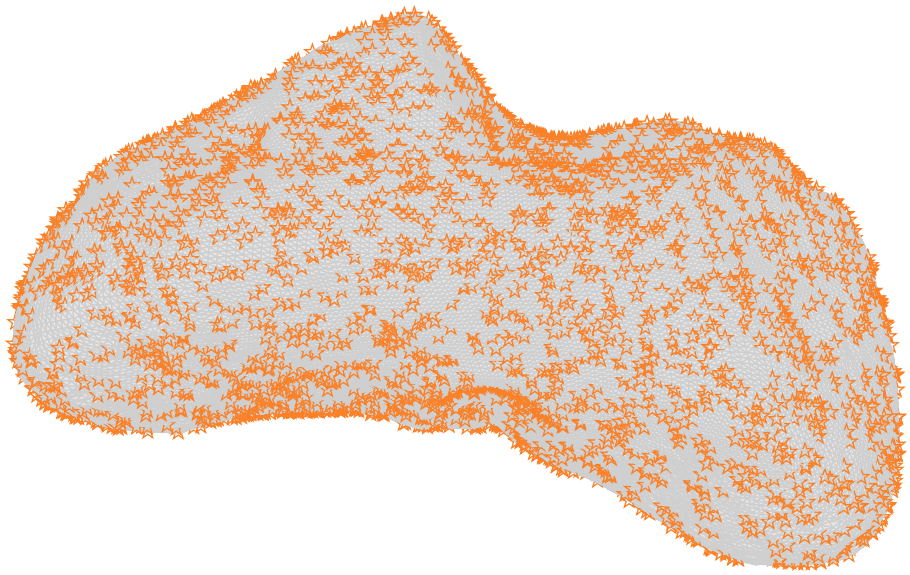

Figure 6.9: 4600 Landmarks generated on the surface of Eros.

be seen by the camera. In fact, if the spacecraft is located in the asteroid's shadow, the lightning conditions are not sufficient for any image to be recorded by the cameras.

The last step that must be done is the generation of the measurement vector from the landmarks position. This can be done following Equations 5.5 to 5.9, where the landmarks position are projected in the pixel plane before being converted to a noisy vector measurement.

### 6.4.2 Lidar

The Lidar model would use the Landmarks in the camera field-of-view to extract the spectrum and to measure the TOF. The time would be updated accordingly to the time-resolution of the Lidar. Acting in addition to the Navcam, the Lidar is capable of giving the range and control angles. The Lidar diagram is seen in Figure 6.11.

## 6.5 Filters model

The two navigation filters to be used are the Unscented Kalman Filter and the Extended Kalman Filter. This section will clarify how they will be applied in the Navigation software, and the results of their algorithms will be compared to the literature to be validated.

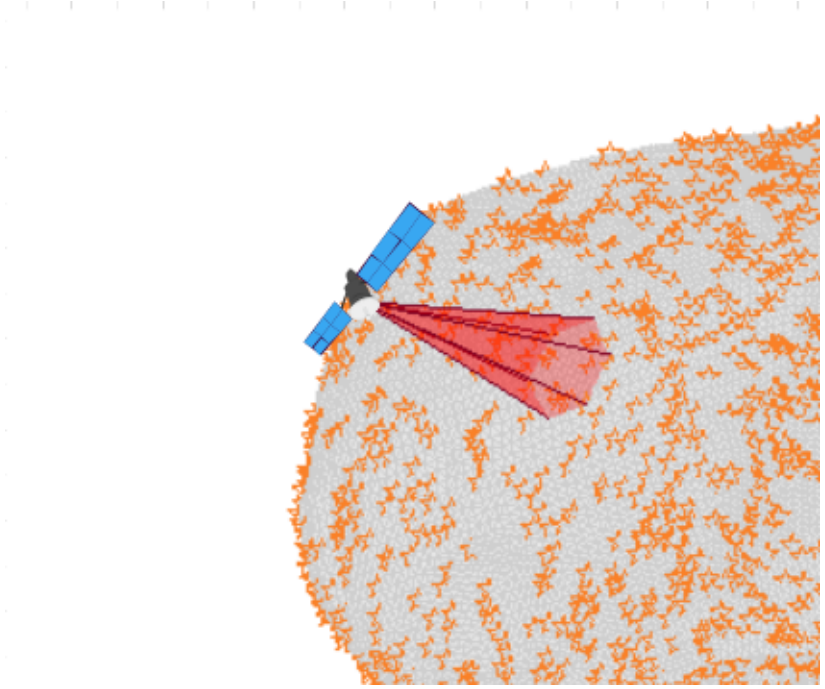

Figure 6.10: Field-of-view of the camera.

### 6.5.1 EKF model

The EKF model will be presented in detail in this subsection. The equations used in the filter model as well as the algorithm applied in the Simulink environment will be discussed. The full model for different scenarios can be found in Annexe A.

#### EKF equations

Starting from the acceleration equation:

$$\ddot{\mathbf{x}}_\mathbf{I} = \mathbf{F_g} + \mathbf{F_{srp}} + \mathbf{F_{3bp}} \tag{6.3}$$

We can write the linearized full state matrix equation:

$$\begin{pmatrix} \Delta\dot{\mathbf{x}} \\ \Delta\ddot{\mathbf{x}} \\ \Delta\dot{\mathbf{c}}_{\mathbf{ij}} \\ \Delta\dot{\mathbf{s}}_{\mathbf{ij}} \\ \Delta\dot{\boldsymbol{\omega}}_{\boldsymbol{R/I}} \\ \Delta\dot{\mathbf{q}}_{\mathbf{R/I}} \end{pmatrix} = \mathbf{J} \begin{pmatrix} \Delta\mathbf{x} \\ \Delta\dot{\mathbf{x}} \\ \Delta\mathbf{c}_{\mathbf{ij}} \\ \Delta\mathbf{s}_{\mathbf{ij}} \\ \Delta\boldsymbol{\omega}_{\boldsymbol{R/I}} \\ \Delta\mathbf{q}_{\mathbf{R/I}} \end{pmatrix} + \begin{pmatrix} \boldsymbol{\nu}_x \\ \boldsymbol{\nu}_v \\ \boldsymbol{\nu}_c \\ \boldsymbol{\nu}_s \\ \boldsymbol{\nu}_\omega \\ \boldsymbol{\nu}_q \end{pmatrix} \tag{6.4}$$

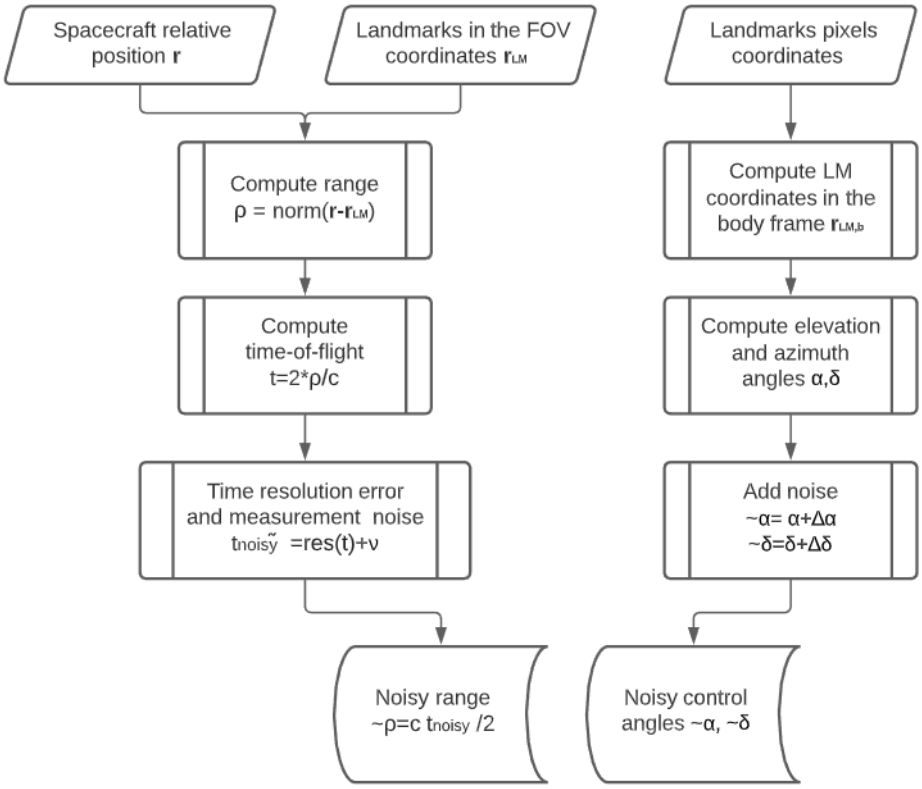


Figure 6.11: Lidar diagram

with $\boldsymbol{\nu}$ the process noise associated with each element of the state and parameter vector, and $\mathbf{J}$ being the following Jacobian matrix, i.e; the matrix of partial derivatives:

$$\mathbf{J} = \begin{bmatrix} \mathbf{0}_{3\times3} & \mathbf{I}_{3\times3} & \mathbf{0}_{3\times m} & \mathbf{0}_{3\times n} & \mathbf{0}_{3\times3} & \mathbf{0}_{3\times3} \\ \left(\frac{\partial\ddot{\mathbf{x}}}{\partial\mathbf{x}}\right)_{3\times3} & \mathbf{0}_{3\times3} & \mathbf{0}_{3\times m} & \mathbf{0}_{3\times n} & \mathbf{0}_{3\times3} & \mathbf{0}_{3\times3} \\ \mathbf{0}_{m\times3} & \mathbf{0}_{m\times3} & \mathbf{I}_{m\times m} & \mathbf{0}_{m\times n} & \mathbf{0}_{m\times3} & \mathbf{0}_{m\times3} \\ \mathbf{0}_{n\times3} & \mathbf{0}_{n\times3} & \mathbf{0}_{n\times m} & \mathbf{I}_{n\times n} & \mathbf{0}_{n\times3} & \mathbf{0}_{n\times3} \\ \mathbf{0}_{3\times3} & \mathbf{0}_{3\times3} & \mathbf{0}_{3\times m} & \mathbf{0}_{3\times n} & \mathbf{I}_{3\times3} & \mathbf{0}_{3\times3} \\ \mathbf{0}_{3\times3} & \mathbf{0}_{3\times3} & \mathbf{0}_{3\times m} & \mathbf{0}_{3\times n} & \mathbf{0}_{3\times3} & \mathbf{I}_{3\times3} \end{bmatrix} \tag{6.5}$$

where $n$ and $m$ are the length of the $c_{ij}$ and $s_{ij}$ vectors respectively, depending on the order and degree of the spherical harmonics expansion. Although the system and measuring equations are not linear, an approximation of the first order is used in the Riccati continuous equations for the $\mathbf{F}$ and $\mathbf{H}$ matrices. The matrices refer to the non-linear

system with the following equations (Zarchan, 2009):

$$\begin{aligned} \mathbf{F} &= \left.\frac{\partial f(\mathbf{X})}{\partial \mathbf{X}}\right|_{\mathbf{X}=\hat{\mathbf{X}}} \\ \mathbf{H} &= \left.\frac{\partial h(\mathbf{X})}{\partial \mathbf{X}}\right|_{\mathbf{X}=\hat{\mathbf{X}}} \end{aligned} \tag{6.6}$$

Recalling the non-linear measurement equation at time k:

$$\mathbf{z_k} = h(\mathbf{X_k}) + \boldsymbol{\sigma_k} \tag{6.7}$$

We can write measurement equations for the sensors that we use in our filter. First, radiometric measurements and star-tracker sensor will simply produce a noisy position and attitude vector:

$$\begin{aligned} \mathbf{z}_{radio} &= \mathbf{x}_I + \boldsymbol{\sigma}_{radio} \\ \mathbf{z}_{STT} &= \mathbf{q}_{B/I} + \boldsymbol{\sigma}_{STT} \end{aligned} \tag{6.8}$$

The navcam will output noisy pixels coordinates of the $i_{th}$ landmark, transformed into the line-of-sight vector, i.e., into unit vector from the camera to the $i_{th}$ landmark, therefore:

$$\mathbf{z}_{Navcam,i} = \mathbf{C}_{B/R}\frac{\mathbf{x}_{LM,i} - \mathbf{C_{R/I}}\mathbf{x}_I}{||\mathbf{x}_{LM,i} - \mathbf{C_{R/I}}\mathbf{x}_I||} + \boldsymbol{\sigma}_{Navcam} \tag{6.9}$$

The Lidar will output range measurements from the $i_{th}$ Landmark of the FOV of the camera, hence the measurement equation for the Lidar is:

$$\mathbf{z}_{Lidar,i} = ||\mathbf{x}_{LM,i} - \mathbf{C_{R/I}}\mathbf{x}_I|| + \boldsymbol{\sigma}_{Lidar} \tag{6.10}$$

The continuous process noise matrix is given by:

$$\mathbf{Q} = E(\boldsymbol{\nu}\boldsymbol{\nu}^T) \tag{6.11}$$

And the discrete measurement noise matrix:

$$\mathbf{R}_k = E(\boldsymbol{\sigma_k}\boldsymbol{\sigma_k}^T) \tag{6.12}$$

where $\sigma_k$ is the noise measurement vector, at time step k. The discrete process noise matrix can be obtained from the PSO, and kept constant for the rest of the simulations.

### EKF algorithm

The EKF algorithm, based on the previous developed equations is resumed in Figure 6.12.

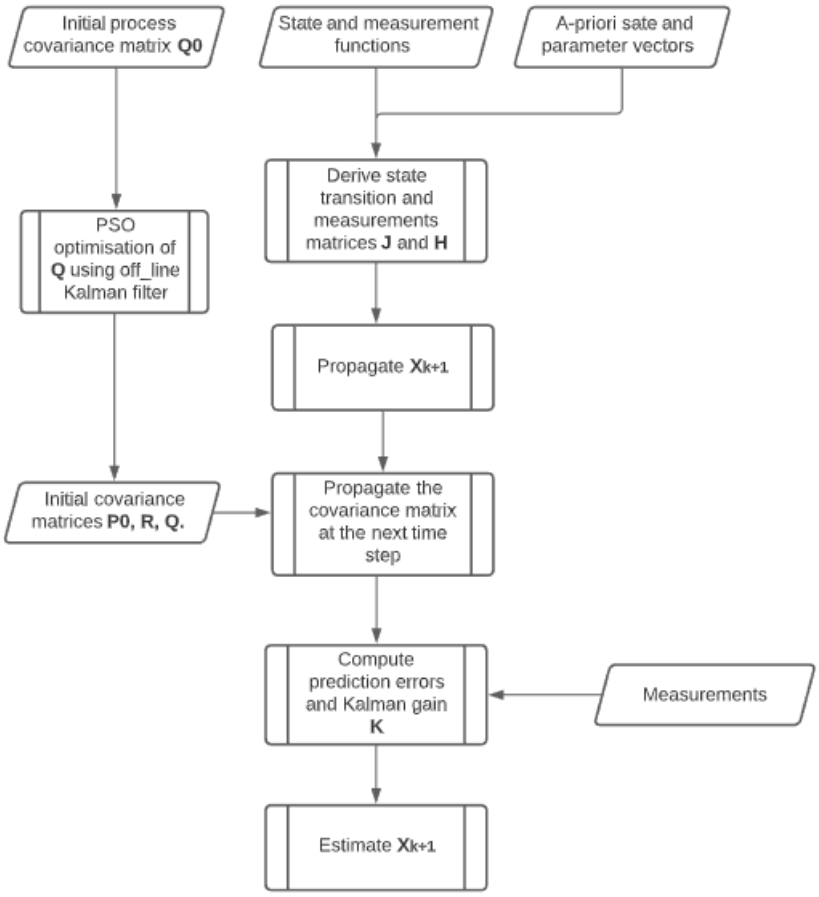


Figure 6.12: EKF algorithm

### 6.5.2 UKF model

Using the software, the UKF will compare its results with the EKF filter. This filter is easier to implement for several state variables and parameter elements as the analytical derivation of matrices is not needed in advance.

#### UKF algorithm

The UKF algorithm implemented in the navigation software is resumed in Figure 6.13

## 6.6 Verification

The simulator will be verified in this section, evaluating the efficiency of the sensors and filters and comparing them with the literature. The sensor models will be verified to see if the sensors are capable of providing the correct information to the filter. Once the EKF

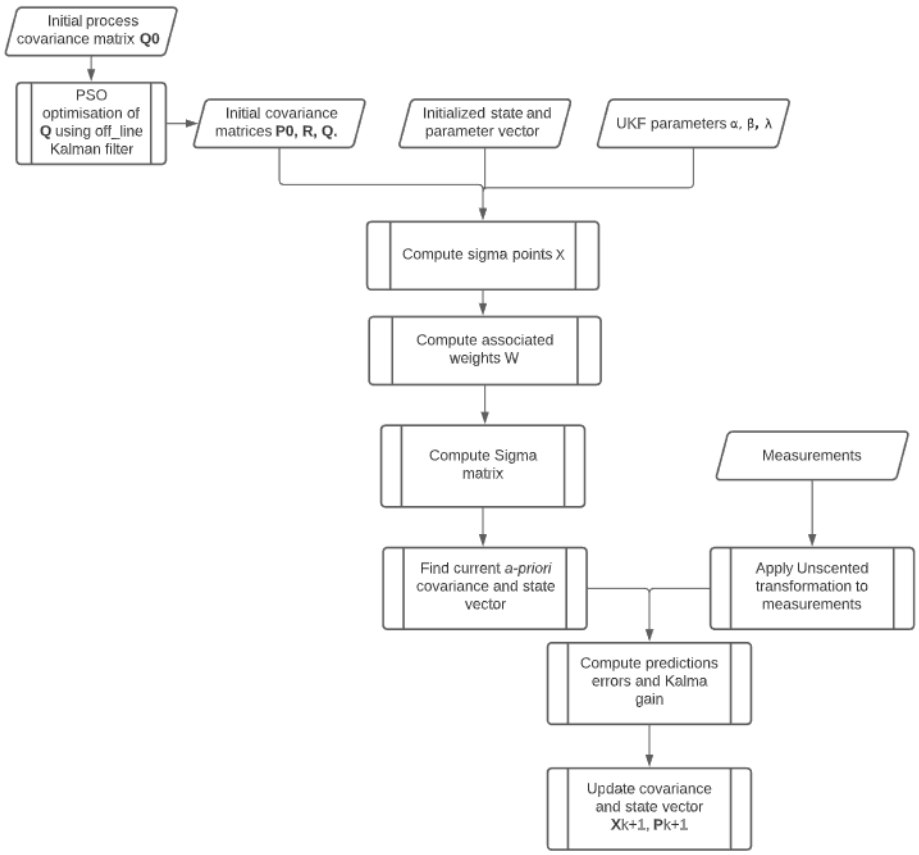


Figure 6.13: UKF algorithm

filter has been verified the performance of the UKF will be assessed for a simple case and compared to the results of the EKF.

### 6.6.1 Navcam

A verification procedure must be followed for the navcam algorithm to determine if the navcam can see the right number of landmarks, with the right positions. The verification procedure is as follows: the navcam FOV will be plotted for the generated set of landmarks, and for a given spacecraft position and attitude. The number of landmarks must then be counted, and must correspond to those found by the algorithm. The focal length is set to f=0.05 m, based on the value of the Near spacecraft camera (Shuang, 2008).

The first verification test is shown in Figure 6.14. We can see that the navcam gives the right number of pixels, corresponding to the landmarks.

The second test is with other conditions, with a new set of landmarks, to confirm the first test and is shown in Figure 6.15. This time, the navcam only sees three landmarks, and it again confirms that the right number of landmarks at exact locations are seen by the camera.

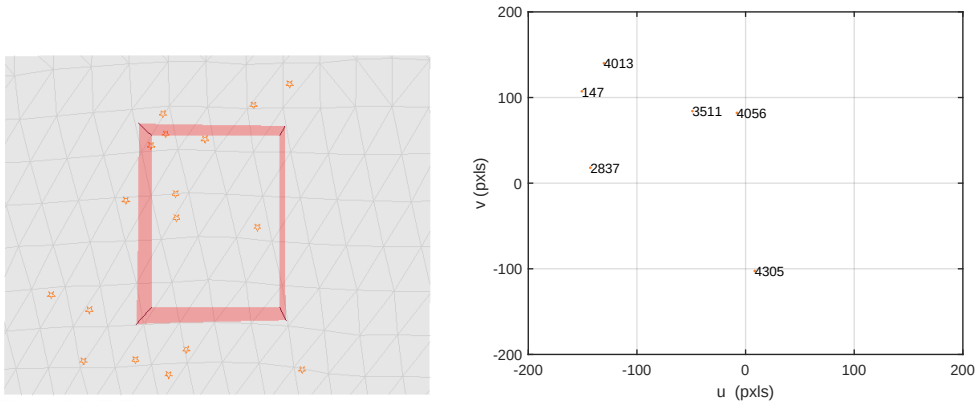


Figure 6.14: Landmarks seen by the navcam, with the corresponding pixels

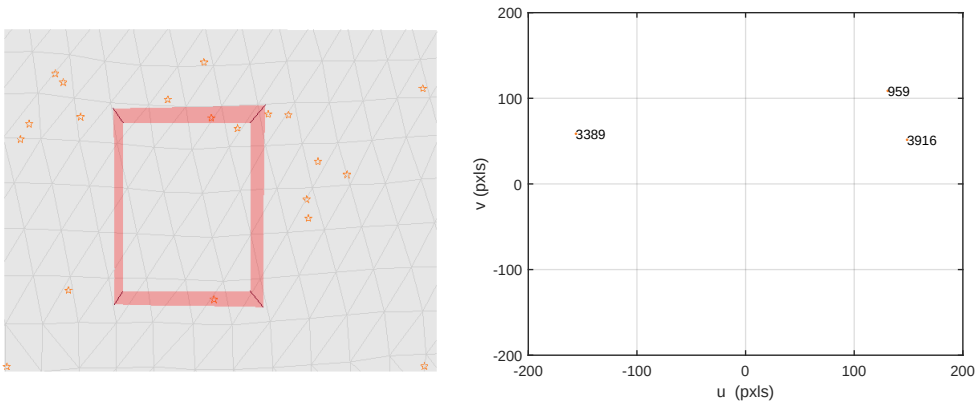


Figure 6.15: Landmarks seen by the navcam, with the corresponding pixels

### 6.6.2 Lidar

The lidar verification procedure will be performed using the FOV Navcam algorithm. If the navcam is able to see the landmarks on the surface of the asteroid, the lidar should be able to provide the same amount of measurements for the landmarks within the camera FOV, with the exact range of elevation and azimuth angles if no noise is introduced, as sown in Figure 6.16.

As expected, if no noise is introduced in the process, the lidar gives values of the range depending on the value of the time resolution of the lidar. Indeed, when increasing the resolution, the range error decreases. We can see in the Figure 6.17 that a time resolution of at least $10^{-9}s$ is required to have an accurate value of the range, which corresponds to nano-seconds.

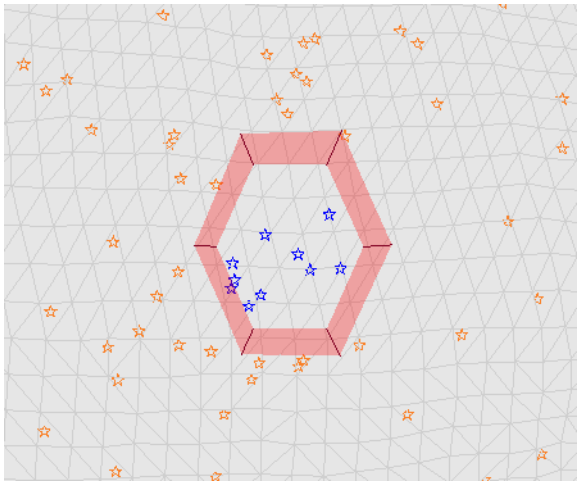

Figure 6.16: Landmarks in the FOV of the camera, recorded by the lidar sensor(in blue).

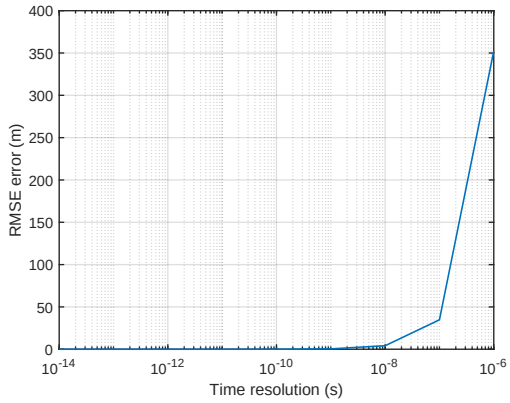


Figure 6.17: Mean RMS range errors in function of time resolution.

### 6.6.3 EKF verification

The extended Kalman filter model has been applied in the case of radar tracking falling object in presence of drag as shown in Figure 6.18. The performances of the filter have been assessed and compared to the results found in the book of Zarchan (2009).

#### First attempt

Setting the process noise $\Phi_s$ equal to zero, and the measurement noise $\sigma_v$ equal to 1000 ft, the results are shown in Figures 6.19 and 6.20. We can see that, although the EKF filter we use behaves slightly better, the results are quite similar with Zarchan's results.

#### Second attempt

Another case was run in which the measurement noise standard deviation $\sigma_v$ was reduced from 1000 to 25 ft. The error in the altitude in this case is reduced but diverges from the

covariance bounds, as shown in Figure 6.21. The error in velocity appears to be growing over the time, as shown in Figure 6.22.

### Third attempt

The third attempt consist in adding process noise to the filter, increasing form 0 to 100 with a noise standard deviation of 25 ft. The process noise appears to be useful to eliminate the divergences in the filter, as shown in Figures 6.23 and 6.24.

The results are shown to be close to the reference model for each attempt, the small differences we observe are due to the noise set we use at each attempt, which is different from Zarchan, so we can conclude that the Extended Kalman filter model is verified.

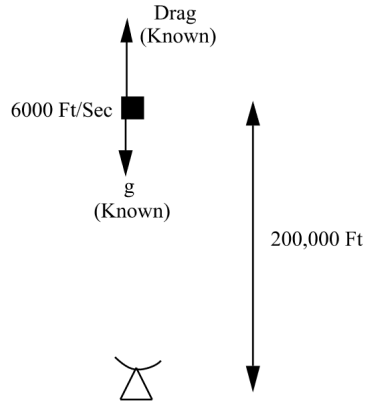


Figure 6.18: Radar tracking falling object, initial conditions

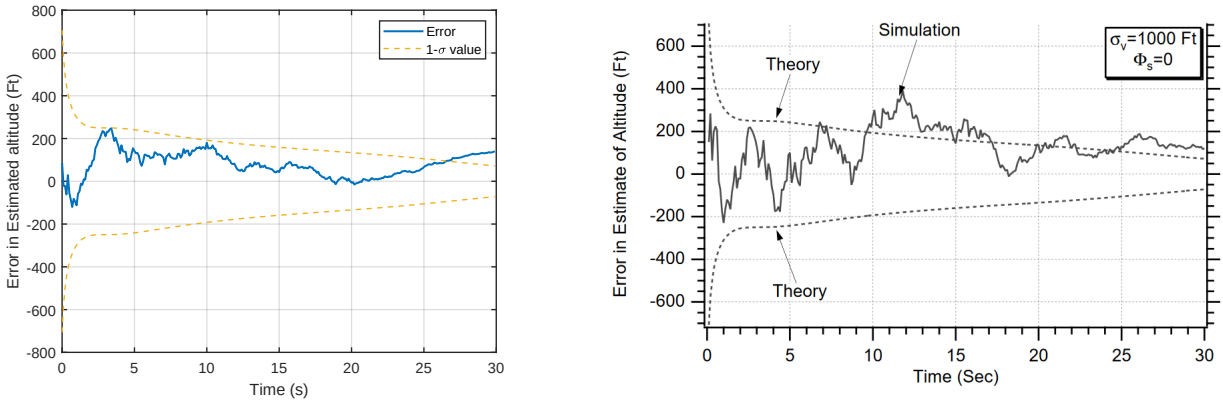


(a) EKF results

(b) Zarchan results

Figure 6.19: Error in altitude, Kalman filter performances.

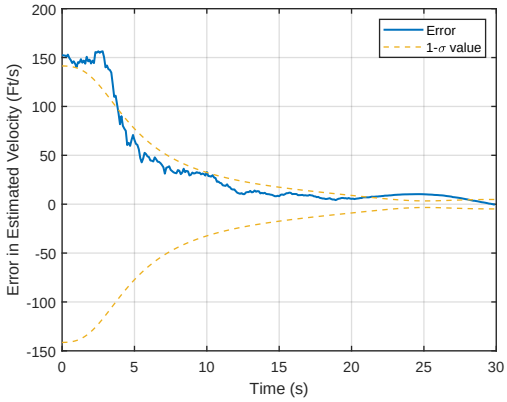


(a) EKF results

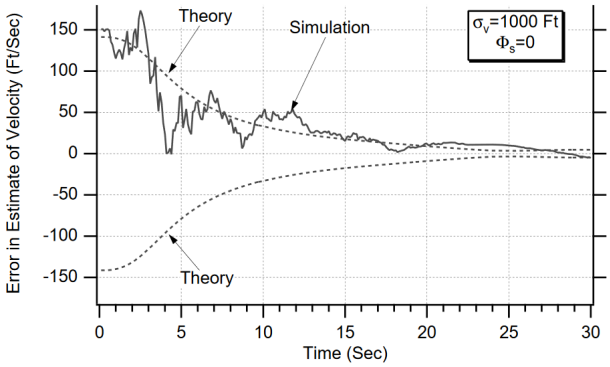


(b) Zarchan results

Figure 6.20: Errors in velocity, Kalman filter performances.

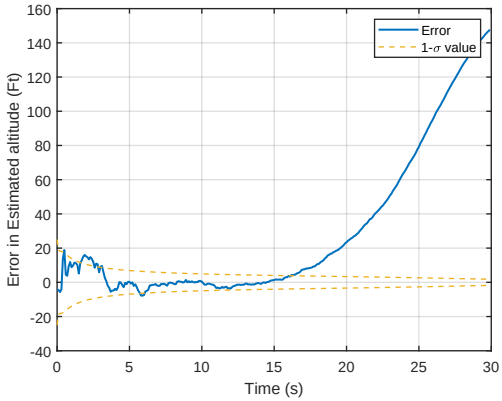


(a) EKF results

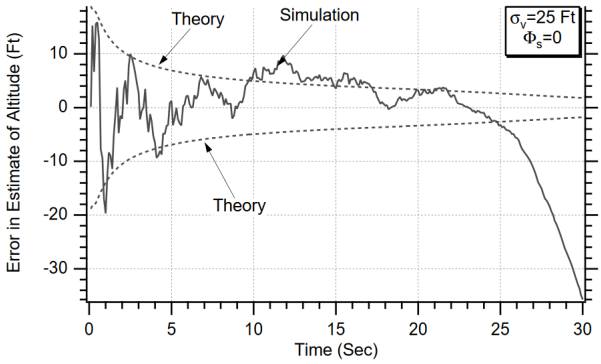


(b) Zarchan results

Figure 6.21: Error in altitude, Kalman filter performances.

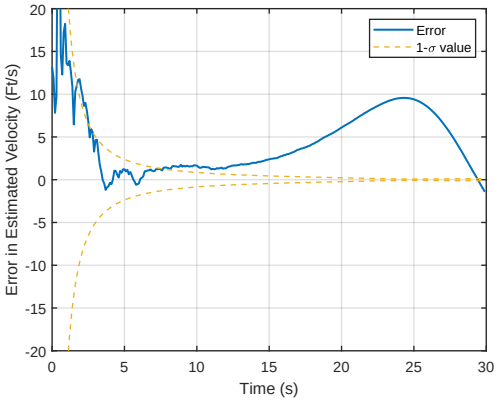


(a) EKF results

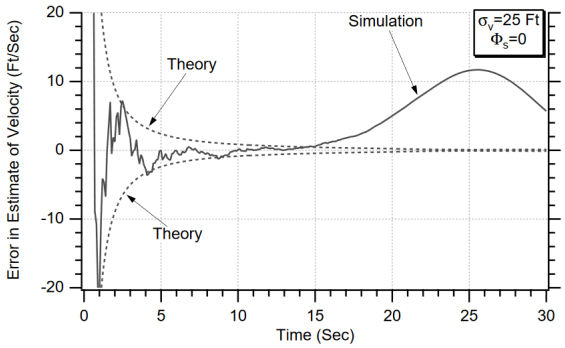


(b) Zarchan results

Figure 6.22: Errors in velocity, Kalman filter performances.

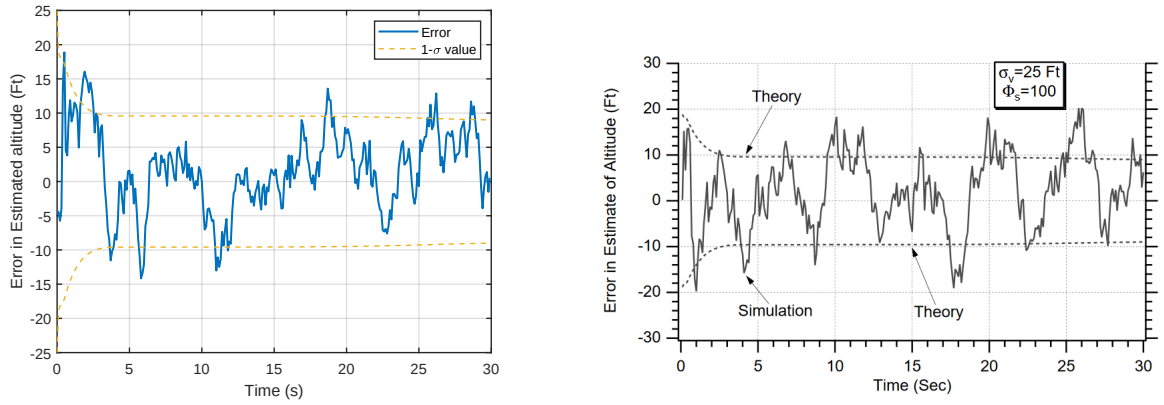


(a) (b)

Figure 6.23: Error in altitude, Kalman filter performances in (6.23a) compared to the results of Zarchan (6.23b)

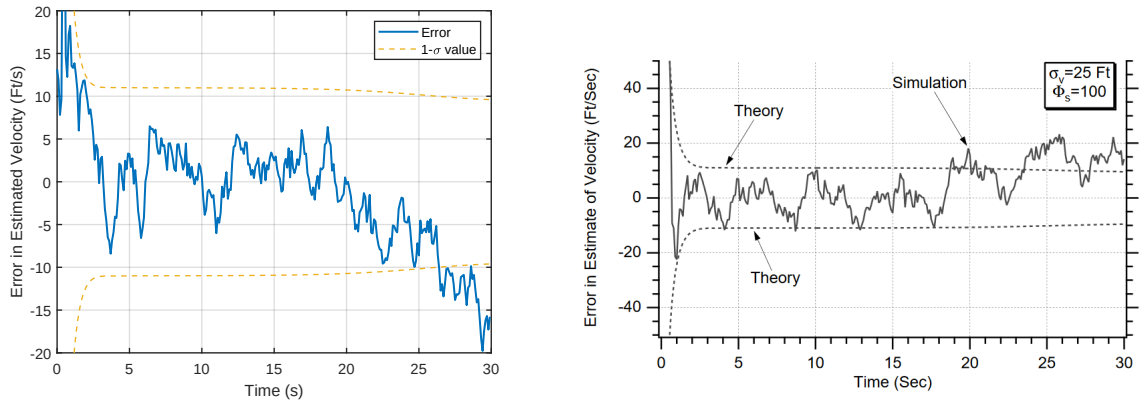


(a) (b)

Figure 6.24: Errors in velocity, Kalman filter performances in (6.24a) compared to the results of Zarchan (6.24b)

### 6.6.4 UKF Verification

EKF and UKF have been applied to compare their efficiency in estimating the $\mu$ parameter and the state vectors, in the simpler case, i.e., the point mass gravity model. Filter values of $\alpha = 0$, $\beta = 2$ and $\kappa = 0$ were selected to tune the UKF.

#### First attempt

On the first try, the noise covariance matrix was set to $\sigma_1$=100 m for the position and $\sigma_2$=10 m/s for the velocity. The process noise matrix is $\Phi_s = [1e-9, 5e-11, 1e-4]$, and not optimised by the PSO to see the effect on the estimation. The output of the two methods with the initial condition $x_0 = [25000, 0, 0]$ for the position is seen in Figure 6.25. With large noise measurements, the Kalman Unscented Filter tends to be more effective

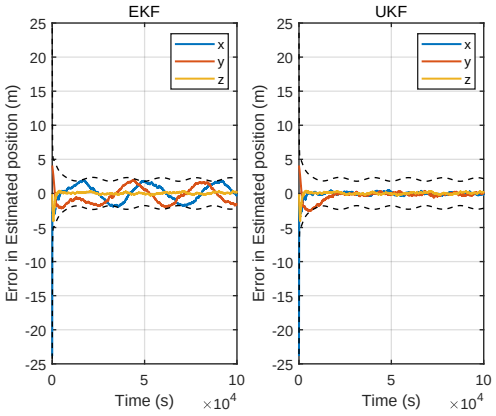


(a) Error in position.

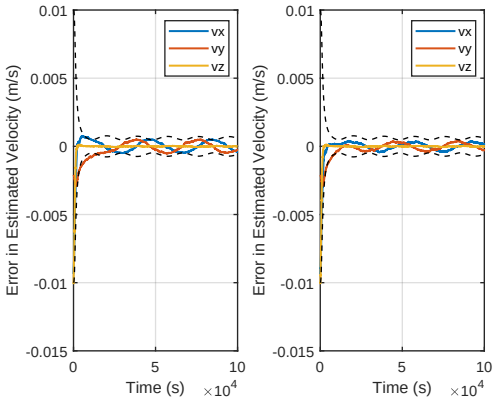


(b) Error in speed.

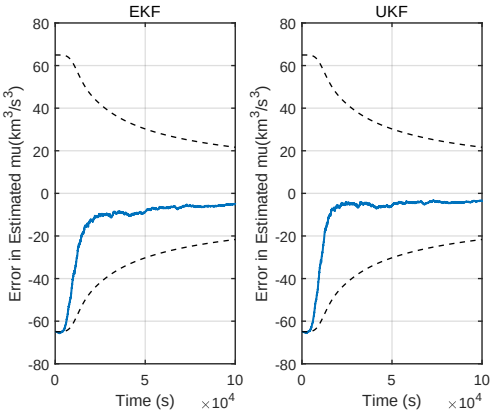


(c) Error in the $\mu$ parameter.

Figure 6.25: Error in states and parameters, first attempt.

than the EKF. In particular, the errors are reduced in position and the convergence is faster in the estimation of $\mu$. The estimate of $\mu$ is very slow to converge in both cases and there is a significant delay until the estimate begins to converge to the real value.

### Second attempt

Reducing the measurement noise to $\sigma_1$=10 m for the position and $\sigma_2$=1 m/s for the velocity, the effects for both filters are seen in Figure 6.26. By reducing the measurement noise covariance, the behaviour of the filters tends to be enhanced with faster convergence and a final error smaller than in the previous example. However, the differences in the results between the UKF and EKF filters are reduced.

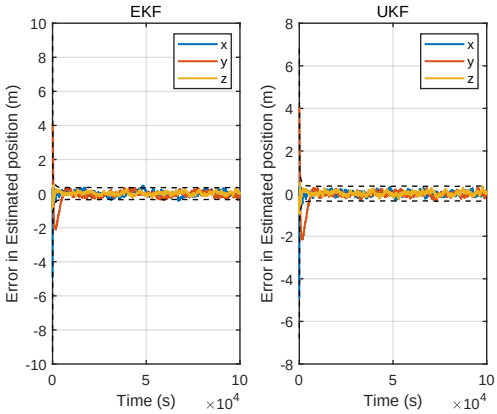


(a) Error in position, second attempt.

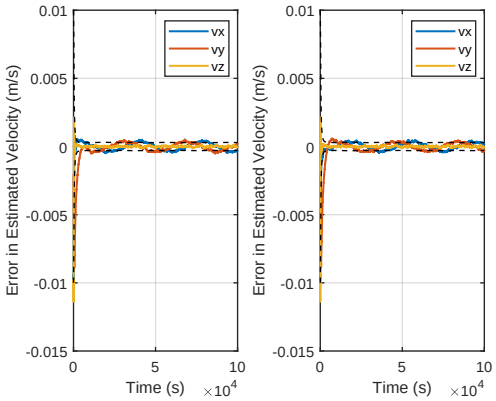


(b) Error in speed, second attempt.

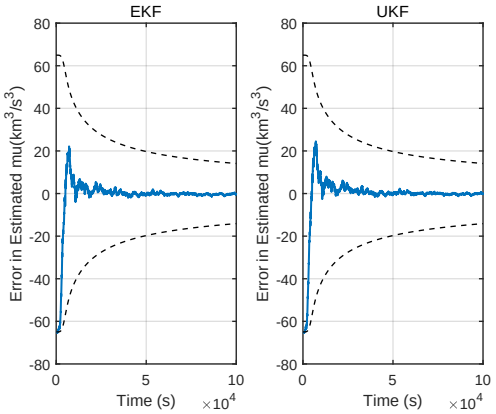


(c) Error in the $\mu$ parameter, second attempt.

Figure 6.26: Error in states and parameters, second attempt.

# 7

# Simulations

This chapter will discuss the simulation scenarios used to test the estimator. It will be split into test cases in which a variety of initial conditions will be changed to see their effects on the estimation process. First, simplified versions will be evaluated and the estimation will be limited to the first order and degree of Spherical Harmonics coefficients. The resolution of the spherical harmonics can then be improved to see if the estimator is able to estimate all these coefficients. For all simulations, real-world dynamics will be propagated using the Spherical Harmonics Gravity Model up to degree and order 22 to ensure high accuracy of the gravity model without high computational workload.

## 7.1 $\mu$ and $J_2$ estimation

The first test will be to estimate the $\mu$ and the $J_2$ parameters at the same time as the spacecraft state vector. The efficiency of the UKF and EKF filters is compared.

### 7.1.1 $J_2$ perturbed environment

The first attempt will consists of reducing the resolution of the real-world spherical harmonics gravity only to the central field with the $J_2$ perturbation. In this case, no other disturbances-gravitational or not-are present in the environment. This basic test allows the efficiency of the various filters to be seen. As this is the most simple test we can provide, we are going to use the noisy position vector as a 'measurement.' Indeed, this test is not reflective of real life, but it may provide an insight into how filters interact with such data. Position measurement noise was set to $\sigma_p = 10$ m.

#### 30 km altitude orbit

The estimation process will be carried out on an orbit of 30 km altitude, with i=60° inclination. The inclination has been chosen different to zero to be able to detect the $J_2$ effect on the system dynamics. The results as shown from Figures 7.5 to 7.8. The results indicate that while the output is slightly improved with the final position error with the UKF, the difference is not significant with the $\mu$ and $J_2$ parameters. In addition, under these conditions, both filters are capable of measuring the state vector and the gravitational parameters with errors inferior to 10% their real values.

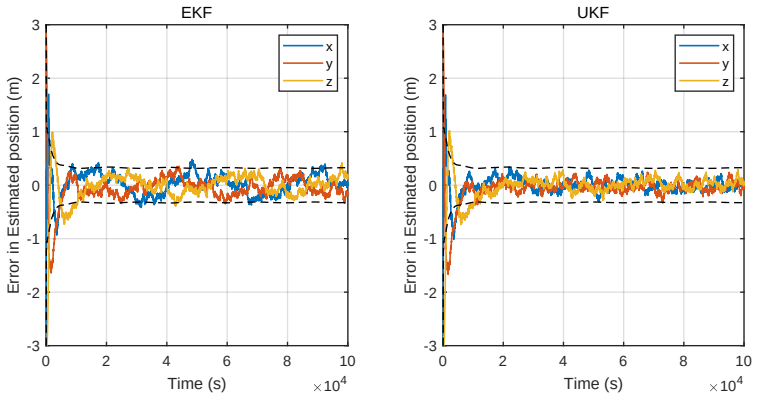


Figure 7.1: Error in position after estimation, first attempt, d=30 km i=60°.

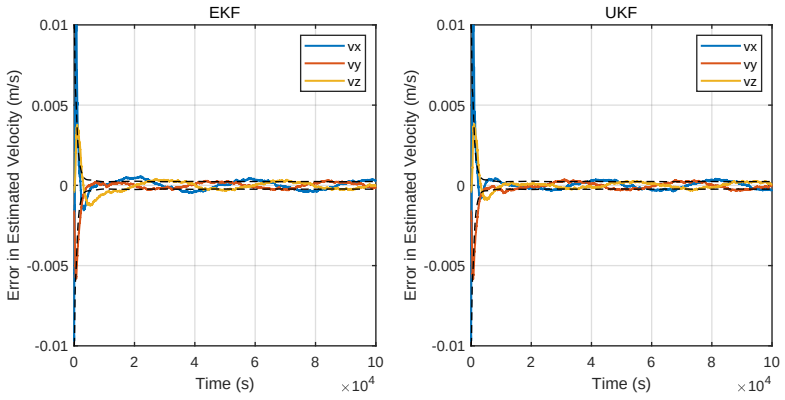


Figure 7.2: Error in velocity after estimation, first attempt, d=30 km i=60°.

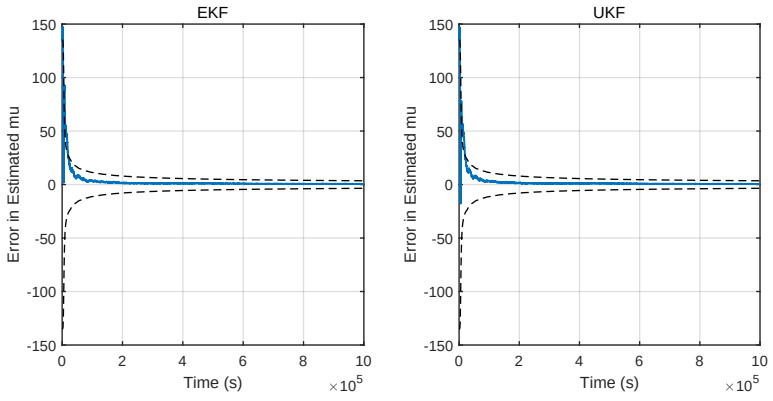


Figure 7.3: Error in the $\mu$ parameter estimation, first attempt, d=30 km i=60°.

### 1200 km altitude orbit

The altitude was raised to 1200 km for the second evaluation. We can see that while the estimate can still be made, the transient behaviour of both filters appears to be growing, which means that the peak we observe at the beginning of the estimation gets larger. This can be explained by the fact that at varying altitudes and at the same time of

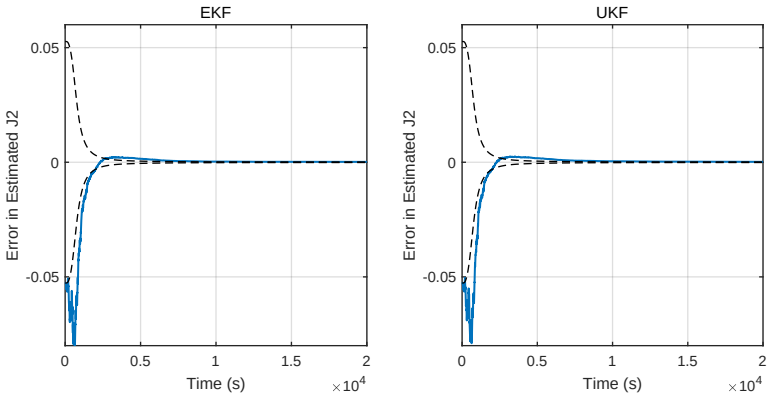


Figure 7.4: Error in the $J_2$ parameter estimation, first attempt, d=30 km i=60°.

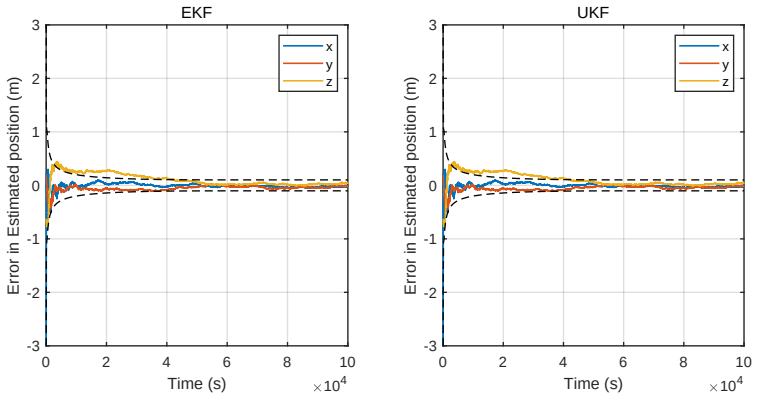


Figure 7.5: Error in position after estimation, second attempt, d=1200 km i=60°.

propagation, the dynamic vector rate of change is different. Indeed, with an orbit closer to the earth, the spacecraft will make more revolutions around the asteroid than it does for higher altitude orbits. This can then be converted into the estimator dynamics, where the process noise covariance matrix is set closer to zero by the PSO, which increases the transient peak in the estimation results. Convergence for the $J_2$ parameter gets slower, directly due to the fact that the effect of this parameter fades at higher altitudes. The orbit tends to be more stable and thus it is more difficult to predict this parameter over a limited propagation time.

### 7.1.2 Conclusion

With this first introduction, we can see in the simulations that the variations in efficiency between the UKF and EKF filters are not significant for this type of estimation. We will therefore now concentrate on the results of the UKF, which appears to be slightly better than the EKF, primarily because the equations are easier to apply for models with a wide number of parameters, as would be used in furture tests. For EKF, each model needs a Jacobian matrix calculation that requires analytical expression or mathematical approximation for each parameter that we want to estimate. It is therefore more convenient to use the UKF, particularly if we want to estimate a large number of spherical harmonic

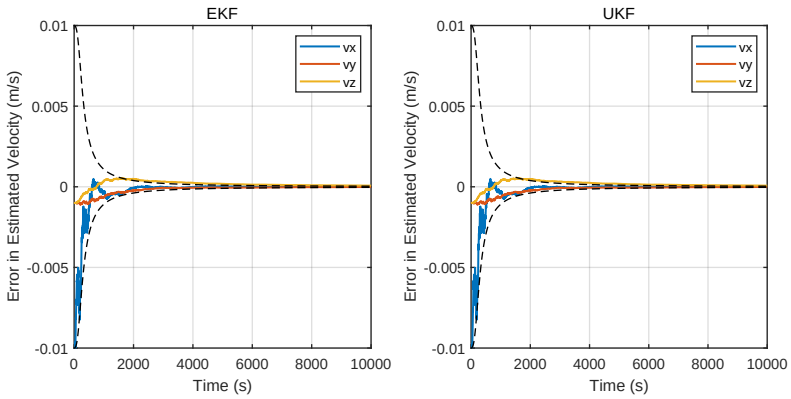


Figure 7.6: Error in velocity after estimation, second attempt, d=1200 km i=60°.

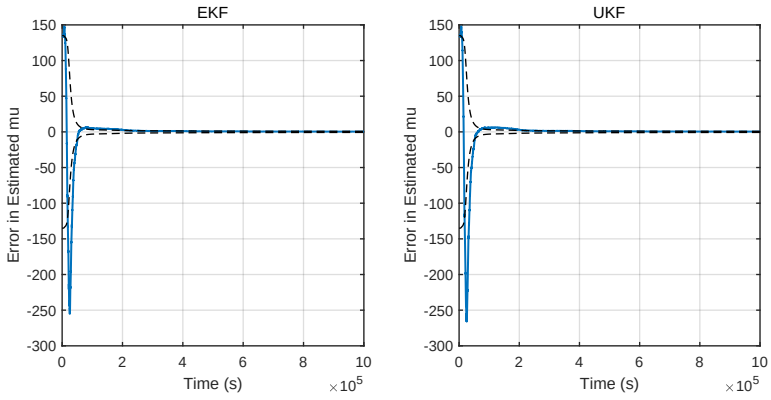


Figure 7.7: Error in the $\mu$ parameter estimation, second attempt, d=1200 km i=60°.

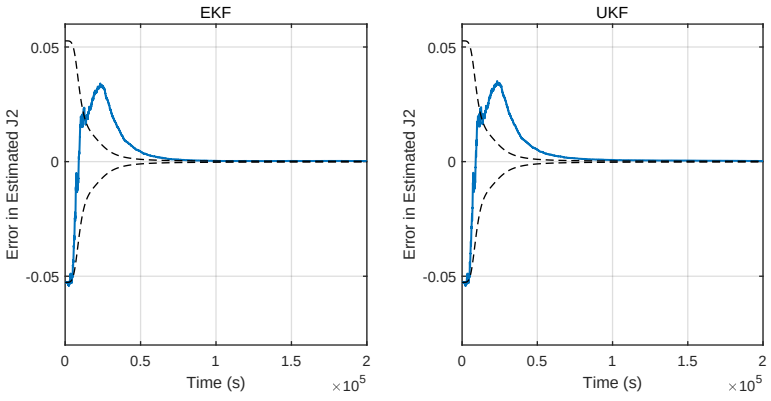


Figure 7.8: Error in the $J_2$ parameter estimation, second attempt, d=1200 km i=60°.

coefficients.

Table 7.1: Estimation results for the $\mu$ parameter for different altitude orbits

| **Distance to the centre of Eros** | **Convergence time (s)** | **Simulation error** | | **Theoretical error** | |
|---|---|---|---|---|---|
| | | $m^3.s^{-2}$ | % | $m^3.s^{-2}$ | % |
| **150** | 19,265 | 966 | 0.2195 | 313 | 0.0711 |
| **250** | 43,948 | 369 | 0.0838 | 277 | 0.0629 |
| **350** | 98,828 | 222 | 0.0504 | 210 | 0.0477 |
| **500** | 184,348 | 56 | 0.0127 | 66 | 0.0150 |
| **1000** | 417,932 | 41 | 0.0093 | 198 | 0.0223 |

## 7.2 Third-body perturbation effect

Increasing the accuracy of the real-world simulator model, the third-body perturbation is one of the main disturbances that can influence the dynamics of the spacecraft. The effect of this disturbance on the estimation process will be detailed in this section.

### 7.2.1 Results

From Earth to the asteroid, the spacecraft is subjected to many gravitational forces.When the Sphere of Hill of Eros is crossed, the spacecraft will orbit around Eros with a stable orbit. When reaching the Sphere of Influence (SOI), the gravitational effect of other bodies, such as the Sun, can be ignored and the problem reduced to the well-known two-body problem. As shown in previous gravitational maps, the further the spacecraft is from the centre of Eros, the more the gravitational field of Eros is felt by the spacecraft as a central field force. The objective of this section is to find the optimum distance in such a way that the $\mu$ parameter can be estimated alone as accurately as possible, to use the value in the next estimation step, i.e., the estimation of the second higher perturbations.

In an ideal world, where only Eros and the spacecraft exist, and where all other forces and perturbations can be neglected, we should expect that the farther we are from the centre of Eros, the more precisely we can estimate the $\mu$ parameter, because increasing the distance means that spherical harmonics disturbances will fade away. Indeed, that is what we observe in Table 7.1, where the moving mean of the estimation error decreases with the distance to the centre of Eros. The initial *a-priori* value of $\mu$ has been initialised with an error of $4.0135 \times 10^4$ $m^3.s^{-2}$ compared to the true value. We also note that the time of convergence increases with distance, possibly due to the fact that the gravitational influence of Eros is diminishing. This explains the value of the 1000 km orbit, which is higher than the estimated value of the 500 km orbit. Although the convergence is slower and the simulation time remains the same, the error value at the end of the simulation is higher with slower convergence.

In the real world, the higher gravitational perturbation after Eros is due to the Sun, located at a distance $d_{Sun} = 218.155 \times 10^6$ km from Eros. The radius of the SOI of Eros is therefore $R_{SOI} = 366.437$ km, while the radius of the Sphere of Hill is $R_H = 2255.70$ km when Eros is located at the semi-major axis of its orbit around the sun. As shown in Figure 7.9c, the ratio between the main and perturbing acceleration increases exponentially with the distance. Therefore, we should expect that, by neglecting this disturbance in the

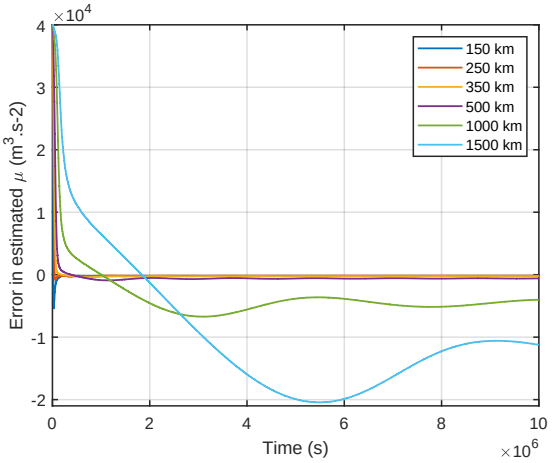


(a) Error in the $\mu$ estimation in function of time for different altitude orbits.

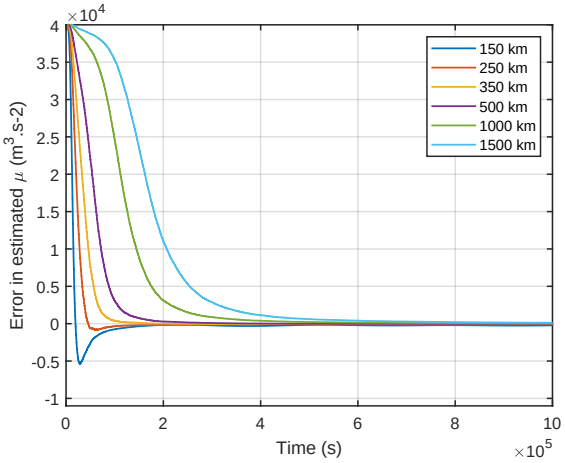


(b) Estimation error of the $\mu$ parameter in function of time for different altitude orbits.

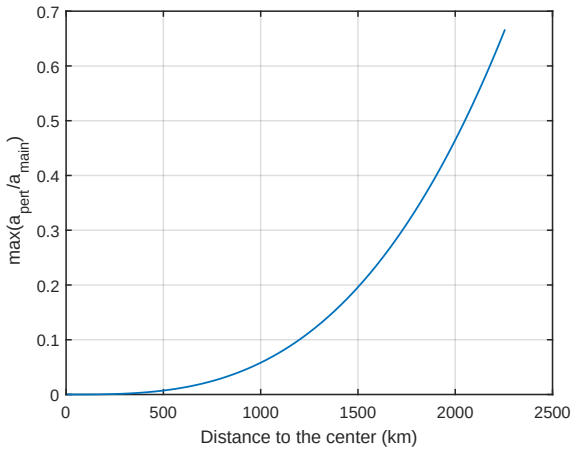


(c) Maximum ratio between the perturbing and main acceleration.

Figure 7.9: Third-body perturbation effect on the orbit and estimation procedure

estimation model, once we reach $R_{SOI}$, the performance will begin to decay. This is shown in Figure 7.9a, where a set of orbits are taken at different distances from the centre of Eros to estimate the parameter $\mu$, neglecting the Sun 's contribution to the dynamics of the spacecraft. Closer to the asteroid, the disturbances due to the highly irregular shape or Eros are getting larger, and it becomes more difficult to isolate the $\mu$ parameter. In the reverse situation, the Sun 's contribution becomes greater when the distance from the centre of Eros increases, and the estimation of the $\mu$ parameter alone becomes difficult as well.

It is not complicated to take into account the third-body disturbance in the estimated model, since we already know the Sun's gravitational parameter $\mu_{Sun}$. The only variables are the position of the Sun and the position of the spacecraft with regard to Eros. Including this perturbation in the estimation model by calculating this perturbation at

Table 7.2: Estimation results for the $\mu$ parameter for different altitude orbits

| **Distance to the centre of Eros** | **Convergence time (s)** | **Simulation error** | | **Theoretical error** | |
|---|---|---|---|---|---|
| | | $m^3.s^{-2}$ | % | $m^3.s^{-2}$ | % |
| **150** | 19,155 | 233 | 0.0527 | 135 | 0.0307 |
| **250** | 43,726 | 82 | 0.0186 | 110 | 0.0250 |
| **350** | 100,039 | 50 | 0.0114 | 81 | 0.0184 |
| **500** | 193,571 | 32 | 0.0073 | 75 | 0.0170 |
| **1000** | 438,645 | 34 | 0.0077 | 190 | 0.0432 |
| **1500** | 690,705 | 120 | 0.0273 | 432 | 0.0982 |

each step, based on the relative position of the sun with respect to the spacecraft, the results are displayed in Table 7.2 and Figure 7.9b. Compared with the previous model, we can observe that the divergences of the filter are corrected. The convergence time still increases with the distance to the centre of Eros, hence the large theoretical and estimated values for the 1000 km and 1500 km orbits.

### 7.2.2 Conclusion

- In an ideal world in which Eros is the principal gravitational body and all other perturbations can be ignored, increasing the distance will increase the filter's convergence time, but will reduce the estimation errors.
- As we get closer to the asteroid, the disturbances due to Eros's highly irregular gravity field will be stronger, and thus estimating the $\mu$ parameter alone will be more and more complicated.
- If the third-body perturbation due to the influence of the Sun is included in the real-world simulator, after we reach the SOI, the performances of the filter will decrease exponentially.
- Including the third-body perturbation in the estimated model will correct for the previous divergences of the filter, and will increase the performances of the filter compared to the previous case. The optimum distance to estimate the $\mu$ parameter in this case is around 500 km, for a low convergence time and the best filter performances.

## 7.3 Effect of the Solar radiation pressure on the estimation

Another disturbing force that can influence the spacecraft's dynamics is the Solar Radiation Pressure (SRP). The effect of the SRP in the estimation procedure will be detailed in this section.

### 7.3.1 Results

The SRP is the principle of massless electromagnetic waves, which possess mass-like properties. The photons in the light produced by the Sun travel and have momentum at the speed of light. Since they have momentum, when they reach the spacecraft, they transfer momentum to the spacecraft. The momentum that these photons bear is, however, extremely small. Thus, in spacecrafts orbiting Earth, the perturbing force is not really detected, but it is a disturbance that can not be ignored when orbiting an asteroid of small mass and size. When a spacecraft is huge, exposed in the light or moving slowly, the SRP perturbation is stronger. Since the gravity field of Eros is weak, the SRP perturbation effect is stronger when increasing the distance to the centre of Eros, as we can see in Figure 7.10.

When attempting to estimate the $\mu$ parameter, it becomes very important to take the SRP into account. It is wise to start by estimating the $\mu$ at a sufficient distance from the centre to avoid all the irregular shape and density effects on the dynamics of the spacecraft, as already seen in previous sections. But the gravitational acceleration due to the Eros gravity field becomes weaker as the distance to the centre increases, and hence the disturbances coming from the sun become greater. This is what we see in Figure 7.11a, where we can see that, ignoring the SRP, the estimate diverges after reaching 250 km from the centre of Eros. Unlike the third-body perturbation, it is complicated to estimate the SRP perturbation. It depends on several parameters, such as the orientation of the spacecraft with respect to the sun, the size of the spacecraft or its reflectivity. In past missions, the SRP was the first parameter to be estimated before estimating the gravity field of the main attracting body. Since the estimation cannot be perfectly accurate, some estimation errors (up to 10%) will be taken into account when the SRP is implemented in the estimation model. Figure 7.11b shows that taking into account the SRP, the divergences are eliminated. In the same way as in the previous case, increasing the distance to the centre increases the convergence time. This is probably due to the fact that the gravitational influence of Eros is becoming weaker and that the spacecraft will see less of the surface of Eros for the same amount of propagation time. In the case of a high altitude orbit ($>$ 500 km), the error in the SRP estimate introduces an error in the $\mu$ estimate, as can be seen in Table 7.3. It is therefore important to estimate the SRP as accurately as possible before estimating the $\mu$ at high distance from the centre of

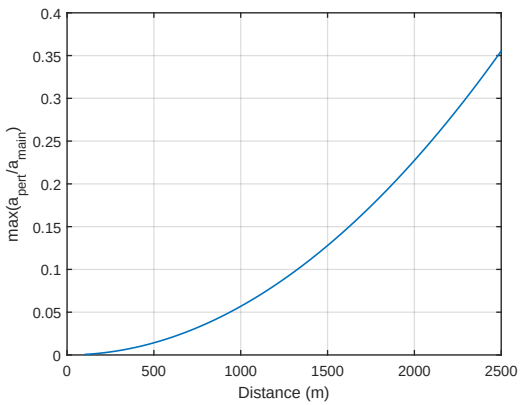


Figure 7.10: Maximum ration between the SRP perturbing and main acceleration.

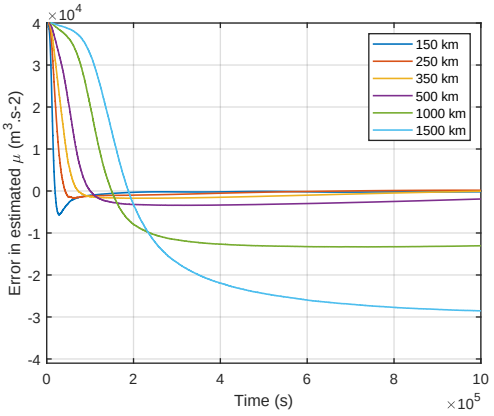


(a) $\mu$ estimation for different altitudes orbit, ignoring the SRP.

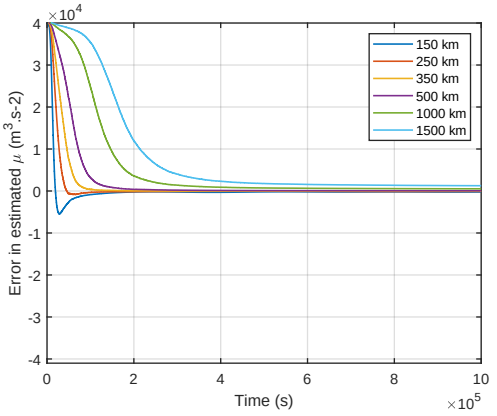


(b) $\mu$ estimation for different altitudes, taking into account the estimated SRP.

Figure 7.11: $\mu$ estimation results.

Table 7.3: $\mu$ simulation results

| **Distance to the centre of Eros (km)** | **Simulation error** | | **Theoretical error** | |
|---|---|---|---|---|
| | $m^3.s^{-2}$ | % | $m^3.s^{-2}$ | % |
| **150** | 235 | 0.0534 | 135 | 0.0306 |
| **250** | 96 | 0.0218 | 110 | 0.0249 |
| **350** | 48 | 0.0109 | 81 | 0.0184 |
| **500** | 49 | 0.0111 | 72 | 0.0163 |
| **1000** | 110 | 0.0249 | 318 | 0.0722 |
| **1500** | 550 | 0.1242 | 789 | 0.1792 |

Eros.

### 7.3.2 Conclusion

- The effect of the SRP on the orbit increases with the distance to the centre and results in a force acting in the opposite direction to the vector position of the Sun in the asteroid frame.
- Not taking into account the SRP in the estimation process result in a divergence of the filter for high altitude orbits.
- Taking into account an estimated SRP in the process eliminates the filter divergences but introduces error in the final estimate of $\mu$.

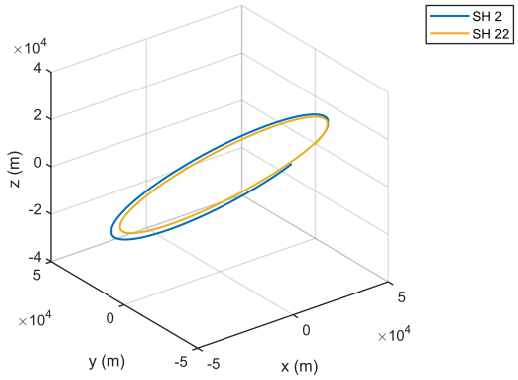


Figure 7.12: Spacecraft orbit propagated using two different maximum degree for the spherical harmonics expansion, degree 2 and 22.

## 7.4 Gravity resolution

The gravity field resolution will depend on the degree of expansion selected for the expansion of spherical harmonics. The higher the degree, the closer the gravity field model will be to the real gravity field of the asteroid. We have seen that while the polyhedron gravity field can give the most precise modelling results, the spherical harmonics model can give similar results when only the estimate outside the radius of the reference sphere is taken into account. The estimate is therefore only suitable for the characterisation phases, but not for the landing phases. In the estimation procedure, the modelling of spherical harmonics is also easier to implement, since it requires only the estimation of finite numbers of coefficients that can be used to directly calculate the acceleration felt by the spacecraft at each step. Moreover the low computational time compared to the polyhedron model is the main advantage of the spherical harmonics model.

The objective of this section is to find a trade-off between the computational time and the resolution of the spherical harmonics expansion, since we can not just decide to estimate the spherical harmonics coefficients up to infinity. In the end, the degree of expansion of spherical harmonics must be sufficiently high to reduce errors in the final estimation of the state. In Figure 7.12 between a spherical harmonics model of order 2 and 22, the error in position in a 50 km orbit is displayed. As expected, we can see that the error increases with time in the spacecraft's position and velocity, as shown in Figure 7.13, compared to the more precise model.

Indeed, as we can see in Figures 7.14, increasing the resolution of the spherical harmonics model, the errors in position and velocity of the spacecraft are reduced. If we take into account the propagation of the states in time, the small error at the beginning is added to the next step until the propagation time is reached, which is why the final position or velocity errors could have large values even with a high resolution of the approximate gravity model. That is why we used the spherical harmonics model in the simulator model until order 22, to reduce these errors as much as possible. This is not, however, the case in the estimation procedure. Since we estimate using the measurements for the next time step at each instant, the errors in the propagation are not added to each other linearly. This is why in the estimator model we can allow a decreased resolution of

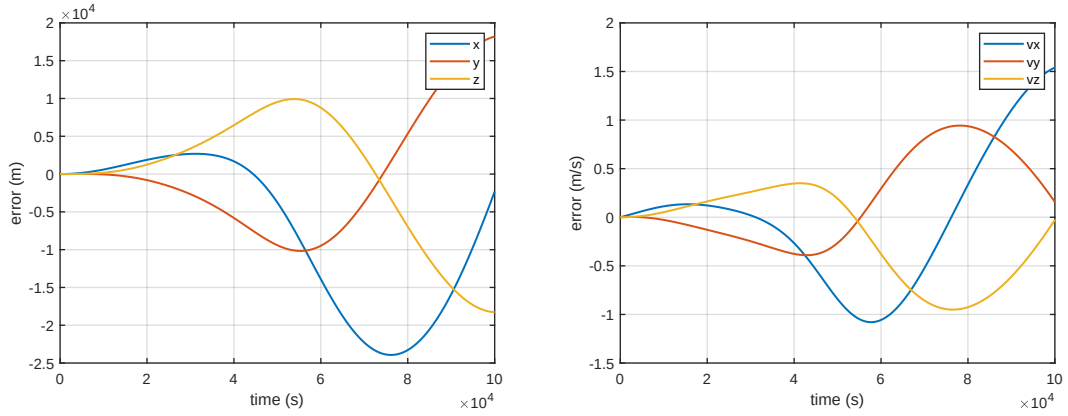


(a) Error in position (b) Error in velocity

Figure 7.13: Error between states propagated with the SH-2 and SH-22 gravity model

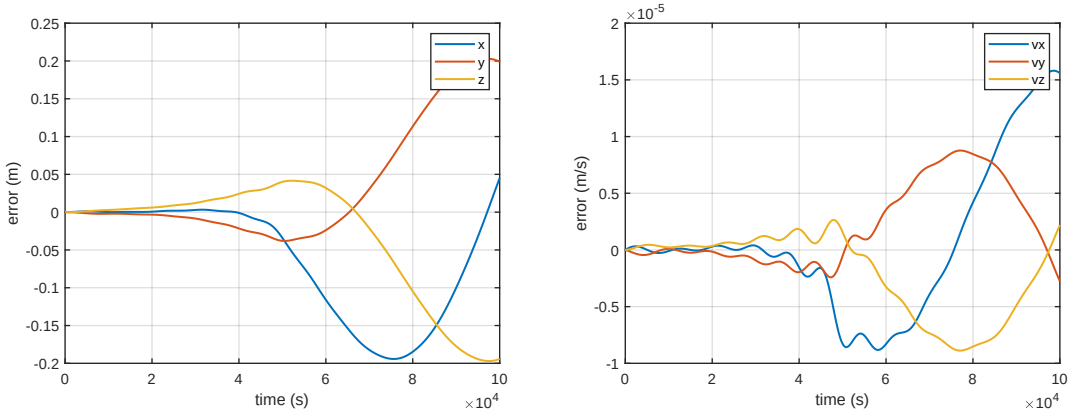


(a) Error in position (b) Error in velocity

Figure 7.14: Error between states propagated with the SH-8 and SH-22 gravity model

the gravity field.

The differences in the propagation of orbits according to the resolution of the orbit can be explained by the difference in the acceleration of the gravity field felt by the spacecraft. As the gravity field resolution increases, the differences in gravitational accelerations between the different gravity resolutions tend to decrease and thus reduce the differences in the spacecraft's dynamics. In Figure 7.15, this is what we observe by plotting the differences in gravity accelerations for various resolutions for a sphere of 16 km radius corresponding to the maximum radius of Eros. Since the difference between the degree 12 and 8 are as large as the differences between the degree 7 and 8, we can assume that this degree of expansion will be sufficient for the estimation procedure. This is also what we could observe in 7.14, where the initial differences in position and velocity induced by the gravity field were small.

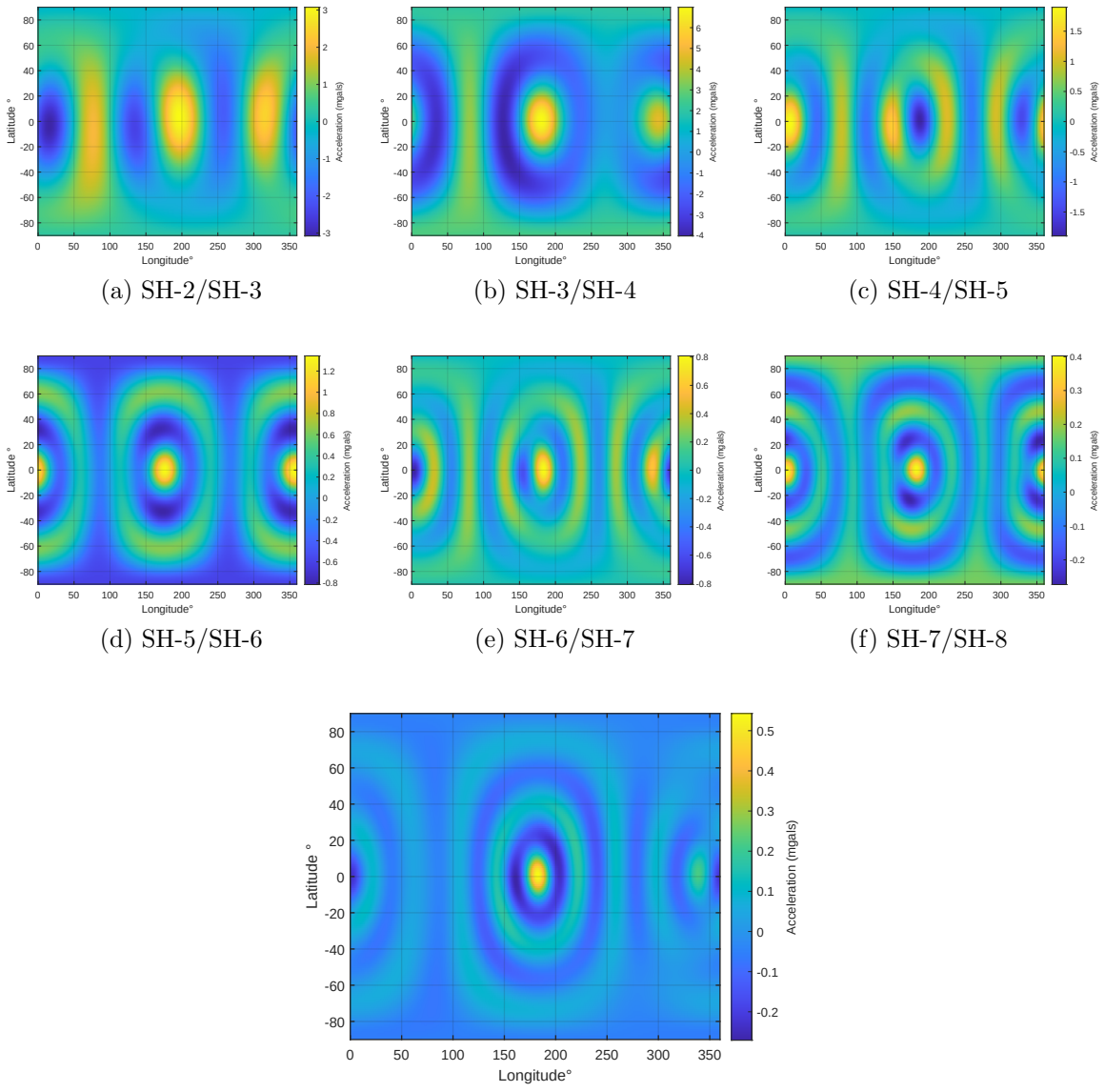


(a) SH-2/SH-3 (b) SH-3/SH-4 (c) SH-4/SH-5

(d) SH-5/SH-6 (e) SH-6/SH-7 (f) SH-7/SH-8

(g) SH-8/SH-12

Figure 7.15: Differences in gravity field on a sphere of 16 km radius, and in function of the degree of expansion (SH-i denotes the spherical harmonics expansion of degree i).

## 7.5 Spherical harmonics coefficients estimation

We will attempt to estimate the coefficients of spherical harmonics up to degree and order 8 in this section. In an environment where only a noisy position vector is available as a measurement, we will begin with an estimate of the maximum coefficients. We can test the estimator in different conditions by setting the position noise quite high, to see any improvement in the results. Real measurements will be implemented in the estimator and tested in the Near-Shoemaker mission scenario when different conditions are tested.

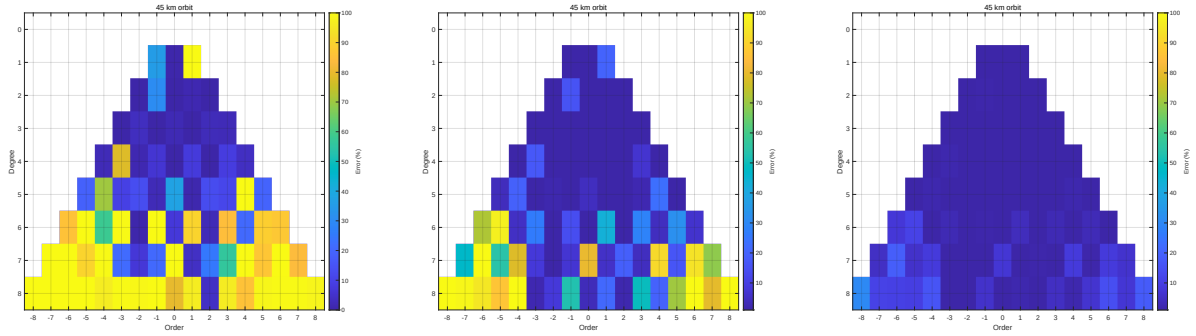


(a) $\sigma_p = 1000$ m (b) $\sigma_p = 100$ m (c) $\sigma_p = 10$ m

Figure 7.16: Estimation errors in function of the position measurement error $\sigma_p$

### 7.5.1 Effect of position noise on the estimation

For the first attempt, under different noise position errors, we will try to estimate these coefficients, where the position noise, $\sigma_p$, ranges from 1 km to 10 m. The propagation time is chosen to be t=10,000,000 s for this estimation. The spacecraft is launched into a polar circular orbit at an altitude of 45 km at the beginning of the estimation. The results of the estimation are shown in Figures 7.16, where the final estimation error is shown for all estimated coefficients. The negative degree coefficients represent the $s_{ij}$ coefficients, while the positive values represent the $c_{ij}$ coefficients. These results indicate that reducing the error in the position makes it possible to estimate higher degrees coefficients. This can be explained by the fact that the small changes in the dynamics due to the high spherical harmonic values are hidden by high noise on the position vector. Therefore the measurement noise should be as low as possible to allow the spherical harmonic coefficients of high order degrees to be felt in system dynamics for optimal estimation. We can also see that with $\sigma_p$= 10 m, it is possible to estimate all coefficients up to degree 8. A 10 m error in the measurements can be envisaged with current sensor technologies.

### 7.5.2 Effect of the range and inclination on the estimation

The spacecraft should cover the maximum surface area to feel the effect of every component of the asteroid 'irregular gravity field. In the estimate, coverage is of major significance as poor coverage can lead to divergences in estimated coefficients. It is more complicated to estimate the $J_2$ effect under specific conditions, such as equatorial orbits. There are two major dependencies in the coverage of the surface, the time-of-flight and the inclination.

The inclination is the first element that we can think of. The inclination increases the surface area seen by the spacecraft for the same major axis orbit and time-of-flight, as shown in Figures 7.17a, 7.17b and 7.18. The maximum latitude and longitude are restricted by the initial inclination angle.

Time-of-flight also plays an important role in the procedure of estimation. Increasing the flight time results in a higher estimation time, but it does not always lead to higher

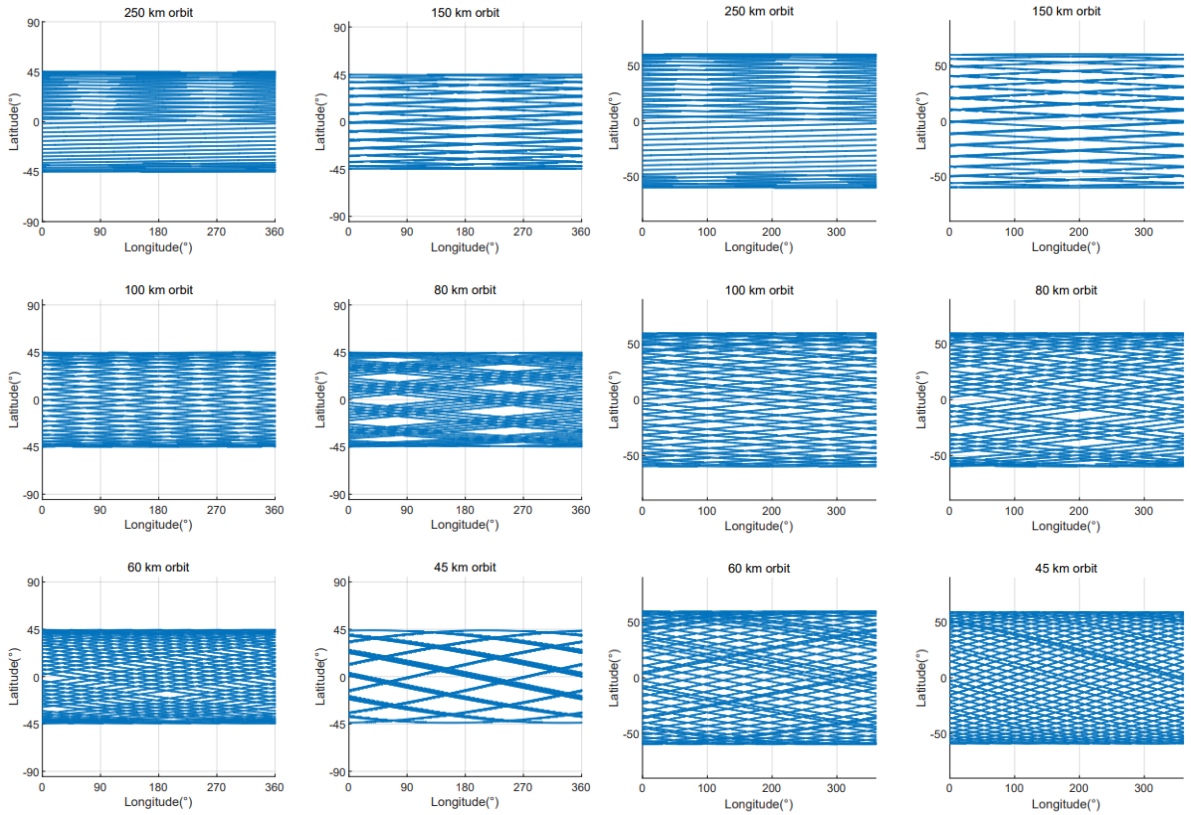


(a) i=45° (b) i=60°

Figure 7.17: Coverage plot for different altitudes orbit, with an inclination of i=45°and i=60°.

coverage. Under certain conditions, every period T, the projected orbit on the surface repeats the same scheme. Such special orbits are called repeat ground-track orbits. For a time-of-flight of 3,000,000s, in Figure 7.17a, for i=45 °, the orbit seems to be repeated every period, and therefore it leads to uncovered areas in the estimation process. It is the same effect we observe for i=90° with a distance of 150 km form Eros in Figure 7.18. These orbits must therefore be avoided. Repeat orbits for i=90° are shown for different semi-major axis, and in function of the repeat time, in Figure 7.19. We can see that the closer we are to the surface, the more repeated orbits we can find. This is only due to the fact that the orbit can make more revolutions around the asteroid closer to the surface, and therefore more repetitive orbits can be found.

To investigate the effects of the range and the inclination on the estimation procedure, we reduce the propagation time to t=100,000s and use the position as a measurement with $\sigma_p$=1 km. Under these conditions, we do not expect the estimated time to be sufficient for the estimation of all coefficients. However, this technique allows us to see under which conditions the estimation procedure converges more quickly. From Figures 7.20a to 7.20c, it can be seen that a reduction in the distance to the centre of Eros allows a better estimation of higher degree coefficients. This is due to the fact that as we have seen before, increasing distances means reducing the effects of these higher degrees parameters on the dynamics of the spacecraft. Increased inclination also improves the efficiency of

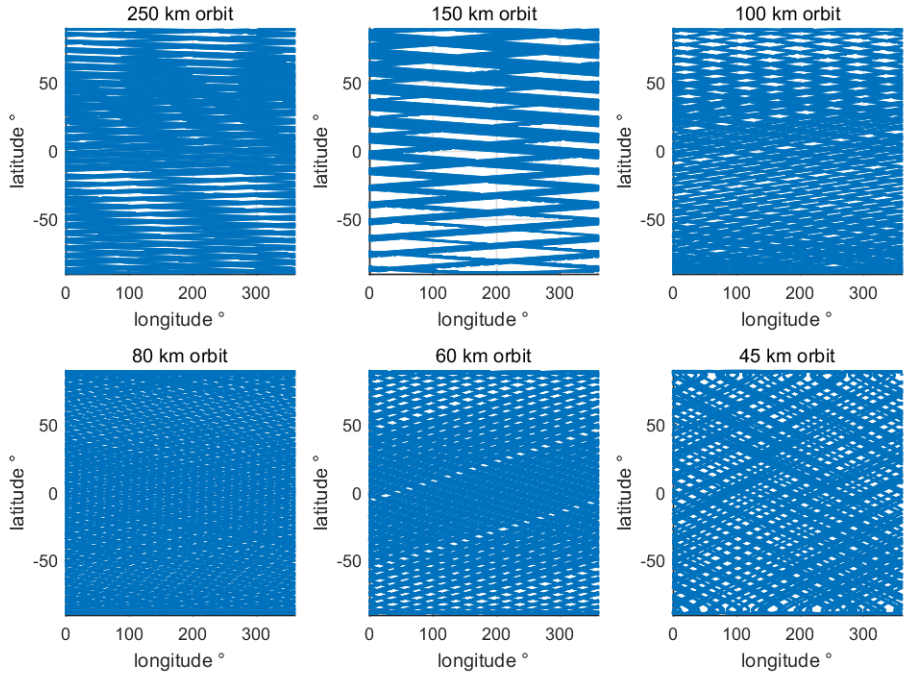


Figure 7.18: Coverage plot for different altitudes orbit, with an inclination of i=90°.

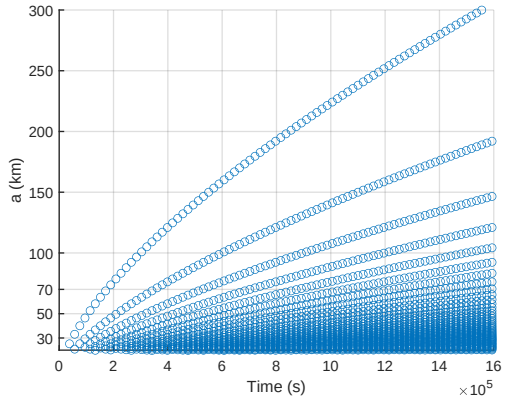


Figure 7.19: Repeat orbits in function of the semi-major axis and the repeat time

the estimation. This is due to the effect of coverage, because with a high inclination, the spacecraft covers more of surface and, combined with the rotation effect, allows much more of the surface areas than with low inclinations orbits.

### 7.5.3 Conclusion

- Even with with bad conditions, i.e., only highly noisy position as a measurement, small propagation time and not optimum orbits, the $c_{10}$ and $c_{20}$ coefficients can be estimated with a high accuracy.

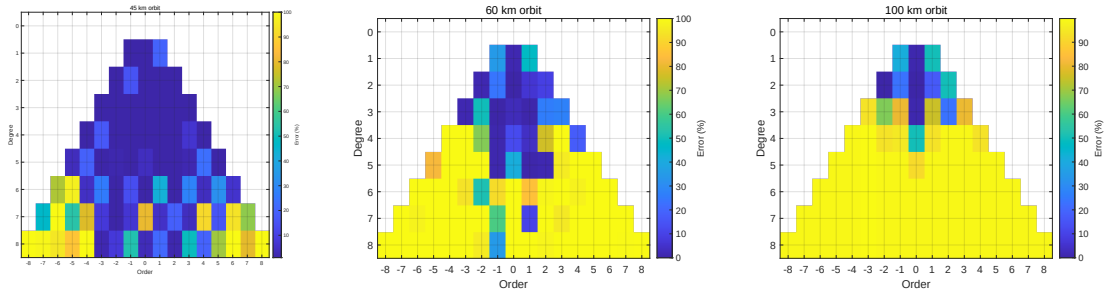


(a) 45 km orbit (b) 60 km orbit (c) 100 km orbit

Figure 7.20: Estimation results for the spherical harmonics coefficients in function of the altitude.

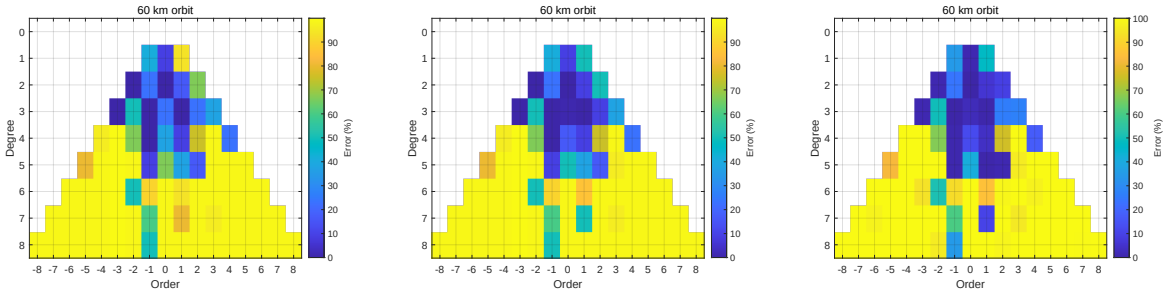


(a) i=45° (b) i=60° (c) i=90°

Figure 7.21: Estimation results for the spherical harmonics coefficients for a 60 km orbit, and an inclination of i=45°, i=60°and i=90°.

- Repeat orbits must be avoided for optimum coverage of the surface.
- Decreasing the distance to the surface of the asteroid, higher degree coefficients can be estimated. This is due to the fact that the effect of the disturbances decreases with the distance to the centre, and because the higher degree of disturbance has a smaller dynamical effect, it is harder to feel this effect for high altitude orbits.
- To make the estimation procedure more efficient, the inclination of the orbit should be as close as possible to 90°. In the case of polar orbits, combined with the rotational rate of Eros, coverage is optimum. Therefore, these orbits should be preferred for the coefficient estimation.

## 7.6 Parameters effect on the estimation

As we have seen, the further away we are from the asteroid, the harder it becomes to estimate the spherical harmonics coefficients of high order and degree. However, some parameters, such as the $\mu$ and $J_2$ parameters, have effects strong enough to be felt on the dynamics of the spacecraft at high altitudes. It is therefore possible to estimate these parameters in the early stages of the mission. Some other coefficients have strong

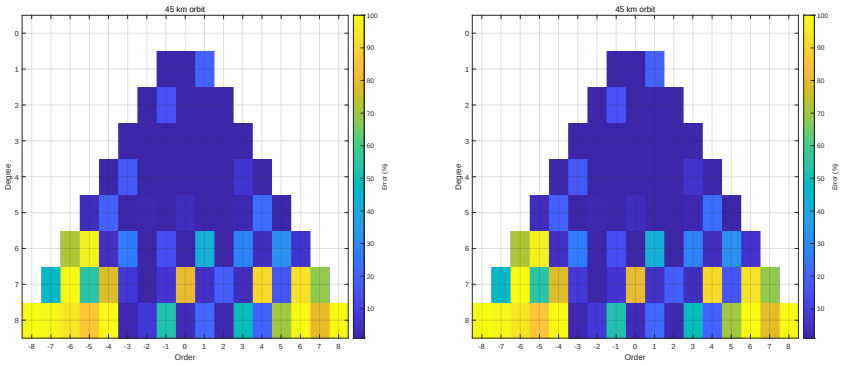


(a) $\mu$ and $J_2$ coefficients estimated (b) $\mu$ and $J_2$ coefficients removed from the estimation

Figure 7.22: Spherical harmonics coefficients estimation errors, with and without the first-order and degree coefficients in the estimation.

physical means, such as the first degree coefficients, which represent a shift from the centre of gravity to the centre of mass, and can therefore be also deducted earlier in the mission. If these parameters are removed from the estimation procedure, we should not necessarily expect an improvement in the estimation results. For example, since the estimator can easily estimate the parameters $J_2$ and $\mu$, the rest of the estimation time is spent only on estimating the other coefficients, and therefore the results should not be improved.

### 7.6.1 Removing the $\mu$ and $J_2$ parameter from the estimation

The first step in investigating the effects on the estimation parameters is to remove the main gravitational parameter $\mu$. Since this parameter contributes to the central field, it is the main contribution to the acceleration felt by the spacecraft. Therefore, and as we have shown before, taking into account SRP and third-body disturbances, the $\mu$ parameter can be estimated very precisely in the early stages of the mission, with an error of maximum 0.2%. The $\mu$ parameter will be removed from the estimation procedure, assuming a constant value with an error of 0.2%, and the $J_2$ will be assumed to be a constant with 1% error to evaluate the effects of these parameters on the estimation results. For a 45 km orbit, the results are compared in Figure 7.22 with the previous case, where $\mu$ and $J_2$ were a part of the estimation procedure. As shown in Figure 7.22, the estimation results are not actually improved. This was expected because the filter estimate the $\mu$ and $J_2$ parameters very quickly with high accuracy, and therefore there is no reason for this test to have an effect on the rest of the estimation procedure.

### 7.6.2 Removing the first-order and degree coefficients from the estimation

We have seen in 7.16 that, especially when we consider highly noisy measurements, first order and degree coefficients can be more difficult to estimate. However, they represent

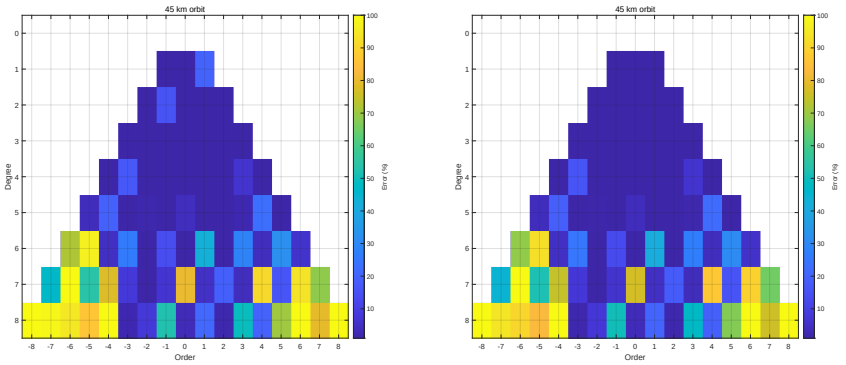


(a) First-order and degree coefficients estimated

(b) First-order and degree coefficients removed from the estimation

Figure 7.23: Spherical harmonics coefficients estimation errors, with and without the first-order and degree coefficients in the estimation.

a shift in the centre of the figure from the centre of the mass, which can be obtained by multiplying the first order and degree coefficients by the reference sphere radius (16 km). For the Near NLR Gravity Model, the centre shift is small and equal to [9.7 m, 2.4 m, 32.6 m], however for the shape model, the shift is reduced to less that 1 m for every axis, which explains why it is difficult to estimated them. This shift can be obtained independently from the estimation procedure, so we will choose to remove these coefficients from the estimated model to see if any improvements can be made with the estimation results. In Figure 7.23 the estimation results are compared for a 45 km polar orbit, with $\sigma_p = 100$ m. We still assume that the $\mu$ and $J_2$ coefficients are estimated earlier in the mission, and therefore are not estimated with the rest of the coefficients. We can observe that the removal of the first order and the degree coefficients form the estimate slightly improves the performance of the filter. For instance, the $s_{21}$ error can be estimated below 10% error, which was not the case when attempting to estimate these coefficients at the same time. It also improves the convergence of higher order and degree coefficients.

### 7.6.3 Adding the rotational rate of the asteroid in the estimation

When attempting to estimate the spacecraft's position and velocity, the rotational rate of the asteroid is a very important parameter to know. Since gravitational acceleration depends on where the spacecraft is located with respect to the asteroid's surface, it is important to know the relative position of the spacecraft in relation to the asteroid and therefore to know the asteroid's dynamics. For the prior estimates, the rotational rate of the spacecraft was assumed to be known. In real missions, however, this rotational rate must be estimated, because its dynamics are supposed to be unknown before the encounter with the asteroid. Together with the estimation of the $\mu$ and $_2$ parameters, the estimation of the asteroid's rotational rate is one of the first estimates being conducted. Once the landmarks are generated on the surface of the asteroid, this rotational rate can be measured by just measuring the displacement of the landmarks in the camera's

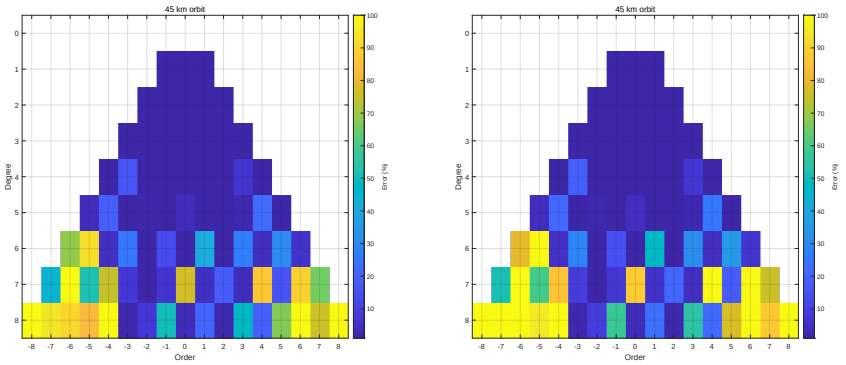


(a) Given attitude and rotational rate (b) Estimate attitude and rotational rate

Figure 7.24: Spherical harmonics coefficients estimation errors, with and without the first-order and degree coefficients in the estimation.

field-of-view. However, far from the asteroid, this process is more efficient, that is, when the entire surface of the asteroid is present in the camera field-of-view. Using noisy position and rotational rate as measurements, with $\sigma_p$=100 m and $\sigma_w$= 50 degrees/day, the estimation process has been carried on a 45 km polar orbit. The estimation was based on the previous estimation, that is without the $\mu$, first-order and degree coefficients and $J_2$. The results are shown in Figure 7.25, where we can see that the estimation performances are reduced only for the 7 and 8th order and degree coefficients. We can clearly see in these conditions, such as the previous tests, that the higher degrees are more difficult to estimate. This could be because the estimation time is not sufficient, or the orbit is not optimal for these coefficients to be estimated.

### 7.6.4 Conclusion

- Removing the $\mu$ and $J_2$ parameters does not influence the estimation results, due to the fact that these parameters can be estimated quickly and very accurately.
- Removing the first-order and degree coefficient improves the estimation results, probably due to the fact that they are complicated to estimate when the coverage is not optimum and the shift in the centre of Figure from the centre of mass is small.
- The integration in the estimation process of the rotation rate and asteroid attitude reduces the performance slightly, or at least increases the convergence time. However, using the movement of landmarks in the Navcam field-of-view, the rotational rate can be estimated early in the mission stages.

## 7.7 Mission scenario

Since only a limited set of measurements can be made available for a real mission, the first step in improving model reality would be to move from a noisy state vector to an ideal yet real measurement model. Two types of measurements available in real systems are inertial and relative measurements. The inertial position can be determined through the DSN, which is the only sensor capable of delivering direct inertial data. The range and range rate, which are relative quantities, can be determined by the lidar sensor, and the relative location and attitude can be measured by the navcams and the star trackers. We will attempt to reproduce the mission stages of the Near-mission to test the software in a real environment. The orbit was reduced to 50 km after the spacecraft was successfully placed in orbit at 200 km around Eros, where NLR data was collected. A shape-based spherical gravity model was calculated with the shape model based on this data, and the coefficients were used as a-priori coefficients for the process of orbit determination. After the orbit was reduced to 35 km the gravity coefficients were estimated by the orbit determination process during 10 days by degree and order 10 in relation to their uncertainties.

Estimating the $\mu$ on the first part of the mission, as we have shown before, is the most important gravitational influence the spacecraft can feel at high altitudes. We have already shown, however, that the estimation could be done quite accurately for this parameter by increasing the distance to the centre of Eros, even if the convergence time increased with the distance. At this distance, radiometric data will give the inertial position as a measurement. We should also maintain that the estimation can not be done for such altitudes by ignoring the SRP and the third-body disturbance.

The focus is on estimating the coefficients during the 50 km orbit after this estimate is carried out. For that, we assume that every 2s, the Lidar and Navcam delivers data, working along with the radiometric measurements that continuously give measurements 3 hours a day. Figure 7.25a displays the results for this estimation. We can see that the higher degree coefficients are still to be estimated, although the coefficients up to degree and order 5 can be estimated quite accurately. For the next estimation step, we will use this data as *a-priori* values, which will consist of estimating all degree coefficients up to degree and order 8 during a 35 km orbit, orbiting for 10 days. In this case, as shown in Figure 7.25b, we can see that all the coefficients can be estimated. We can see, however, there are still some coefficients converging. The initial *a-priori* values for the position and velocity are initialised close to the real values, with an initial error of 10 m for the position and 1 m/s for the velocity.

With this spherical harmonics model, the estimated velocity and position are shown in figure 7.26, where we can see that for the propagation time, the position and velocity errors are very low. This is mainly due to the fact that the measurements are based on low noise. We can also observe that the model is still not perfect for estimating the position and velocity perfectly, although the estimation error is low. This may be because higher order coefficients are not included in the estimation process or the errors in the estimated forces of the disturbance are too high.

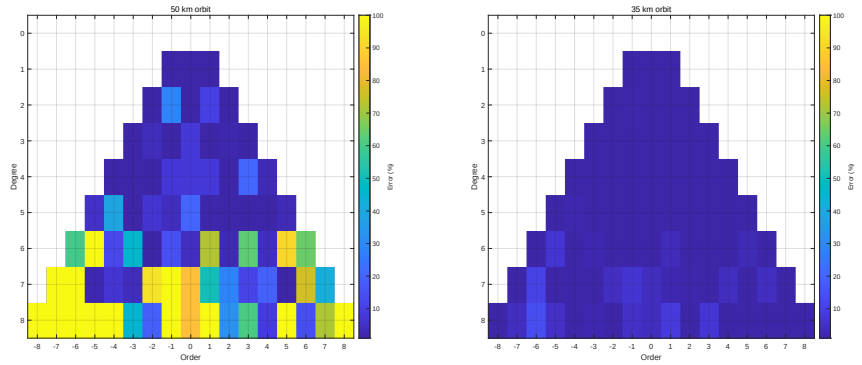


(a) 50 km altitude orbit estimation (b) 35 km altitude orbit estimation

Figure 7.25: Estimation error for the spherical harmonics coefficients estimated with a 50 km altitude orbit.

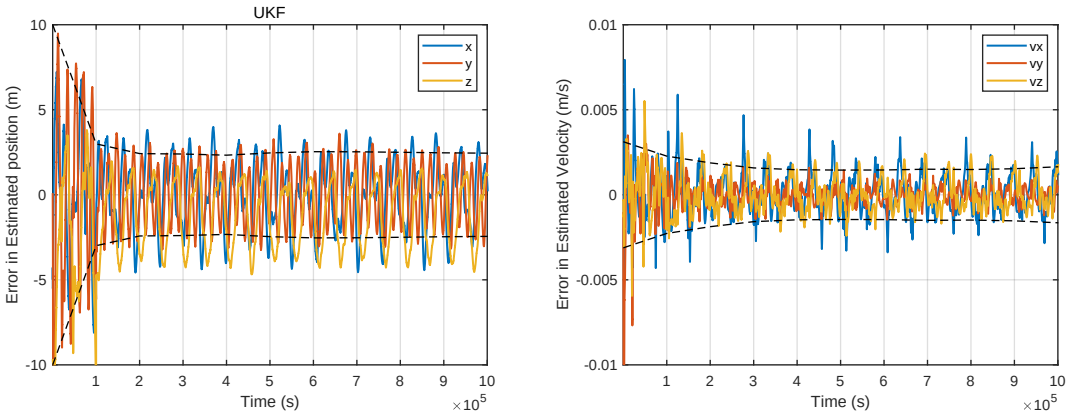


(a) Position error (b) Velocity error

Figure 7.26: Estimation error for the position and velocity with a 30 km orbit.

# 8

# Conclusions, Discussions and Recommendations

The key objectives of this study are to discuss the research questions formulated in the introduction. From these questions, several conclusions can be drawn for each question, using the results of development and simulations. Indeed these questions can not be fully answered, so certain investigations will need to be carried out to finish the work done during the study, because of the lack of time. The recommendations will then outline the remaining work to address the questions thoroughly and to broaden the scope of this work.

## 8.1 Conclusions

The software was tested under different conditions in the previous chapter, to evaluate the performances of the simulator in each of these conditions.

Since the resolution of the spherical harmonics decreases, as the distance to the asteroid increases, the high order and degree coefficients are becoming harder to estimate. The inclination also affects the estimation, due to the fact that the surface area covered by the spacecraft is larger with a high inclination, and therefore the spacecraft can feel the effect of every component of the irregular gravity field. We have attempted to remove the coefficients of first-order and degree spherical harmonics to see any improvement in the results, which worked, since the software struggled to estimate these coefficients representing the shift from the centre of gravity to the centre of reference frame, which appeared to be very small. However, removing the $J_2$ and $\mu$ had no effect on the estimation results, as they are strong effects that can be estimated below 1% error, very quickly. Nonetheless, adding the asteroid's rotational rate to the estimation procedure did not drastically reduce the performances. Finally, the software was tested with the Near mission scenario leading to an estimate of all spherical harmonics coefficients up to degree and order 8, below 10% error.

Based on the previous results and the work accomplished during this thesis, the research questions must be mentioned and answered in this section.

– ***How to increase the safety of autonomous navigation for asteroid missions?***

By attempting to measure as accurately as possible the forces and torques acting on the dynamics of the spacecraft in this kind of environment, the safety of autonomous navigation can be improved. To prevent major errors in the state prediction, any disturbance that could have an effect on the spacecraft must be included in the model. As we have shown, for instance, it is not appropriate to neglect the SRP and third-body disruption, as it causes significant errors in the $\mu$ parameter estimation. The navigation software should then be able to predict these forces and apply them to the spacecraft dynamical model. In addition, sensors should be present on the spacecraft to estimate these forces for this estimation to be performed. The accelerometer will, for instance, be used to effect the SRP force on the spacecraft during no-thrust manoeuvres.

It is not necessary to know the properties of the asteroid before the encounter to ensure better dynamic estimation. However, the collection of sensors that must be carried out by the spacecraft should be sufficient to provide prior characterisation of the asteroid during the first step of the mission, which is necessary for the rest of the estimations. Navcams are very effective sensors that have been used in the past, and will be used in future missions. They are powerful in the sense that, they can be used both for early characterisation and for accurate navigation close to the asteroid and for landings. When combined with Lidar data, a full collection of measurements can be created and more measurements can be given to the filters. The more measurements are given, the better the estimation would be as long as the information given to the filter is not redundant. However, the estimation can be conducted using only Lidar data, navcams and star-tracker, along with radiometric-measurements.

The last factor to be taken into account to improve the safety of navigation and the precision of the predictions is the gravity field of the target asteroid. It must be taken into account that, while we have used a spherical harmonics model, this gravity field model cannot be used for the last mission phase corresponding to the landing phase. The Spherical Harmonics gravity model is valid only outside the sphere of reference and often diverges close to the surface. For this reason, another solution must be explored for the last mission phase We have seen that although the polyhedron gravity field modelling is very accurate, the spherical gravity harmonics model is more than adequate to describe the field of gravity even for irregular bodies during interesting mission phases, and has the advantage of being computationally effective, which is not the case for the polyhedron model.

Consequently, three aspects must be taken into consideration to improve the safety of navigation. The sensors should provide measurements as accurately as possible, providing as much environmental information as possible, so that the filter can estimate the state and velocity with a high accuracy. The gravity field of the asteroid must be included in the estimation process, with the spherical harmonics model up and to the maximum degree and order and only before the landing phase, to reduce the errors of the estimated acceleration and thus improve the accuracy of the dynamical model. The last phase, i.e., the landing phase, must be analysed separately and a different way of estimating the coefficients of gravity must be used to prevent divergences. The last factor to be taken into account is the disturbances arising from other bodies, such as the Sun or others massive bodies in the asteroid environment.

***(a) What is the influence of an irregular gravity field on the motion of a spacecraft in the vicinity of asteroids?***

The influence of the irregular gravitational field can be seen in the dynamics of the spacecraft, with a highly irregular gravitational field, the dynamics of the spacecraft will be affected and may lead to unstable orbits. The problem in a highly irregular gravity field is that the errors introduced in the dynamics may be too strong to estimate the position and velocity of the next step. That is why we are using a spherical harmonics model to characterise Eros gravity field, to allow an estimation of the state at each time step. However, we know the farther we are from the asteroid, the less the spacecraft will be affected by irregularities and therefore by high order and degree of spherical harmonics. Consequently, we can start by estimating only the $\mu$ gravitational parameter far away from the centre of Eros, without taking into consideration the higher order and the degree of the spherical harmonics.

The same procedure can be used to estimate the value of the $J_2$ coefficients by getting closer to the surface when the $\mu$ parameter has been accurately estimated. However, in our case, the shape of Eros allowed the characterisation of all coefficients up to degree and order, but we must take into account that the gravitational field of the target asteroid may be more regular and therefore the effect of the gravitational coefficients may have too little effect to be estimated with the same estimation time. In the reverse situation, the shape may be more irregular, and therefore the effects of higher order and degree coefficients may be as strong as the effect of $J_2$, which could strongly impact the estimation of this coefficient by proceeding step-by-step. For a larger picture, if we do not know the shape of the target asteroid at all a step-by-step solution must be avoided and a simultaneous estimation of all the coefficients preferred.

***(b) What is the impact of the gravitational modelling on the navigation accuracy?***

The gravity field model has a major effect on navigation safety in such a way that if the gravity field is not correctly modelled, the acceleration acting on the spacecraft cannot be accurately determined and thus, location and velocity cannot be predicted with adequate accuracy. As we have seen before in the case of very irregular bodies such as Eros, the simple point mass gravity model, which may be appropriate for orbiting planets, is not for this type of body. For low altitude orbits, the errors in the gravity field and thus the acceleration felt by the spacecraft using this model can be up to 30% of the actual acceleration value, which is too high to consider this model. However, more refined models can be used, such as the polyhedron and spherical harmonics, which as discussed above, can be used for computational efficiency in different mission phases.

However, some aspect that needs to be discussed is the gravity resolution. In our case, we computed the differences in propagated states that could occur by using different degrees of expansion for our spherical harmonics model. We concluded that the model of spherical harmonics up to degree and order 8 was sufficient to con of these coefficients without too much error in the dynamical model . However, this degree was also chosen because the increase in the degree of expansion increases the number of coefficients to be estimated and increases the computational time. By choosing a too high degree of expansion, the computational time may be too long for the estimation process to be carried out in-real time, and the estimation time may be too long to estimate all these degrees and order coefficients, without the assurance of any improvement in the estimation of the state of the spacecraft. As previously discussed, this resolution is also dependent on the target asteroid. If the body appears to be regular in shape, it may not be necessary

to extend the spherical harmonics to a high degree, because the higher degree and order of the spherical harmonics coefficients will require a long estimation time, although they will not really affect the dynamics of the spacecraft. To reduce the computational time, a trade-off must be made on the basis of the first data obtained at the arrival of the different sensors.

**(c)** ***How can the gravity field be autonomously estimated using only on-board data and measurements?***

Using the correct set of measurement data, the field of gravity can be estimated using the spherical harmonics expansion. Measurements are used by an Unscented Kalman Filter to correct the state of the spacecraft and parameters that need to be estimated on the basis of a given analytical state transition and measurement model. The Unscented Kalman Filter is much easier to implement than the Extended Kalman Filter for a large number of parameters that need to be estimated, since no Jacobian computation and measurement matrices are required. The difference in the performances, however, has not been shown to be significant. A particle swarm optimiser is used to estimate the covariance matrix using an off-line Kalman filter prior to estimation. The Navigation Filter was evaluated during a simulated-Near Mission Scenario, where the gravitational coefficients were estimated at order and degree 8 for a 35 km orbit, based on the a-priori coefficients determined during the preceding 50 km orbit.

## 8.2 Discussion

The results we have found, although very promising, need to be put in context, and will be discussed in this section, assessing their limitations, impact and significance.

We have seen that in the case of the Near Shoemaker mission, we were able to estimate the spherical harmonic coefficients to degree and order 8 below 10 percent error, at the same time as estimating the state of the spacecraft below 10 m error for the position and 0.01 m/s error for the velocity. In the work of Miller et al. (2002), we have seen that during the Near-mission, they were able to estimate the coefficients relative to their uncertainty up to degree and order 10. We could have increased the order coefficients to this degree and even higher, but the limitation was motivated by the limited CPU we have and the time we could afford for each estimate to be made. However, this does not mean that this model is not capable of estimating higher degree and order coefficients. We just decided to limit the estimation for practical reasons.

We have decided to estimate the coefficients in the same time than the spacecraft state, and the two estimates are working in a complementary way. If the spherical harmonics model is more accurate, the estimation of the state will be more accurate in the next estimation step, which will contribute to the estimation of the coefficients, and so on. This loop is beneficial for both state and parameter estimates. This method works well and makes it possible to estimate the spherical harmonics gravity at the same time as the state vectors, which is a step further in making navigation fully autonomous, because even if we do not know the shape of the target asteroid, this estimation can still be made and allow us to predict the negative effects that the field of gravity may have on the dynamics of the spacecraft.

We have also seen that the range has a major impact on the estimation of the gravity field coefficients. For example, the spherical harmonics coefficients on a 100 km orbit, were only estimated up to order and degree 4, while reducing the altitude to a 45 km orbit, the estimation could be conducted up to degree and order 8, for the same propagation time. This is a very important drawback in the use of spherical harmonics as a model for the body's gravity field. As the resolution of the expansion of the harmonics decreases with the distance to the centre, the spacecraft should be closer to the asteroid surface to feel higher order and degree coefficients. However, if the spacecraft is too close, the spherical harmonics cannot be used any longer due to the differences in its model when entering the Brillouin sphere. The maximum order and the degree to which the spherical harmonics coefficients are to be estimated should be chosen according to the orbit altitude at which these parameters are to be estimated. However, the closer we get, the higher the perturbations will be and the more difficult it will be to estimate the state. If the degree of expansion is too important, the estimated time will be increased and the higher coefficients will not be estimated. On the contrary, if the degree of expansion is chosen to be too small, errors will be introduced in the estimation, since the perturbations that will not be taken into account by the model will interfere with the estimation process. It is therefore important to analyse and carefully choose the degree of expansion. In addition, the inclination should be chosen on the basis of the rotational dynamics of the asteroid in the order to cover the maximum surface area. It has been shown that, for our spacecraft around Eros, an inclination of 90° leads to better results in the estimation for the spherical harmonics coefficients. It is therefore important to optimise the trajectory of the spacecraft, based on the first data we get from the asteroid, to improve the estimation. If the optimisation of the orbit is not carried out the estimation process will not be ideal.

Another important aspect that needs to be discussed is the navigation sensors. For most simulations, we have chosen to use only the noisy position as a measure for the estimation process to be performed. However, this was chosen because the implementation of the range and range rate as measurements did not improve the performance of the filter. However, the last simulation was performed using the modelled sensors. We have seen that although the transition from ideal measurement to sensors still leads to accurate estimation, it affects the estimation time and the estimation of the state. This is due to the fact that we use a more complex model that outputs measurements at different rates, and sometimes no measurements are given to the filter that needs to be taken the last step without improving the results. It must be understood that the improvement of the measurement model can give different results with this estimation process and therefore this filter must be tested with different and more complex sensors models to really test the behaviour of this navigation filter in a real environment

The assumptions that we made at the beginning of the thesis must also be discussed. We assumed that the SRP was estimated earlier in the mission and therefore a small error value with the SRP was given to the estimation filter. We have seen that, ignoring the SRP in the estimation process led to divergences in the $\mu$ estimation. Therefore, if the $\mu$ could not be estimated accurately, the spherical harmonics coefficients estimation could not be conducted properly. Taking into account this disturbance, however, the $\mu$ parameter could be estimated with a maximum error of 0.2%. It would have been interesting to see if the filter could be able to estimate this force at the beginning, because we have chosen a small error for the SRP, which in reality, might not be possible. It is exactly the same process with a rotational rate. Although we have seen its effect on the estimation process, it would have been interesting to see if, along with the SRP estimate,

the estimation of coefficients would still have been possible under these conditions. In other words, by increasing the accuracy of the models, the simulated-real-world model, and the navigation filters, the actual performance of the filters can be assessed.

This thesis work can be added to previous works, such as the work of Razgus (2016), who explored the implementation of a dual quaternion method for relative asteroid navigation. It allows a precise characterization of the asteroid's gravity field and thus to decreases the errors in the acceleration model and in the state estimation. This thesis completes his extensive work on the modelling of the navigation system around an asteroid, by improving the precision of the gravity field, and hence by increasing the model and estimation accuracy. This work is one step forward in trying to make the navigation around asteroids more robust and reliable, and hence to increase the navigation safety.

## 8.3 Recommendations

For time purposes, some investigations or improvements in the models could not be carried out. However, these objectives and considerations will remain as recommendations for future work:

- This software must be evaluated in other settings, around other bodies, to determine its efficiency in different scenarios. Because the simulation of the gravity field depends on the shape of the asteroid, we should expect that this model is also suitable for other environments. However, the degree of expansion of the spherical harmonics must be tested and adjusted, if necessary, depending on the shape and density of the orbiting asteroid.
- The last phase of the mission must be investigated by testing different techniques for estimating the near-surface gravity field. Polyhedron modelling may be the solution for this estimation method, but other techniques may be envisaged to increase computational efficiency, such as Mascon-spherical modelling coupled harmonics, or the dynamic Brillouin Sphere Radius technique for computing spherical harmonics close to the surface.
- This model should be included in a full GNC system to evaluate its performance in a real mission when the manoeuvres are executed.
- Gravitational accuracy must be increased to see up to which order the model is capable of estimating the coefficients of spherical harmonics and with which accuracy. Depending on the distance, an investigation may be conducted into the limits of this estimation process in the case of Eros or other scenarios.
- The measurement model must be enhanced to include real-sensor effects such as bias and misalignment. Models of the sensors must be refined to obtain measurements that are as realistic as possible, including, for example, pointing errors or range errors due to the presence of surface features occulting the line of sight of the sensors. In this conditions, the performances of the filters must decrease.
- The image processing part should be included in the Navcam model. The landmark tracking phase must be carried out at the beginning of the mission and not

randomly generated on the surface for more realistic conditions. Simultaneous localization and mapping methods should be explored to determine its effect on the estimation.

- A different set of sensors can be used to test the efficiency of the filter under these new conditions. The sensors can only be reduced to optical navigation, which is a very promising technique. We have shown that the filter can operate with only one noisy inertial state vector measurement, so this technique needs to be investigated to see whether it is possible to reduce the number of sensors on-board without reducing the performances.

- The given constant values for this model such as the SRP and the rotational rate must be included in the navigation filter to see if it is still possible to estimate the coefficients when these constants are not given.

- The torque and force model of the spacecraft must be enhanced to provide the control forces and torques that could be used to control the attitude of the spacecraft, and to guide the sensors to the surface. This could increase the efficiency of the filter in the sense that it would keep the asteroid from being out of the sensor LOS.

# References


Binzel, R., Barucci, M., and Fulchignoni, M., (1991), "The Origins of the Asteroids", *Scientific American*, Vol. 256, pp. 66-71.

Buemi, M., Landi A., and Procopio, D.,(1999) "Autonomous Star tracker for Rosetta", *4th International ESA Conference on Guidance, Navigation and Control Systems*, ESTEC, Nordwijk, The Netherlands.

Butcher, J., (1987), *The Numerical Analysis of Ordinary Differential Equations: Runge-Kutta and General Linear Methods*, 1st edition, Wiley-Interscience, New York.

Castellini, F., Santayana, R.P., Wokes, D., and Kielbassa, S., (2014), "Optical navigation for Rosetta operations near comet Churyumov-Gerasimenko", *Advances in the Astronautical Sciences*, Vol. 150, pp. 1619-1637.

Chanut, T. G. G., Winter, O. C., Tsuchida, M., (2014), "3D stability orbits close to 433 Eros using an effective polyhedral model method", *Monthly notices of the Royal astronomical society*, Vol. 438, pp.2672–2682.

Chanut, T., Aljbaae, S., Carruba, V.,(2015), "Mascon gravitation model using a shaped polyhedral source", *Monthly Notices of the Royal Astronomical Society*, Vol. 450, pp.3742-3749.

Cheng and Andrew, (2002), "Near-earth Asteroid Rendezvous: Mission Summary", *Asteroids III*, Vol. 1, pp. 351–366.

Davies, M. E., Abalakin, V. K., Bursa, M., Lieske, J. H., Morando, B., Morrison, D., Seidelmann, P. K., Sinclair, A. T., Yallop, B., Tjuflin, Y. S., (1996), "Report of the IAU/IAG/COSPAR Working Group on Cartographic Coordinates and Rotational Elements of the Planets and Satellites: 1994 ", *Celestial Mechanics Dynamical Astronomy*, Vol. 63, Issue 2, pp.127-148.

Garmier, R., Barriot, J-P., Konopliv, A.S., Yeomans, D.K., (2002), "Modeling of the Eros gravity field as an ellipsoidal harmonic expansion from the NEAR Doppler tracking data", *Geophysical Research Letters*, Vol. 29, No. 8, pp.721–723.

Gasbarri, P., Pisculli, A., (2015), "Dynamic/control interactions between flexible orbiting space-robot during grasping, docking and post-docking manoeuvres", *Acta Astronautica*, Vol. 110, pp.225-238.

Gaskell, R.W., (2005), "Landmark navigation and target characterization in a simulated Itokawa encounter",*AAS/AIAA Astrodynamics Specialists Conference*.

Gaskell et al., (2006), "Landmark Navigation Studies and Target Characterization in the Hayabusa Encounter with Itokawa", *AIAA/AAS Astrodynamics Specialist Conference and Exhibit*, pp. 6660.

Godard et al., (2015), "Orbit Determination of Rosetta Around Comet 67P Churyumov-Gerasimenko", *Proceedings 25th International Symposium on Space Flight Dynamics – 25th ISSFD*, Munich, Germany.

Gil-Fernandez, J. and Ortega-Hernando, G., (2018), "Autonomous vision-based navigation for proximity operations around binary asteroids", *CEAS Space Journal*, Vol. 10, no. 2, pp. 287–294.

Gil-Fernandez, J., Casasco, M., Carnelli, I., Martino, P., Küppers, M. (2019). HERA autonomous Guidance, Navigation and Control experiments: enabling better asteroid science future missions., *EUCASS 2019*.

Hahn, W., (1969), *Stability of Motion*, 1st edition, Springer-Verlag, Berlin.

Harris, A.W. and Burns, J.A., (1979), "Asteroid rotation: I. Tabulation and analysis of rates, pole positions and shapes", *Icarus*, Vol. 40, Issue 1, pp. 115-144.

Hashimoto, T., Kubota, T., Kawaguchi, T., Uo, J. Shirakawa, M. Kominato, K. Morita and Hiroshi, T., (2010), "Vision-based guidance, navigation, and control of Hayabusa spacecraft - Lessons learned from real operation", *IFAC Proceedings*, Vol. 18., pp. 259-264.

Holsapple, K., (2001), "Equilibrium configurations of solid cohesionless Bodies", *Icarus*, Vol. 154, pp. 432-448.

Hughes, D., (1983), "The Relationship between the sizes of Asteroids and their Spin Frequencies", *Journal of the British Astronomical Association*, Vol. 94., pp. 12-17.

Ivantsov, Anatoliy, (2008), "Asteroid mass determination at Nikolaev Observatory", *Planetary and Space Science*, Vol. 56, Issue 14, pp. 1857-1861.

Jatoth, R.K., Kumar, T.K., (2009), "Particle Swarm optimization Based Tuning of Extended Kalman Filter for Manoeuvring Target Tracking," *Mathematics and Computers In Science And Engineering archive Proceedings of the 8th WSEAS international conference on Signal processing, robotics and automation*.

Jean, I., Ng, A., and Misra, A.K., (2019), "Impact of Solar radiation pressure modeling on orbital dynamics in the vicinity of binary asteroids",*Acta Astronautica*, Vol. 165, pp. 167-183.

Julier, S., Uhlmann, J.K., (2004), "Unscented Filtering and Nonlinear Estimation", *Proceedings of the IEEE*, Vol. 92, pp. 401-422.

Kim, S. G., Crassidis, J. L., Cheng, Y., Fosbury, A. M., and Junkins, J.L., (2017), "Kalman Filtering for Relative Spacecraft Attitude and Position Estimation", *Journal of Guidance, Control, and Dynamics*, Vol. 30, No. 1, pp. 133–143.

Konopliv et al., (2014), "The Vesta gravity field, spin pole and rotation period, landmark positions, and ephemeris from the Dawn tracking and optical data", *Icarus*, Vol. 240, pp.103-117.

Hashimoto, T., Kubota, T., Kawaguchi, T., Sawai, S. Uo, M., Ninomiya, K., and Kenichi, B., (2010), "An autonomous navigation and guidance system for MUSES-C asteroid landing, *Acta Astronautica*, Vol. 5., pp. 125-131.

Markley, F.L., and Crassidis, J.L., (2013), *Fundamentals of Spacecraft Attitude Determination and Control*, Springer, Vol. 2.

Mathews, J.H., Fink, K.D., (1999), *Numerical Methods Using Matlab.*, Prentice-Hall, 3th edition.

Mcmahon, J., Scheeres, D.J., Hesar, S., Farnocchia, D., Chesley, S., and Lauretta, D., (2018), "The OSIRIS-REx Radio Science Experiment at Bennu", *Space Science Reviews*, Vol. 214., pp. 1-41.

Miller, J., Konopliv, A.S., Antreasian, P., Bordi, J.J., Chesley, S., Helfrich, C.E., Owen, W.M., Wang, T.C., Williams, B., Yeomans, D., and Scheeres, D.J., (2002), "Determination of Shape, Gravity, and Rotational State of Asteroid 433 Eros", *Icarus*, Vol. 155, pp.3-17.

Mooij, E., Noomen, R., (2013), "Autonomous navigation at asteroids", *60th Astronautical Congress*, IAC 2009, pp.1519-1530.

Mooij, E., (2019), *Re-entry Systems*, (AE4870B Lecture Notes), Delft University of Technology, Faculty of Aerospace Engineering.

Montenbruck, O. and Gill, E., (2001), *Satellite Orbits: Models, Methods and Applications*, Springer Verlag, Hei-delberg.

Moreno Villa, V.M, (2018), *Spacecraft Navigation Around Small Bodies in Early-characterisation Phases*, TU Delft Msc thesis, Tu Delft repository, Netherlands.

Mukundan, R., (1990), "A procedure for the estimation of Solar radiation torque components considering multiple shadow regions and surface reflectance properties", *Math Comput. Modelling*, Vol. 13, No. 4, pp. I-6.

Munoz, P., Budnik, F., Godard, B., Morley, T., Companys, V., Herfort, U., and Casas, C., (2012), "Preparations and strategy for navigation during Rosetta Comet phase", *Proceedings 23rd International Symposium on Space Flight Dynamics*, Pasadena, USA.

Osada, R., Funkhouser, T., Chazelle, B., Dobkin, D., "Shape distributions",(2002), *ACM Transactions on Graphics*, Vol. 21, Issue 4, pp. 807-832.

Owen, W. M., T. Wang, A. Harch, M. Bell, and C. Peterson, (2002), "NEAR optical navigation at Eros", *Advances in the Astronautical Sciences*, Vol. 109, pp. 1075–1087.

Pravec, P., and Harris, A.W., (2000), "Fast and Slow Rotation of Asteroids", *Icarus*, Vol. 148, Issue 1, pp. 12-20.

Razgus, B., (2016), "Relative Navigation in Asteroid Missions Dual Quaternion Approach", TU Delft Msc Thesis, TU Delft Repository, Netherlands.

Rapp, K., (2004), "Nonlinear estimation and control in the iron ore pelletizing process: An application and analysis of the Extended Kalman Filter", Norwegian University of Science and Technology.

Richner, M., Gebauer, G., and Leissle, T., (2003), "Coordinate Systems for Rosetta", Technical report, Vol. 6d.

Scheeres, D.J., 1999, "Satellite Dynamics about small bodies: Averaged Solar Radiation Pressure Effects", *Journal of the Astronautical Sciences*, Vol. 47, pp. 25–46.

Shestopalov, D., Golubeva, L., (2020), *Surface composition of asteroids by their reflectance spectra*, LAP Lambert Academic Publishing.

Shuang, L., Hutao, C., Pingyuan, C., (2005), "Autonomous optical navigation for landing on asteroids", *Aircraft Engineering and Aerospace Technology*, Vol. 77, Issue 4, pp. 317-323.

Shuang, L., (2008), "Landmark tracking based autonomous navigation schemes for landing spacecraft on asteroids", *Acta Astronautica*, Vol. 69, pp.391-403

Shuang, L., Lu, R., Zhang, L. and Peng, Y., (2013), "Image Processing Algorithms For Deep-Space Autonomous Optical Navigation", *Journal of Navigation*, Vol. 69, Issue 4, pp. 828-844.

Souchay, J., Kinoshi, H., Nakai, H., Roux, S., (2003), "A precise modeling of Eros 433 rotation", *Icarus* Vol. 166, Issue 2, pp. 285-296.

Stramaccioni, D., (2004), "The Rosetta Propulsion System", *4th International Spacecraft Propulsion Conference*, Italy, pp.3.1.

Tapley, B.D., Schutz, B.E., Born, G.H., (2004), *Statistical Orbit Determination*, Elsevier Academic Press, 1st edition.

Vasile, M., Romano, M., Marcello, and Trainiti, F., (2000), "An Optical Based Strategy for Deep Space Autonomous Navigation", *4th ESA International Conference on Spacecraft Guidance Navigation and Control Systems*, pp.549.

Verdant, M. and Schwehm, G.H., (1998), "The International Rosetta Mission", *ESA Bulletin*, ESA, Vol. 93, pp.39-50.

Virgili, B., Lemmens, S., and Krag, H., (2014), "Investigation on Envisat Attitude Motion" ,*e.Deorbit Workshop*, European Space Agency, The Netherlands.

Wakker, K., (2015), *Fundamentals of Astrodynamics*, Institutional Repository, Delft University of Technology.

Wan, E.A., and Van Der Merwe R., (2000), "The Unscented Kalman Filter for Nonlinear Estimation", *Adaptive Systems for Signal Processing, Communications, and Control Symposium 2000*, pp.153-158.

Welch, G., and Bishop, G., (2006), *An Introduction to the Kalman Filter*, University of North Carolina, Department of Computer Science.

Werner, R.A., and Scheeres, D.J., (1996), " Exterior gravitation of a polyhedron derived and compared with harmonic and mascon gravitation representations of asteroid 4769 Castalia", *Celestial Mechanics and Dynamical Astronomy*, Vol. 65, pp. 313–344.

Williams, B., (2002), "Technical challenges and results for navigation of NEAR Shoemaker", *Johns Hopkins APL Technical Digest*, Vol. 23, Issue 1, pp. 34–45.

Williams et al., (2018), "OSIRIS-REx Flight Dynamics and Navigation Design", *Space Science Reviews*, Vol. 214, pp. 69.

Yeomans et al., (1998), "Estimating the Mass of Asteroid 253 Mathilde from Tracking Data During the NEAR Flyby", *Science*, Vol. 278, pp. 2106-2109.

Yeomans et al., (2000), "Radio Science Results During the NEAR-Shoemaker Spacecraft Rendezvous with Eros", *Science*, Vol. 289, pp.2085-2088.

Yoshikawa et al., (2006), "Astrodynamics Science About Itokawa, Gravity and Ephemeris", *AIAA/AAS Astrodynamics Specialist Conference and Exhibit*, pp. 6658.

Zarchan, P., (2009), *Fundamentals of Kalman Filtering: A Practical Approach*, American Institute of Aeronautics and Astronautics.

# A

# EKF Equations

## A.1 Point mass Gravity

The calculation for the point mass gravity acceleration was made using the main formula:

$$||\mathbf{F}_g|| = -\frac{\mu}{d^2} \tag{A.1}$$

with d the distance to the centre of Eros, $\mu$ its main gravitationnal parameter. The state space equation can be written as:

$$\begin{pmatrix} \dot{\mathbf{x}} \\ \ddot{\mathbf{x}} \\ \dot{\mu} \end{pmatrix} = F \begin{pmatrix} \mathbf{x} \\ \dot{\mathbf{x}} \\ \mu \end{pmatrix} + \begin{pmatrix} \boldsymbol{\nu}_1 \\ \boldsymbol{\nu}_2 \\ \nu_3 \end{pmatrix} \tag{A.2}$$

With $\nu_1, \nu_2, \nu_3$ the values of the process noise.

The jacobian matrix, for this scenario can be witten as:

$$\mathbf{F} = \begin{bmatrix} \mathbf{0}_{3\times3} & \mathbf{I}_{3\times3} & \mathbf{0}_{3\times1} \\ (\frac{\partial \ddot{\boldsymbol{x}}}{\partial \boldsymbol{x}})_{3\times3} & \mathbf{0}_{3\times3} & \mathbf{0}_{3\times1} \\ \mathbf{0}_{1\times3} & \mathbf{0}_{1\times3} & 0 \end{bmatrix} \tag{A.3}$$

And the process noise matrix is:

$$\mathbf{Q} = E[\nu_k \nu_j^T] = \begin{bmatrix} \mathbf{I}_{3\times3} * \nu_1^2 & \mathbf{0}_{3\times3} & \mathbf{0}_{3\times1} \\ \mathbf{0}_{3\times3} & \mathbf{I}_{3\times3} * \nu_2^2 & \mathbf{0}_{3\times1} \\ \mathbf{0}_{1\times3} & \mathbf{0}_{1\times3} & \nu_3^2 \end{bmatrix} \tag{A.4}$$

For the first scenario, the measurements are the real state with added Gaussian noise, therefore the measurement matrix is the following:

$$\mathbf{H} = \begin{bmatrix} 1 & 0 & 0 & 0 & 0 & 0 \\ 0 & 1 & 0 & 0 & 0 & 0 \\ 0 & 0 & 1 & 0 & 0 & 0 \\ 0 & 0 & 0 & 1 & 0 & 0 \\ 0 & 0 & 0 & 0 & 1 & 0 \\ 0 & 0 & 0 & 0 & 0 & 1 \end{bmatrix} \tag{A.5}$$

If $\mu_1$,$\mu_2$,$\mu_3$ are the measurement noise acting on the position, velocity and acceleration respectively, the noise measurement matrix can be written as:

$$\mathbf{R} = E[\sigma_k \sigma_j^T] = \begin{bmatrix} \mathbf{I}_{3\times3} * \sigma_1^2 & \mathbf{0}_{3\times3} & \mathbf{0}_{3\times1} \\ \mathbf{0}_{3\times3} & \mathbf{I}_{3\times3} * \sigma_2^2 & \mathbf{0}_{3\times1} \\ \mathbf{0}_{1\times3} & \mathbf{0}_{1\times3} & \sigma_3^2 \end{bmatrix} \tag{A.6}$$

The value of the **Q** matrix is given after optimisation by the PSO. The values of the **R** matrix are depending on the noise values chosen during the simulations. For example, if we chose the case where $x_0$=[250000 0 0] m, when choosing $\sigma_1 = \sigma_p$=1 km where only the noisy position is given as a measurement, the matrices are reduced to:

$$\mathbf{H} = \begin{bmatrix} 1 & 0 & 0 & 0 & 0 & 0 \\ 0 & 1 & 0 & 0 & 0 & 0 \\ 0 & 0 & 1 & 0 & 0 & 0 \end{bmatrix} \tag{A.7}$$

$$\mathbf{R} = E[\sigma_k \sigma_j^T] = \begin{bmatrix} \sigma_p^2 & 0 & 0 \\ 0 & \sigma_p^2 & 0 \\ 0 & 0 & \sigma_p^2 \end{bmatrix} \tag{A.8}$$

and the process covariance matrix after optimisation is given by:

$$\mathbf{Q} = \begin{bmatrix} \mathbf{I}_{3\times3} * 1e-14 & \mathbf{0}_{3\times3} & \mathbf{0}_{3\times1} \\ \mathbf{0}_{3\times3} & \mathbf{I}_{3\times3} * 1e-12 & \mathbf{0}_{3\times3} \\ \mathbf{0}_{3\times3} & \mathbf{0}_{3\times3} & 1e-18 \end{bmatrix} \tag{A.9}$$

## A.2 $J_2$ perturbation

The state-space model that has been used in the Kalman Filter when adding $J_2$ and the rotational rate to the model is the following:

$$\begin{pmatrix} \dot{\mathbf{x}} \\ \dot{\mathbf{v}} \\ \dot{\mathbf{w}} \\ \dot{\mu} \\ \dot{J}_2 \end{pmatrix} = \begin{bmatrix} \mathbf{0}_{3\times3} & \mathbf{I}_{3\times3} & \mathbf{0}_{3\times3} & \mathbf{0}_{3\times1} & \mathbf{0}_{3\times1} \\ \left(\frac{\partial \mathbf{F}}{\partial \mathbf{x}}\right)_{3\times3} & \left(\frac{\partial \mathbf{F}}{\partial \mathbf{v}}\right)_{3\times3} & \left(\frac{\partial \mathbf{F}}{\partial \mathbf{w}}\right)_{3\times3} & \left(\frac{\partial \mathbf{F}}{\partial \boldsymbol{\mu}}\right)_{3\times1} & \left(\frac{\partial \mathbf{F}}{\partial \mathbf{J_2}}\right)_{3\times1} \\ \mathbf{0}_{3\times3} & \mathbf{0}_{3\times3} & \mathbf{0}_{3\times3} & \mathbf{0}_{3\times1} & \mathbf{0}_{3\times1} \\ \mathbf{0}_{1\times3} & \mathbf{0}_{1\times3} & \mathbf{0}_{1\times3} & \mathbf{0}_{1\times1} & \mathbf{0}_{1\times1} \\ \mathbf{0}_{1\times3} & \mathbf{0}_{1\times3} & \mathbf{0}_{1\times3} & \mathbf{0}_{1\times1} & \mathbf{0}_{1\times1} \end{bmatrix} \begin{pmatrix} \mathbf{x} \\ \mathbf{v} \\ \mathbf{w} \\ \mu \\ J_2 \end{pmatrix} + \begin{pmatrix} \boldsymbol{\nu}_1 \\ \boldsymbol{\nu}_2 \\ \boldsymbol{\nu}_3 \\ \nu_4 \\ \nu_5 \end{pmatrix} \tag{A.10}$$

with $\mathbf{x}$ the position vector, $\mathbf{x}$ the velocity, $\mathbf{w}$ the rotation rate of the asteroid, $\mu$ the gravitational parameter and $J_2$ the perturbation due to the $C_{2,0}$ harmonic coefficient. the $\nu$ coefficients are corresponding to the process noise. The measurement equation when taking into account only the position noise for the Kalman filter is the following:

$$\mathbf{z}_k = \begin{bmatrix} \mathbf{I}_{3\times3} & \mathbf{0}_{3\times3} & \mathbf{0}_{3\times3} & \mathbf{0}_{3\times1} & \mathbf{0}_{3\times1} \end{bmatrix} \begin{pmatrix} \mathbf{x} \\ \mathbf{v} \\ \mathbf{w} \\ \mu \\ J_2 \end{pmatrix} + \begin{pmatrix} \sigma_p \\ \sigma_p \\ \sigma_p \end{pmatrix} \tag{A.11}$$

with $\sigma_p$ the measurement noise acting on the position.

The acceleration due to $J_2$ in spherical coordinates is the following:

$$a_{J_2,r} = 3\mu J_2 R_e^2 r^{-4}(-\frac{1}{2} + \frac{3}{2}\sin^2\delta) \tag{A.12}$$

$$a_{J_2,\delta} = -\mu J_2 R_e^2 r^{-4}(3\sin\delta\cos\delta) \tag{A.13}$$

$$a_{J_2,\lambda} = 0 \tag{A.14}$$

which can be transformed into Cartesian coordinates:

$$a_{J_2} = -\frac{3}{2}\mu J_2 \frac{R_E^2}{r^5} \begin{pmatrix} (1 - 5\frac{z^2}{r^2})x \\ (1 - 5\frac{z^2}{r^2})y \\ (3 - 5\frac{z^2}{r^2})z \end{pmatrix} \tag{A.15}$$

Taking into account the rotation of the asteroid, new terms have to be included in the expression of the acceleration, which is, in Cartesian coordinates:

$$\mathbf{a} = -\frac{GM}{\mathbf{r}^3}\mathbf{r} - 2\mathbf{w}\times\mathbf{v} - \mathbf{w}\times\mathbf{w}\times\mathbf{r} - \mathbf{a}_{J_2} \tag{A.16}$$

Therefore, the partial derivatives of the Jacobian matrix are the following:

$$\frac{\partial F_x}{\partial x} = w_y^2 - \frac{mu}{r^3} + w_z^2 + \frac{3\mu x^2}{r^5} + \frac{\partial a_{J_2,x}}{\partial x} \tag{A.17}$$

$$\frac{\partial F_x}{\partial y} = \frac{3\mu xy}{r^5} - w_x w_y + \frac{\partial a_{J_2,x}}{\partial y} \tag{A.18}$$

$$\frac{\partial F_x}{\partial z} = \frac{3\mu xy}{r^5} - w_x w_z + \frac{\partial a_{J_2,x}}{\partial z} \tag{A.19}$$

$$\frac{\partial F_y}{\partial x} = \frac{3\mu xy}{r^5} - w_x w_y + \frac{\partial a_{J_2,y}}{\partial x} \tag{A.20}$$

$$\frac{\partial F_y}{\partial x} = w_x^2 - \frac{mu}{r^3} + w_z^2 + \frac{3\mu y^2}{r^5} + \frac{\partial a_{J_2,y}}{\partial y} \tag{A.21}$$

$$\frac{\partial F_y}{\partial z} = \frac{3\mu yz}{r^5} - w_y w_z + \frac{\partial a_{J_2,y}}{\partial z} \tag{A.22}$$

$$\frac{\partial F_z}{\partial x} = \frac{3\mu xz}{r^5} - w_x w_z + \frac{\partial a_{J_2,z}}{\partial x} \tag{A.23}$$

$$\frac{\partial F_z}{\partial z} = \frac{3\mu yz}{r^5} - w_y w_z + \frac{\partial a_{J_2,z}}{\partial y} \tag{A.24}$$

$$\frac{\partial F_z}{\partial z} = w_x^2 - \frac{mu}{r^3} + w_y^2 + \frac{3\mu z^2}{r^5} + \frac{\partial a_{J_2,z}}{\partial z} \tag{A.25}$$

(A.26)

$$\frac{\boldsymbol{\partial}\mathbf{F}}{\boldsymbol{\partial}\mathbf{V}} = \begin{bmatrix} 0 & 2w_z & -2w_y \\ -2w_z & 0 & 2w_x \\ 2w_y & -2w_x & 0 \end{bmatrix} \tag{A.27}$$

$$\frac{\boldsymbol{\partial}\mathbf{F}}{\boldsymbol{\partial}\mathbf{w}} = \begin{bmatrix} -w_y y - w_z z & 2w_y x - 2V_z - w_x y & 2V_y + 2w_z x - w_x z \\ 2V_z - w_y x + 2w_x y & -w_x x - w_z z & 2w_z y - 2v_x - w_y z \\ 2w_x z - w_z x - 2V_y & 2V_z - w_z y + 2w_y z & -w_x x - w_y y \end{bmatrix} \tag{A.28}$$

$$\frac{\boldsymbol{\partial}\mathbf{F}}{\boldsymbol{\partial}\mathbf{J_2}} = -\frac{3}{2}\mu\frac{R_e^2}{r^5}\begin{bmatrix} (1-5\frac{z^2}{r^2})x \\ (1-5\frac{z^2}{r^2})y \\ (3-5\frac{z^2}{r^2})z \end{bmatrix} \tag{A.29}$$

$$\frac{\boldsymbol{\partial}\mathbf{F}}{\boldsymbol{\partial}\boldsymbol{\mu}} = -\frac{\vec{r}}{r^3} - \frac{3}{2}J_2\frac{R_e^2}{r^5}\begin{bmatrix} (1-5\frac{z^2}{r^2})x \\ (1-5\frac{z^2}{r^2})y \\ (3-5\frac{z^2}{r^2})z \end{bmatrix} \tag{A.30}$$

Again, the $\mathbf{R}$ and $\mathbf{Q}$ matrices are determines each scenario, depending on the on the initial conditions and the PSO optimisation for the $\mathbf{Q}$ matrix. For the case $x_0$ =[100000 0 0] m, and a noisy position measurement with $\sigma_p$=1 km, the covariance matrix after optimisation is:

$$\mathbf{Q} = \begin{bmatrix} \mathbf{I}_{3\times3} * 1e-13 & \mathbf{0}_{3\times3} & \mathbf{0}_{3\times3} & \mathbf{0}_{3\times1} & \mathbf{0}_{3\times1} \\ \mathbf{0}_{3\times3} & \mathbf{I}_{3\times3} * 1e-10 & \mathbf{0}_{3\times3} & \mathbf{0}_{3\times1} & \mathbf{0}_{3\times1} \\ \mathbf{0}_{3\times3} & \mathbf{0}_{3\times3} & \mathbf{I}_{3\times3} * 1e-12 & \mathbf{0}_{3\times1} & \mathbf{0}_{3\times1} \\ \mathbf{0}_{1\times3} & \mathbf{0}_{1\times3} & \mathbf{0}_{1\times3} & 1e-16 & 0 \\ \mathbf{0}_{1\times3} & \mathbf{0}_{1\times3} & \mathbf{0}_{1\times3} & 0 & 1e-18 \end{bmatrix} \tag{A.31}$$

## A.3 Spherical harmonics coefficients model

The state-space model that has been used in the Kalman Filter when adding all the spherical harmonics coefficients is the following:

$$\begin{pmatrix} \dot{\mathbf{x}} \\ \dot{\mathbf{v}} \\ \dot{\mathbf{w}} \\ \dot{\mu} \\ \dot{\mathbf{c}}_{\mathbf{ij}} \\ \dot{\mathbf{s}}_{\mathbf{ij}} \end{pmatrix} = \begin{bmatrix} \mathbf{0}_{3\times3} & \mathbf{I}_{3\times3} & \mathbf{0}_{3\times3} & \mathbf{0}_{3\times1} & \mathbf{0}_{3\times m} & \mathbf{0}_{3\times n} \\ (\frac{\partial \mathbf{F}}{\partial \mathbf{x}})_{3\times3} & (\frac{\partial \mathbf{F}}{\partial \mathbf{v}})_{3\times3} & (\frac{\partial \mathbf{F}}{\partial \mathbf{w}})_{3\times3} & (\frac{\partial \mathbf{F}}{\partial \boldsymbol{\mu}})_{3\times1} & (\frac{\partial \mathbf{F}}{\partial \mathbf{c}_{\mathbf{ij}}})_{3\times m} & (\frac{\partial \mathbf{F}}{\partial \mathbf{s}_{\mathbf{ij}}})_{3\times n} \\ \mathbf{0}_{3\times3} & \mathbf{0}_{3\times3} & \mathbf{0}_{3\times3} & \mathbf{0}_{3\times1} & \mathbf{0}_{3\times m} & \mathbf{0}_{3\times n} \\ \mathbf{0}_{1\times3} & \mathbf{0}_{1\times3} & \mathbf{0}_{1\times3} & \mathbf{0}_{1\times1} & \mathbf{0}_{1\times m} & \mathbf{0}_{1\times n} \\ \mathbf{0}_{1\times3} & \mathbf{0}_{1\times3} & \mathbf{0}_{1\times3} & \mathbf{0}_{1\times1} & \mathbf{0}_{1\times m} & \mathbf{0}_{1\times n} \end{bmatrix} \begin{pmatrix} \mathbf{x} \\ \mathbf{v} \\ \mathbf{w} \\ \mu \\ \mathbf{c}_{\mathbf{ij}} \\ \mathbf{s}_{\mathbf{ij}} \end{pmatrix} + \begin{pmatrix} \boldsymbol{\nu}_1 \\ \boldsymbol{\nu}_2 \\ \boldsymbol{\nu}_3 \\ \nu_4 \\ \boldsymbol{\nu}_5 \\ \boldsymbol{\nu}_6 \end{pmatrix} \tag{A.32}$$

with $\mathbf{c}_{\mathbf{ij}}$ and $\mathbf{s}_{\mathbf{ij}}$ vectors containing the spherical harmonics coefficients, and $m$ and $n$ being the size of these vectors, respectively. The measurement equation becoming:

$$\mathbf{z}_k = \begin{bmatrix} \mathbf{I}_{3\times3} & \mathbf{0}_{3\times3} & \mathbf{0}_{3\times3} & \mathbf{0}_{3\times1} & \mathbf{0}_{3\times m} & \mathbf{0}_{3\times n} \end{bmatrix} \begin{pmatrix} \mathbf{x} \\ \mathbf{v} \\ \mathbf{w} \\ \mu \\ \mathbf{c}_{\mathbf{ij}} \\ \mathbf{s}_{\mathbf{ij}} \end{pmatrix} + \begin{pmatrix} \sigma_p \\ \sigma_p \\ \sigma_p \end{pmatrix} \tag{A.33}$$

with $\sigma_p$ the measurement noise acting on the position. Increasing the order and degree of expansions, the size of the Jacobian matrix increases and that is why we will prefer the UKF over the EKF for high degree of expansions.

On the same way than the last models, for the case $x_0$ =[25000 0 0] m, and a noisy position measurement with $\sigma_p$=1 km, the covariance matrix after manual optimisation is:

$$\mathbf{Q} = \begin{bmatrix} \mathbf{I}_{3\times3}*1e{-}13 & \mathbf{0}_{3\times3} & \mathbf{0}_{3\times3} & \mathbf{0}_{3\times1} & \mathbf{0}_{3} & \mathbf{0}_{3\times n} \\ \mathbf{0}_{3\times3} & \mathbf{I}_{3\times3}*1e{-}10 & \mathbf{0}_{3\times3} & \mathbf{0}_{3\times1} & \mathbf{0}_{3\times m} & \mathbf{0}_{3\times n} \\ \mathbf{0}_{3\times3} & \mathbf{0}_{3\times3} & \mathbf{I}_{3\times3}*1e{-}12 & \mathbf{0}_{3\times1} & \mathbf{0}_{3} & \mathbf{0}_{3\times n} \\ \mathbf{0}_{1\times3} & \mathbf{0}_{1\times3} & \mathbf{0}_{1\times3} & 1e{-}16 & \mathbf{0}_{1\times m} & \mathbf{0}_{1\times n} \\ \mathbf{0}_{m\times3} & \mathbf{0}_{m\times3} & \mathbf{0}_{m\times3} & \mathbf{0}_{m\times1} & \mathbf{I}_{m\times m}*1e{-}18 & \mathbf{0}_{m\times n} \\ \mathbf{0}_{n\times3} & \mathbf{0}_{n\times3} & \mathbf{0}_{n\times3} & \mathbf{0}_{n\times1} & \mathbf{0}_{n\times m} & \mathbf{I}_{n\times n}*1e{-}18 \end{bmatrix} \tag{A.34}$$

# B

# Spherical harmonics coefficients

The spherical harmonics coefficients of the Near-Shomaker mission up to degree and order 15, from the NLR data, are shown in Table B.1

Table B.1: Spherical harmonics coefficients of 433 Eros up to degree and order 15

| m | n | $C_{ij}$ | $S_{ij}$ |
|---|---|---|---|
| 0 | 0 | 1.000000000000e0 | 0.000000000000e0 |
| 1 | 0 | 1.175785831520e-03 | 0.000000000000e0 |
| 1 | 1 | -3.484427594460e-04 | 8.766452698130e-05 |
| 2 | 0 | -5.285148878740e-02 | 0.000000000000e2 |
| 2 | 1 | 1.021293512930e-04 | 8.314827416250e-02 |
| 2 | 2 | 1.171641181310e-05 | -2.819769459150e-02 |
| 3 | 0 | -1.746658679040e-03 | 0.000000000000e5 |
| 3 | 1 | 4.086789748400e-03 | -8.401928754980e-04 |
| 3 | 2 | 3.400820184730e-03 | -1.049252521580e-02 |
| 3 | 3 | 2.127432677370e-03 | -1.221642051680e-02 |
| 4 | 0 | 1.307711276510e-02 | 0.000000000000e9 |
| 4 | 1 | -1.449369221770e-04 | -3.130233427200e-04 |
| 4 | 2 | 1.647971980510e-04 | -1.946510011750e-04 |
| 4 | 3 | -1.764730392110e-02 | 1.769372863880e-02 |
| 4 | 4 | 4.623965128100e-03 | -9.118275274890e-03 |
| 5 | 0 | 8.040269731590e-04 | 0.000000000000e14 |
| 5 | 1 | -2.791765238870e-03 | 3.601526439980e-03 |
| 5 | 2 | -1.230910225660e-03 | 5.901588590910e-04 |
| 5 | 3 | -1.003790649660e-03 | -7.741235325160e-04 |
| 5 | 4 | 4.497119857680e-04 | -1.034639930470e-02 |
| 5 | 5 | 4.645819165710e-03 | -5.986302199180e-03 |
| 6 | 0 | -4.958280336910e-03 | 0.000000000000e20 |
| 6 | 1 | -5.848388650290e-05 | -5.656243124620e-03 |
| 6 | 2 | -8.779840037550e-05 | 1.798612884550e-03 |
| 6 | 3 | 6.600756525270e-03 | -5.628527194580e-04 |
| 6 | 4 | -1.188912547480e-03 | -1.202848311210e-04 |
| 6 | 5 | 2.893725631600e-04 | 5.187143981030e-03 |
| 6 | 6 | 1.860196354340e-04 | -1.562296163960e-03 |
| 7 | 0 | -3.923399201210e-04 | 0.000000000000e27 |
| 7 | 1 | 1.811938547760e-03 | 4.075777475970e-04 |
| 7 | 2 | 5.261744188700e-04 | 3.843931902200e-03 |
| 7 | 3 | 4.969228567990e-04 | 2.035935441050e-03 |
| 7 | 4 | -2.347349608900e-04 | 1.502211084770e-04 |
| 7 | 5 | -2.476609205240e-03 | -4.499749592270e-04 |
| 7 | 6 | -1.458303912990e-03 | -6.790061431970e-03 |
| 7 | 7 | -3.417036641460e-04 | -2.244364637360e-03 |
| 8 | 0 | 2.332698296190e-03 | 0.000000000000e35 |
| 8 | 1 | 1.176328666590e-04 | 3.886108808310e-04 |
| 8 | 2 | 3.362497962950e-05 | 3.491867096780e-05 |
| 8 | 3 | -3.122792657720e-03 | -2.236538379940e-03 |
| 8 | 4 | 3.431369303920e-04 | 4.701611646030e-06 |
| 8 | 5 | -2.243887071000e-04 | -5.127049850290e-04 |
| 8 | 6 | -7.063776582180e-05 | 7.874768865870e-05 |
| 8 | 7 | 2.686346867920e-03 | 2.381956825870e-03 |
| 8 | 8 | -4.162893880770e-04 | 1.330995240810e-03 |
| 9 | 0 | 2.083755917150e-04 | 0.000000000000e44 |
| 9 | 1 | -1.178840644000e-03 | -9.789857034040e-04 |
| 9 | 2 | -2.566713654180e-04 | -1.426858610010e-04 |
| 9 | 3 | -2.722648598350e-04 | 2.435952047480e-04 |

| m | n | $C_{ij}$ | $S_{ij}$ |
|---|---|---|---|
| 9 | 4 | 1.209458385260e-04 | 2.551528527300e-03 |
| 9 | 5 | 1.442991842250e-03 | 1.032029657740e-03 |
| 9 | 6 | 7.053099613340e-04 | 9.283364693910e-05 |
| 9 | 7 | 2.131043153390e-04 | -2.054462267160e-04 |
| 9 | 8 | -2.107677526960e-04 | -3.722311837610e-03 |
| 9 | 9 | -1.918873227880e-03 | -9.675531421480e-04 |
| 10 | 0 | -1.248967639670e-03 | 0.000000000000e54 |
| 10 | 1 | -1.160925394350e-04 | 1.264722906180e-03 |
| 10 | 2 | -7.213596367630e-06 | 1.993112878460e-04 |
| 10 | 3 | 1.685644566410e-03 | 3.359059776390e-04 |
| 10 | 4 | -8.994391355250e-05 | -8.480033301550e-05 |
| 10 | 5 | 1.654276532790e-04 | -1.197818966110e-03 |
| 10 | 6 | 1.014086290020e-05 | -7.489964576750e-04 |
| 10 | 7 | -1.483105545530e-03 | -3.676819780660e-04 |
| 10 | 8 | 5.471732160300e-05 | 1.743637426720e-04 |
| 10 | 9 | -2.489579760670e-04 | 1.728715263910e-03 |
| 10 | 10 | 1.741299162170e-05 | 1.940078250460e-03 |
| 11 | 0 | -1.190283726000e-04 | 0.000000000000e65 |
| 11 | 1 | 7.760862570840e-04 | -1.364432003100e-04 |
| 11 | 2 | 1.388126009180e-04 | -1.285874753440e-03 |
| 11 | 3 | 1.614103760450e-04 | -6.192102507220e-04 |
| 11 | 4 | -6.351910587980e-05 | -1.185901948620e-04 |
| 11 | 5 | -8.899570169650e-04 | 1.247571451850e-04 |
| 11 | 6 | -3.845559889400e-04 | 1.466165690390e-03 |
| 11 | 7 | -1.434581493120e-04 | 6.444114454580e-04 |
| 11 | 8 | 1.133263943250e-04 | 1.381854523050e-04 |
| 11 | 9 | 1.079663667450e-03 | -8.158184226540e-05 |
| 11 | 10 | 5.484046400350e-04 | -1.775104869060e-03 |
| 11 | 11 | 1.240210000940e-04 | -8.301376620890e-04 |
| 12 | 0 | 7.256931959170e-04 | 0.000000000000e77 |
| 12 | 1 | 9.643829496850e-05 | -2.115488306640e-04 |
| 12 | 2 | -3.341237746430e-06 | 7.152461372720e-05 |
| 12 | 3 | -9.862806858110e-04 | 7.197569750460e-04 |
| 12 | 4 | 9.846923705680e-06 | 4.740876399370e-04 |
| 12 | 5 | -1.193356283570e-04 | 2.497341740410e-04 |
| 12 | 6 | 1.356511759680e-05 | -1.234149507820e-04 |
| 12 | 7 | 8.852545661540e-04 | -8.145742379970e-04 |
| 12 | 8 | 4.139273803930e-05 | -8.917948715270e-04 |
| 12 | 9 | 1.611677244440e-04 | -2.421305769220e-04 |
| 12 | 10 | -3.435167880620e-05 | 1.658720480310e-04 |
| 12 | 11 | -7.734284897900e-04 | 1.340420577700e-03 |
| 12 | 12 | -1.963347146390e-04 | 1.682031157840e-03 |
| 13 | 0 | 7.172376069870e-05 | 0.000000000000e90 |
| 13 | 1 | -5.166324062220e-04 | 4.002311551290e-04 |
| 13 | 2 | -8.113006587390e-05 | 1.104653039030e-04 |
| 13 | 3 | -1.010131602060e-04 | -8.207930629620e-05 |
| 13 | 4 | 3.474784511650e-05 | -7.666716222020e-04 |
| 13 | 5 | 5.692056052810e-04 | -4.546803398150e-04 |
| 13 | 6 | 2.274234109390e-04 | -1.381178917270e-04 |

| m | n | $C_{ij}$ | $S_{ij}$ |
|---|---|---|---|
| 13 | 7 | 1.000384750630e-04 | 6.375096615200e-05 |
| 13 | 8 | -6.437517725010e-05 | 7.520359785560e-04 |
| 13 | 9 | -6.517574800310e-04 | 5.685814553720e-04 |
| 13 | 10 | -3.341832259600e-04 | 1.800024772190e-04 |
| 13 | 11 | -1.009113138600e-04 | -3.898895816870e-05 |
| 13 | 12 | 8.223254404290e-05 | -7.584317051630e-04 |
| 13 | 13 | 7.286727562360e-04 | -9.974333266110e-04 |
| 14 | 0 | -4.442046152000e-04 | 0.000000000000e104 |
| 14 | 1 | -7.422871498740e-05 | -4.518013990110e-04 |
| 14 | 2 | 6.557752099840e-06 | -3.122583053580e-04 |
| 14 | 3 | 6.068552961990e-04 | -1.660095915440e-04 |
| 14 | 4 | 1.352618296030e-05 | 8.126598527880e-05 |
| 14 | 5 | 8.500564310010e-05 | 4.661723912530e-04 |
| 14 | 6 | -1.993821554100e-05 | 5.201175967790e-04 |
| 14 | 7 | -5.525476490290e-04 | 1.814477497610e-04 |
| 14 | 8 | -5.876528447840e-05 | -1.056713705550e-04 |
| 14 | 9 | -1.066563549550e-04 | -5.646551560880e-04 |
| 14 | 10 | 3.514842922550e-05 | -7.836203122960e-04 |
| 14 | 11 | 4.904225162360e-04 | -1.672522769340e-04 |
| 14 | 12 | 1.565736315110e-04 | 1.072588566830e-04 |
| 14 | 13 | 1.365026688050e-04 | 8.818490908810e-04 |
| 14 | 14 | -5.525236769910e-05 | 1.270255444990e-03 |
| 15 | 0 | -4.502685443070e-05 | 0.000000000000e119 |
| 15 | 1 | 3.461437350270e-04 | 5.748970216570e-05 |
| 15 | 2 | 4.998984139680e-05 | 4.450894420060e-04 |
| 15 | 3 | 6.562157430730e-05 | 3.166778688250e-04 |
| 15 | 4 | -2.016101130070e-05 | 1.144734222110e-04 |
| 15 | 5 | -3.720133629400e-04 | -5.024679798710e-05 |
| 15 | 6 | -1.416386791910e-04 | -4.122582779140e-04 |
| 15 | 7 | -7.072101740780e-05 | -3.993979434370e-04 |
| 15 | 8 | 3.903365889700e-05 | -1.521715266520e-04 |
| 15 | 9 | 4.105566819000e-04 | 3.682439339500e-05 |
| 15 | 10 | 2.132337704300e-04 | 3.479838528430e-04 |
| 15 | 11 | 7.836539956400e-05 | 5.755960747180e-04 |
| 15 | 12 | -5.309839556230e-05 | 1.884659869080e-04 |
| 15 | 13 | -4.412537861560e-04 | -2.866030659860e-05 |
| 15 | 14 | -2.658668277550e-04 | -2.986297437300e-04 |
| 15 | 15 | -9.099504643860e-05 | -1.088018942010e-03 |